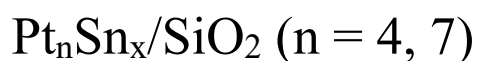


# Coking-Resistant Sub-Nano Dehydrogenation Catalysts:



*Timothy J. Gorey,<sup>a†</sup> Borna Zandkarimi,<sup>b†</sup> Guangjing Li,<sup>a</sup> Eric T. Baxter,<sup>a</sup>*

*Anastassia N. Alexandrova,<sup>b,c\*</sup> and Scott L. Anderson<sup>a\*</sup>*

<sup>a</sup>Chemistry Department, University of Utah, 315 S. 1400 E., Salt Lake City, UT 84112

<sup>b</sup>Chemistry and Biochemistry, University of California, Los Angeles, and <sup>c</sup>California NanoSystems Institute, Los Angeles, CA 90095

† These authors contributed equally to this work.

\*Senior Authors

Corresponding Authors: Scott Anderson, (801) 585-7289, [anderson@utah.edu](mailto:anderson@utah.edu), Anastassia

Alexandrova, (310) 825-3769, [ana@chem.ucla.edu](mailto:ana@chem.ucla.edu)

## ABSTRACT

We present a combined experimental/theoretical study of  $\text{Pt}_n/\text{SiO}_2$  and  $\text{Pt}_n\text{Sn}_x/\text{SiO}_2$  ( $n = 4, 7$ ) model catalysts for the endothermic dehydrogenation of hydrocarbons, using the ethylene intermediate as a model reactant. Mass-selected  $\text{Pt}_n$  clusters were deposited onto amorphous  $\text{SiO}_2/\text{Si}(100)$  to make the  $\text{Pt}_n\text{SiO}_2$  model catalysts. To produce  $\text{Pt}_n\text{Sn}_x$  clusters, size-selected  $\text{Pt}_n$  were used to seed selective deposition of Sn on Pt via a self-limiting  $\text{H}_2/\text{SnCl}_4/\text{H}_2$  reaction sequence. Model catalysts were analyzed using  $\text{C}_2\text{D}_4$  and CO temperature programmed desorption (TPD), low energy ion scattering (ISS), X-ray photoelectron spectroscopy (XPS), plane wave density functional theory (DFT) global optimization combined with a statistical mechanical description of the catalytic interface, and a DFT mechanistic study. Supported pure  $\text{Pt}_n$  clusters are found to be highly active toward dehydrogenation of  $\text{C}_2\text{D}_4$ , quickly deactivating due to a combination of carbon deposition and sintering, resulting in loss of accessible Pt sites. Addition of Sn to  $\text{Pt}_n$  clusters results in the complete suppression of  $\text{C}_2\text{D}_4$  dehydrogenation and carbon deposition, and also stabilizes the clusters against thermal sintering. Theory shows that both systems have thermal access to a multitude of cluster structures and adsorbate configurations that form a statistical ensemble. While  $\text{Pt}_4/\text{SiO}_2$  clusters bind ethylene in both di- $\sigma$ - and  $\pi$ -bonded configurations,  $\text{Pt}_4\text{Sn}_3/\text{SiO}_2$  binds  $\text{C}_2\text{H}_4$  only in the  $\pi$ -mode, with di- $\sigma$  bonding suppressed by a combination of electronic and geometric features of the PtSn clusters. Dehydrogenation reaction profiles on the accessible cluster isomers were calculated using the climbing image nudged elastic band (CI-NEB) method. Dehydrogenation of di- $\sigma$  bound ethylene is computed to dominant, and suppressed by Sn addition, in agreement with the experiments. DFT indicates that after Sn alloying, the barrier for ethane-to-ethylene conversion is lower than that for unwanted ethylene dehydrogenation.

**KEYWORDS:** dehydrogenation, cluster catalysis, fluxionality, coking, PtSn

## INTRODUCTION

Carbon deposition (“coking”) in high temperature reactions under hydrocarbon-rich conditions is a serious catalyst deactivation mechanism, thus understanding the mechanism and developing approaches to suppress carbon deposition are interesting. One reaction of this type is endothermic alkane dehydrogenation, and we have been examining carbon deposition over sub-nano Pt<sup>1</sup> and Pt alloy cluster catalysts,<sup>2-4</sup> with the goal of stabilizing the clusters against both coking and sintering, which is a serious problem for clusters at high temperatures. In addition to maximizing the accessibility of precious metal atoms in the surface layer, sub-nano clusters often have size-dependent properties that provide additional opportunities for catalyst tuning.<sup>5-15</sup> Small clusters are also relatively tractable theoretically, thus these systems allow detailed modeling of the effects of cluster physical and chemical properties on reaction mechanisms.<sup>9, 16-22</sup> Even for a single cluster size, however, cluster reactions can be quite complex, with multiple structural isomers contributing and evolving during reactions due to thermal and adsorbate effects.

Because reducing coking on Pt-based catalysts is important in many applications, there have been many studies of mitigation strategies. Here we focus on use of Pt-Sn alloy catalysts for dehydrogenation and other reactions where coking is problematic. For example, coke formation has been studied on practical Pt catalysts<sup>23-24</sup> and has been addressed by passivating specific metal sites with Sn, ranging from trace to stoichiometric amounts.<sup>25-30</sup> Though successful, the complex nature of practical catalysts makes detailed understanding of the mechanistic origins of the Pt-Sn relationship and its beneficial effects on catalytic dehydrogenation difficult. It is useful, therefore, to consider model catalysts, including ordered surface alloys and planar supported cluster catalysts.

Koel and co-workers studied the branching between alkene desorption and decomposition/dehydrogenation (leading to carbon deposition) on a series of ordered Pt-Sn surface

alloys, ranging from pure Pt(111) to an alloy with 2:1 Pt:Sn stoichiometry. With increasing Sn content, the desorption temperature for the alkenes decreased substantially, without any reduction in the saturation coverage. By decreasing the binding energy, desorption of intact alkenes becomes favored over further dehydrogenation. (i.e., coking is suppressed). It was found that the di- $\sigma$  ethylene binding geometry was preferred for all the alloys, as well as for Pt (111).<sup>31-32</sup> In a comparable study using DFT methods, ethane adsorption to extended Pt and PtSn surfaces was explored by Hook *et al.*, who also found that ethylene binds in a di- $\sigma$  fashion to both Pt and PtSn extended surfaces. As in the experiments, the ethylene adsorption energy decreased below the barrier for dehydrogenation of ethylene, resulting in suppression of dehydrogenation and carbon deposition.<sup>33</sup> This was rationalized as being due to a combination of binding geometry and electronic effects.

For small PtSn supported nanoparticles, some differences have been noted. For example, Shen *et al.*<sup>30</sup> and Natal-Santiago *et al.*<sup>29</sup> studied adsorption geometries and energies of ethylene to silica-supported Pt and PtSn catalyst particles (diam. = 2-5 nm) using microcalorimetry and IR spectroscopy. The nano Pt catalyst supported both di- $\sigma$  and  $\pi$ -bound ethylene, and incorporation of Sn resulted in a decrease in the heat of adsorption and an increase in the fraction of  $\pi$ -bound ethylene with increasing Sn content. The appearance of substantial  $\pi$ -bonding for small PtSn nanoparticles differs from the observation of purely di- $\sigma$  bonding for extended PtSn surface alloys, suggesting significant effects of particle size. Sub-nanometer, or “ultra-dispersed” catalysts would therefore be expected to have additional differences in catalytic behavior. For example, in a study of propane dehydrogenation, Datye *et al.*, examined  $0.6 \pm 0.2$  nm Pt and PtSn particles on Al<sub>2</sub>O<sub>3</sub>.<sup>34</sup> From a thermal stability perspective, it was proposed that Sn helped maintain the dispersion of Pt

particles under reaction and oxidative regeneration conditions, and that this was the major contributor to the prolonged activity for PtSn vs. pure Pt catalysts.

In another study with sub-nanometer particles, Ha and Baxter *et al.*<sup>14</sup> added boron to size-selected Pt<sub>n</sub>/Al<sub>2</sub>O<sub>3</sub> model catalysts to suppress dehydrogenation/coking during ethylene temperature-programmed desorption/reaction (TPD/R). The model catalyst was well-defined enough to allow an accurate DFT model to be built and used to examine changes in energetics and mechanisms for ethylene binding/desorption from Pt<sub>n</sub>/Al<sub>2</sub>O<sub>3</sub><sup>1</sup> and Pt<sub>n</sub>B<sub>x</sub>/Al<sub>2</sub>O<sub>3</sub>.<sup>3</sup> Addition of boron suppressed di-σ binding of ethylene, and substantially lowered the desorption energy, such that ethylene desorbed rather than undergoing dehydrogenation leading to carbon deposition.

Here we apply size-selection methods to study PtSn/SiO<sub>2</sub> model catalysts. Size- and composition-selected clusters were prepared by using mass-selected Pt<sub>n</sub> deposition to prepare planar SiO<sub>2</sub> supports decorated by a precisely controlled coverage of size-selected clusters. These were then used to seed highly selective Sn deposition on the clusters via a self-limiting reaction process. The composition and morphology were probed using X-ray photoelectron and low-energy ion scattering spectroscopies (XPS, ISS). Pt<sub>n</sub>/SiO<sub>2</sub> was chosen as the system, because the process used to deposit Sn is quite selective, depositing Sn almost exclusively on the Pt clusters, rather than on the SiO<sub>2</sub> support. We initially examined Sn modification of Pt<sub>n</sub>/alumina/NiAl(110) and Pt<sub>n</sub>/alumina/Ta(110), but found considerable non-selective Sn deposition on the alumina supports. Those systems have interesting catalytic activity,<sup>35</sup> but for the purpose of studying Pt<sub>n</sub>Sn<sub>x</sub> clusters with well-defined composition, the SiO<sub>2</sub> support is better. Additional detail on catalyst preparation is available below in the Methods section, and a complete characterization of stoichiometry, size, and composition has been previously published.<sup>2</sup> Here, we compare catalytic properties of Pt<sub>4</sub>/SiO<sub>2</sub> and Pt<sub>7</sub>/SiO<sub>2</sub> to these size- and composition-controlled Pt<sub>4</sub>Sn<sub>3.3</sub>/SiO<sub>2</sub> and

Pt<sub>7</sub>Sn<sub>6.3</sub>/SiO<sub>2</sub> bimetallic cluster catalysts. DFT calculations are used to examine structure and binding properties of the clusters for thermally populated cluster isomer ensembles for Pt<sub>4</sub>/SiO<sub>2</sub> and Pt<sub>4</sub>Sn<sub>3</sub>/SiO<sub>2</sub>. Note that the amorphous structure of the SiO<sub>2</sub> native oxide requires a large slab in the calculations. This factor, together with the need to consider the thermally accessible isomer ensembles, makes the DFT calculations quite expensive even for small Pt<sub>n</sub>Sn<sub>x</sub>/SiO<sub>2</sub>, and infeasible for larger clusters.

## RESULTS AND DISCUSSION

In the following, we present experiments comparing Pt<sub>n</sub>/SiO<sub>2</sub> and Pt<sub>n</sub>Sn<sub>x</sub>/SiO<sub>2</sub>, for four clusters: Pt<sub>4</sub>, Pt<sub>7</sub>, Pt<sub>4</sub>Sn<sub>3.3</sub>, and Pt<sub>7</sub>Sn<sub>6.3</sub>. The theory results are focused on Pt<sub>4</sub>/SiO<sub>2</sub> and Pt<sub>4</sub>Sn<sub>3</sub>/SiO<sub>2</sub>, however, the experiments for Pt<sub>4</sub> and Pt<sub>7</sub> suggest that similar considerations should apply to the Pt<sub>7</sub> and Pt<sub>7</sub>Sn<sub>6.3</sub> experiments. The two Pt<sub>n</sub> cluster sizes were selected because Pt<sub>4</sub> and Pt<sub>7</sub> had been studied previously on Al<sub>2</sub>O<sub>3</sub> supports, with Pt<sub>4</sub> found to have all atoms exposed in the surface layer and Pt<sub>7</sub> having both single layer and prismatic 3D isomers, the latter of which was found to isomerize to a single layer structure upon adsorption of multiple ethylene molecules.<sup>1</sup> In addition, the low energy structures for Pt<sub>4</sub>Sn<sub>3</sub>/SiO<sub>2</sub> were already available from our paper describing the method for producing size- and composition-selected Pt<sub>n</sub>Sn<sub>x</sub>/SiO<sub>2</sub> model catalysts.<sup>2</sup>

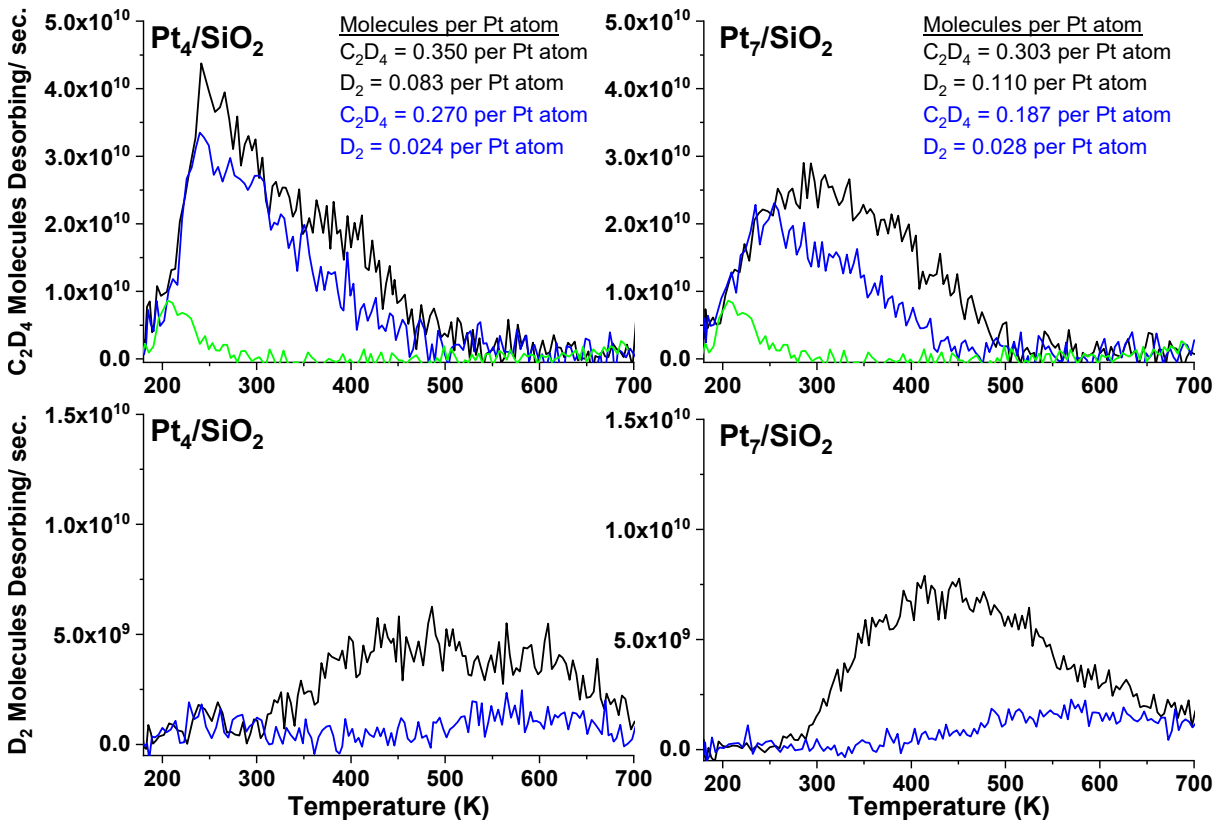


**Figure 1.** Intact desorption of  $C_2D_4$  (top) and  $D_2$  (bottom) from the first (black) and fourth (blue)  $C_2D_4$  TPD. These spectra were collected after a 10 L dose of  $C_2D_4$  to  $Pt_n/SiO_2$  ( $n = 4, 7$ ).  $C_2D_4$  desorption from  $SiO_2$  is also plotted (green), no  $D_2$  evolution from  $SiO_2$  is observed.

**Ethylene Desorption vs. Dehydrogenation.**  $C_2D_4$  and  $D_2$  desorption from  $Pt_4/SiO_2$  and  $Pt_7/SiO_2$  are shown in **Fig. 1**. To examine the effects of repeated  $C_2D_4$  exposure and heating, a total of four TPD/R runs were carried out, but the figure shows results only for the 1<sup>st</sup> (black) and 4<sup>th</sup> (blue) runs. The data for all four runs are shown in **Fig. S1**. Most experiments were done with  $C_2D_4$  to avoid interference with  $H_2$  detection from high background at mass 2, however, the background is also high at mass 28, corresponding to  $C_2D_2$ . Therefore, some experiments were done using  $C_2H_4$  to look for acetylene desorption. None was observed. We also looked for ethane signal from possible hydrogenation processes, but the signals were negligible. Because cracking

of  $C_2D_4$  to  $D_2^+$  in the mass spectrometer is weak, this contribution to the  $D_2$  signal has not been subtracted in the figure.

The figures also show the  $C_2D_4$  desorption observed from a Pt-free  $SiO_2$  substrate (green), indicating that for the 180 K  $C_2D_4$  exposure temperature chosen, only a small amount of  $C_2D_4$  desorbs from the  $SiO_2$  substrate, and that  $SiO_2$  does not support  $D_2$  desorption. We tested the effect of lowering the dose temperature from 180 K to 150 K, observing a large increase in the desorption intensity from the  $SiO_2$  support. The integrated  $C_2D_4$  TPD signal after 180 K dosing on  $SiO_2$  corresponds to  $\sim 3.5 \times 10^{12}$  molecules/cm<sup>2</sup> – well below 1% of a monolayer.

For  $Pt_n/SiO_2$  samples,  $C_2D_4$  desorption also begins at 180 K, initially matching the desorption from  $SiO_2$ , but then continuing with much higher intensities before eventually declining and disappearing by  $\sim 500$  K. The signal between 180 K and  $\sim 220$  K is, therefore, attributed to desorption mostly from  $SiO_2$  sites, while the signal at higher temperatures is attributed to desorption from sites associated with the  $Pt_n$  clusters.

The temperature dependence for desorption of intact  $C_2D_4$  is different for the two cluster sizes. For  $Pt_4$ , during the 1<sup>st</sup> TPD/R run, the desorption appears bimodal, with a strong and relatively sharp peak near 250 K, followed by a shoulder in the 350-400 K range, with a rapid intensity drop above 400 K. For  $Pt_7$ ,  $C_2D_4$  desorption grows more slowly at low temperatures, peaking broadly around 300 K, and declining gradually above 400 K. According to the DFT calculations, the ethylene binding energy of the  $C_2H_4/Pt_4/SiO_2$  global minimum structure, where the ethylene is bound in the di- $\sigma$  mode, is roughly 0.14 eV stronger than in the second local minimum structure (23% population at 700 K), where ethylene is  $\pi$ -bonded. More detailed discussion can be found in the DFT analysis section.



For the 1<sup>st</sup> run on both Pt<sub>4</sub> and Pt<sub>7</sub>, significant D<sub>2</sub> desorption starts just below 300 K and peaks broadly around 440 K, declining to baseline above 600 K. The D<sub>2</sub> signal is significantly larger for Pt<sub>7</sub> than Pt<sub>4</sub>. In one experiment, the heat ramp was extended to 1000 K to check for additional C<sub>2</sub>D<sub>4</sub> or D<sub>2</sub> desorption above 700 K. None was observed, suggesting that dehydrogenation and desorption go to completion by 700 K. The behavior observed here for Pt<sub>4</sub>/SiO<sub>2</sub> and Pt<sub>7</sub>/SiO<sub>2</sub> is similar to that observed for Pt<sub>n</sub>/Al<sub>2</sub>O<sub>3</sub> (n =4, 7), with intact C<sub>2</sub>D<sub>4</sub> desorption peaking near 300 K, and D<sub>2</sub> desorption in the ~300 – 600 K range.<sup>1</sup>

The integrated numbers of C<sub>2</sub>D<sub>4</sub> and D<sub>2</sub> molecules desorbing from each sample are listed in **Table 1**, and because we know the Pt coverage precisely ( $1.5 \times 10^{14}$  atoms/cm<sup>2</sup>), the integrated desorption numbers are given as molecules *per* Pt atom. To correct the numbers for the contribution of desorption from the SiO<sub>2</sub> substrate, ~0.02 C<sub>2</sub>D<sub>4</sub> molecules/Pt atom should be subtracted. With this correction, we find that ~1.4 and ~2.1 intact C<sub>2</sub>D<sub>4</sub> molecules desorb per Pt<sub>4</sub> and Pt<sub>7</sub> cluster, respectively, with the corresponding D<sub>2</sub> desorption being ~0.33 and ~0.77 D<sub>2</sub> molecules *per* cluster. Given that D<sub>2</sub> desorption goes to completion before termination of the heat ramp, the total number of C<sub>2</sub>D<sub>4</sub> adsorbed *per* cluster can be estimated as #C<sub>2</sub>D<sub>4</sub> desorbing + 0.5 #D<sub>2</sub> desorbing, giving ~1.6 and ~2.5 C<sub>2</sub>D<sub>4</sub> adsorbed *per* Pt<sub>4</sub> and Pt<sub>7</sub>, respectively. In theoretical modeling of Pt<sub>4</sub>/SiO<sub>2</sub>, we therefore considered coverages of one and two ethylene molecules per cluster. As expected, the number of adsorbed ethylene *per* cluster increases with cluster size, however, on a *per* Pt atom basis, slightly more ethylene adsorbs on Pt<sub>4</sub>. This effect is consistent with the observation by ISS,<sup>2</sup> that Pt<sub>7</sub>/SiO<sub>2</sub> has a smaller fraction of its Pt atoms in the surface layer, and thus presents fewer ethylene binding sites.

**Table 1.** Numbers of C<sub>2</sub>D<sub>4</sub> and D<sub>2</sub> molecules desorbing *per* Pt atom from Fig. 1.

TPD Run:	Pt <sub>4</sub> /SiO <sub>2</sub>		Pt <sub>7</sub> /SiO <sub>2</sub>	
1 <sup>st</sup>	0.350 C <sub>2</sub> D <sub>4</sub> /Pt	0.083 D <sub>2</sub> /Pt	0.303 C <sub>2</sub> D <sub>4</sub> /Pt	0.110 D <sub>2</sub> /Pt
2 <sup>nd</sup>	0.340 C <sub>2</sub> D <sub>4</sub> /Pt	0.076 D <sub>2</sub> /Pt	0.282 C <sub>2</sub> D <sub>4</sub> /Pt	0.066 D <sub>2</sub> /Pt
3 <sup>rd</sup>	0.270 C <sub>2</sub> D <sub>4</sub> /Pt	0.046 D <sub>2</sub> /Pt	0.226 C <sub>2</sub> D <sub>4</sub> /Pt	0.050 D <sub>2</sub> /Pt
4 <sup>th</sup>	0.270 C <sub>2</sub> D <sub>4</sub> /Pt	0.024 D <sub>2</sub> /Pt	0.187 C <sub>2</sub> D <sub>4</sub> /Pt	0.028 D <sub>2</sub> /Pt

**Fig. 1** also shows the 4<sup>th</sup> TPD/R run for each sample. Two significant changes are observed: the amount of ethylene desorbing is lower than in the 1<sup>st</sup> run, and the desorption occurs at lower temperatures. In addition, D<sub>2</sub> desorption is substantially weaker, compared to the 1<sup>st</sup> TPD/R run. The changes are qualitatively similar for the two cluster sizes, but more dramatic for Pt<sub>7</sub>, where more dehydrogenation occurred in the 1<sup>st</sup> run. These changes imply that substantially less ethylene adsorbs at 180 K, and that the decrease primarily affects the more stable binding sites responsible for desorption at higher temperatures. As will be shown shortly, stronger binding typically corresponds to the di-σ mode of ethylene attachment, which is a precursor for dehydrogenation, which then poisons those sites by carbon deposits. As shown in **Fig. S1**, the 2<sup>nd</sup>, 3<sup>rd</sup>, and 4<sup>th</sup> TPD/R runs are quite similar, implying that most of the changes to the binding site distribution occur in the 1<sup>st</sup> TPD/R run. In the 4<sup>th</sup> TPD run, the differences between Pt<sub>4</sub>/SiO<sub>2</sub> and Pt<sub>7</sub>/SiO<sub>2</sub> are weaker than in the first, but the Pt<sub>4</sub> sample still had significantly more ethylene desorbing, and with sharper temperature dependence, compared to the Pt<sub>7</sub> sample. Given that both samples had the same total number of Pt atoms, the samples clearly retained at least some memory of the deposited cluster size after repeated TPD/R runs.

Run-to-run losses in the number of C<sub>2</sub>D<sub>4</sub>-Pt sites selectively affects the most-strongly bound C<sub>2</sub>D<sub>4</sub>-Pt sites, and because these are most likely to catalyze dehydrogenation, a run-to-run reduction in D<sub>2</sub> desorption is expected, and observed. Given the observation of D<sub>2</sub> desorption, the loss of C<sub>2</sub>D<sub>4</sub> binding sites in repeated C<sub>2</sub>D<sub>4</sub> TPD runs is at least partially attributable to poisoning by carbon deposition. We show below using XPS that repeated ethylene TPD runs lead to carbon deposition, although the precise amount was difficult to measure because the sensitivity for carbon is relatively low, and the Pt coverage (where C is depositing) is also very low.<sup>1</sup> DFT calculations on Pt<sub>8</sub>/Al<sub>2</sub>O<sub>3</sub> and Pt<sub>8</sub>/Al<sub>2</sub>O<sub>3</sub> with a carbon atom deposited were done to examine changes in cluster morphology and energetics, showing that deposition of electrophilic C causes some rearrangement in cluster geometry.<sup>1</sup> Note, however, that supported Pt<sub>n</sub> clusters are expected to be quite dynamic under reaction conditions, sintering is also likely.

Because we have  $\sim 3 \times 10^{-11}$  Torr of CO background in our UHV system, we always monitor CO desorption during TPD/R experiments. Here,  $\sim 0.2$  CO molecules desorbed *per* Pt atom during the 1<sup>st</sup> run, with substantially less in subsequent runs. This CO contamination level is  $\sim 20$  times larger than would be expected if CO sticks only when impinging directly on a Pt site, and shows that for small, well dispersed clusters, substrate-mediated adsorption (reverse spillover) substantially amplifies the contamination rate. Assuming that CO competes with C<sub>2</sub>D<sub>4</sub> for binding sites, there probably would have been additional C<sub>2</sub>D<sub>4</sub> and D<sub>2</sub> desorption observed in the 1<sup>st</sup> TPD/R runs in absences of CO, and the difference between the 1<sup>st</sup> and subsequent runs would have been larger.

Analogous  $C_2D_4$  TPD/R experiments for PtSn alloy clusters are shown in **Fig. 2**, with all four TPDs shown in **Fig. S2**. In this case, the 1<sup>st</sup> run was done just after completing the  $H_2/SnCl_4/H_2$  exposure process used to deposit Sn, and prior to any heating. At this point there would have been H as well as a small amount of Cl adsorbed on the clusters.<sup>2</sup> Therefore, it is not surprising that the amount of  $C_2D_4$  desorbing in this 1<sup>st</sup> run is substantially smaller than in the 1<sup>st</sup> run for  $Pt_n/SiO_2$ , because many  $C_2D_4$  binding sites would have been blocked during the 180 K  $C_2D_4$  exposure. During this 1<sup>st</sup> TPD/R run, significant HCl desorption was observed (**Fig. S3**), and no Cl was

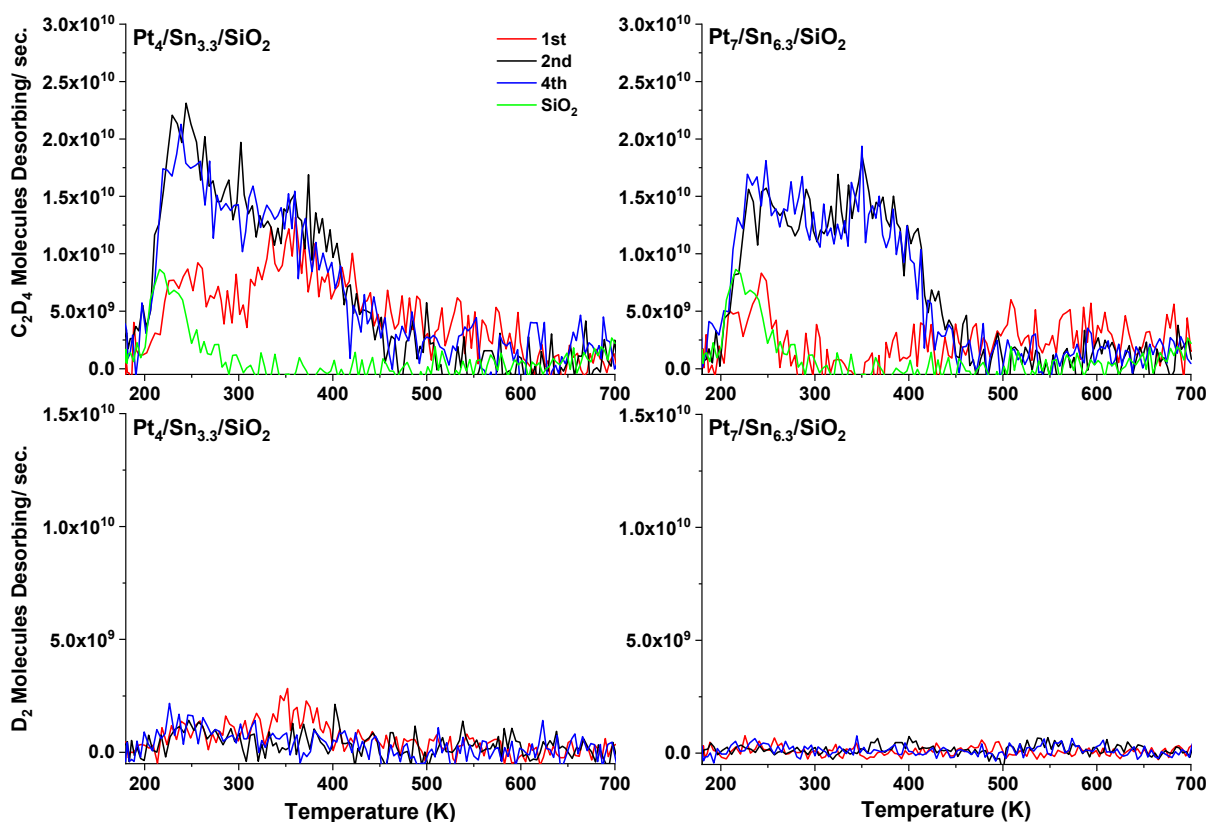


**Figure 2.** Desorption of  $C_2D_4$  (top) and  $D_2$  (bottom) from the first (red), second (black), and fourth (blue)  $C_2D_4$  TPD/R run. Each spectra was collected after a 10 L dose of  $C_2D_4$  to  $Pt_n/SiO_2$  ( $n = 4, 7$ ) at 180 K.  $C_2D_4$  desorption from bare  $SiO_2$  treated with 1 ALD cycle is also plotted (green) – no  $D_2$  was observed in that experiment.

detectable by TPD/R, ISS, or XPS after the 1<sup>st</sup> run. H<sub>2</sub> desorption was not monitored due to large mass 2 background, but 700 K is well above the temperature where hydrogen desorbs from Pt<sub>n</sub>.<sup>1</sup>

In the 2<sup>nd</sup> TPD/R run on each sample, the amount of C<sub>2</sub>D<sub>4</sub> desorbing increased substantially, indicating that desorption of HCl and H<sub>2</sub> during the 1<sup>st</sup> run left more binding sites accessible to C<sub>2</sub>D<sub>4</sub>. Therefore, we feel that the correct comparison is of the 2<sup>nd</sup> TPD/R run for Pt<sub>n</sub>Sn<sub>x</sub>/SiO<sub>2</sub>, with the 1<sup>st</sup> run for the Pt<sub>n</sub>/SiO<sub>2</sub> samples. As before, the number of the C<sub>2</sub>D<sub>4</sub> molecules desorbing *per* Pt atom in the 2<sup>nd</sup>, 3<sup>rd</sup>, and 4<sup>th</sup> TPD/R runs is given in **Table 2**.

**Table 2.** Numbers of C<sub>2</sub>D<sub>4</sub> molecules desorbing per Pt atom from Fig. 2 and Fig. S2.

<b>TPD Run:</b>	<b>Pt<sub>4</sub>Sn<sub>3.3</sub>/SiO<sub>2</sub></b>	<b>Pt<sub>7</sub>Sn<sub>6.3</sub>/SiO<sub>2</sub></b>
<b>2nd</b>	0.190 C <sub>2</sub> D <sub>4</sub> /Pt	0.176 C <sub>2</sub> D <sub>4</sub> /Pt
<b>3rd</b>	0.210 C <sub>2</sub> D <sub>4</sub> /Pt	0.170 C <sub>2</sub> D <sub>4</sub> /Pt
<b>4th</b>	0.190 C <sub>2</sub> D <sub>4</sub> /Pt	0.174 C <sub>2</sub> D <sub>4</sub> /Pt

There are several important points of comparison with the results for pure Pt<sub>n</sub>/SiO<sub>2</sub>. First, there was no significant D<sub>2</sub> desorption in any run on the Pt<sub>n</sub>Sn<sub>x</sub>/SiO<sub>2</sub> samples, i.e., all ethylene desorbed intact. The absence of D<sub>2</sub> desorption implies that there should be little if any carbon deposition. **Fig. S4** summarizes an XPS experiment that shows substantial carbon deposition in repeated TPD/R runs on Pt<sub>n</sub>/SiO<sub>2</sub>, and the complete absence of carbon deposition for Pt<sub>n</sub>Sn<sub>x</sub>/SiO<sub>2</sub> under identical conditions.

Also consistent with the absence of carbon deposition, is the observation that once the H and Cl were desorbed during the 1<sup>st</sup> run, there was little change in the intensity or temperature dependence of C<sub>2</sub>D<sub>4</sub> desorption in TPD runs two through four, compared to the substantial loss of intensity and shifts to lower temperatures observed for pure Pt<sub>n</sub>/SiO<sub>2</sub>. Additionally, the number of C<sub>2</sub>D<sub>4</sub> molecules adsorbing during the 180 K dose was ~50% smaller for the Pt<sub>n</sub>Sn<sub>x</sub>, compared to the pure

Pt<sub>n</sub>, presumably due to site blocking by Sn atoms (note difference in vertical scales). Finally, for the Pt<sub>n</sub>Sn<sub>x</sub>/SiO<sub>2</sub> samples there are cluster size effects on the desorption temperature dependence, weaker than the size effects observed for Pt<sub>n</sub>/SiO<sub>2</sub>, but which are quite persistent in repeated runs. From the perspective of improving the stability of sub-nano Pt cluster catalysts under high temperature hydrocarbon rich conditions, the absence of dehydrogenation (i.e., of carbon deposition) and the stability of the samples in repeated TPD/R runs are both important.

The C<sub>2</sub>D<sub>4</sub> thermal desorption spectra were fit to extract desorption energy distributions,  $\theta(E_{\text{des}})$ , as described in the supporting information. An example fit is shown in **Fig. S5**, and the  $\theta(E_{\text{des}})$  distributions for the 1<sup>st</sup> C<sub>2</sub>D<sub>4</sub> TPD on Pt<sub>4</sub>/SiO<sub>2</sub> and the 2<sup>nd</sup> C<sub>2</sub>D<sub>4</sub> TPD on Pt<sub>4</sub>Sn<sub>3.3</sub>/SiO<sub>2</sub> are compared in **Fig. 3**.  $\theta(E_{\text{des}})$  distributions for Pt<sub>7</sub>/SiO<sub>2</sub> and Pt<sub>7</sub>Sn<sub>6.3</sub>/SiO<sub>2</sub> are shown in **Fig. S6**. Three features were included in the  $\theta(E_{\text{des}})$  distributions to fit the experimental temperature dependences: a small feature with  $E_{\text{des}} < 0.6$  eV attributed to desorption from SiO<sub>2</sub> sites, a larger feature with  $0.6 < E_{\text{des}} < 1.2$  eV attributed to desorption from cluster sites, and a second feature with  $0.8 < E_{\text{des}} < 1.6$  eV also attributed to desorption from cluster sites. Note that there is little difference in the range of  $E_{\text{des}}$  observed for Pt<sub>n</sub> and Pt<sub>n</sub>Sn<sub>x</sub>, consistent with the modest differences in desorption temperatures.

The effects of Sn-alloying on the  $\text{Pt}_n/\text{SiO}_2$  system should be compared to the effects of Sn alloying on ordered PtSn surface alloys studied by Koel and co-workers.<sup>31-32</sup> In both cases, ethylene dehydrogenation, leading to carbon deposition, is strongly suppressed, compared to pure  $\text{Pt}_n/\text{SiO}_2$  or to Pt(111), but the mechanism appears to be different. For the PtSn surface alloys, the saturation ethylene coverage was Sn-independent, whereas for the clusters, Sn significantly reduced the coverage. For the surface alloys, the ethylene desorption temperature dropped with increasing Sn coverage from

$\sim 285$  K for pure Pt(111)<sup>36</sup> to 184

K for the  $\sqrt{3} \times \sqrt{3} R30^\circ$  alloy

which has 1:2 Sn:Pt ratio in the

surface layer. Hook *et al.* used

DFT to examine ethane

dehydrogenation over PtSn

surface alloys, finding,

consistent with the experiments

of Koel and co-workers, that Sn

depresses the alkene desorption

energy below the barrier for

dehydrogenation, due to a

combination of geometric and

electronic effects.<sup>33</sup> Thus in the

surface alloys, the suppression

of carbon deposition appears to

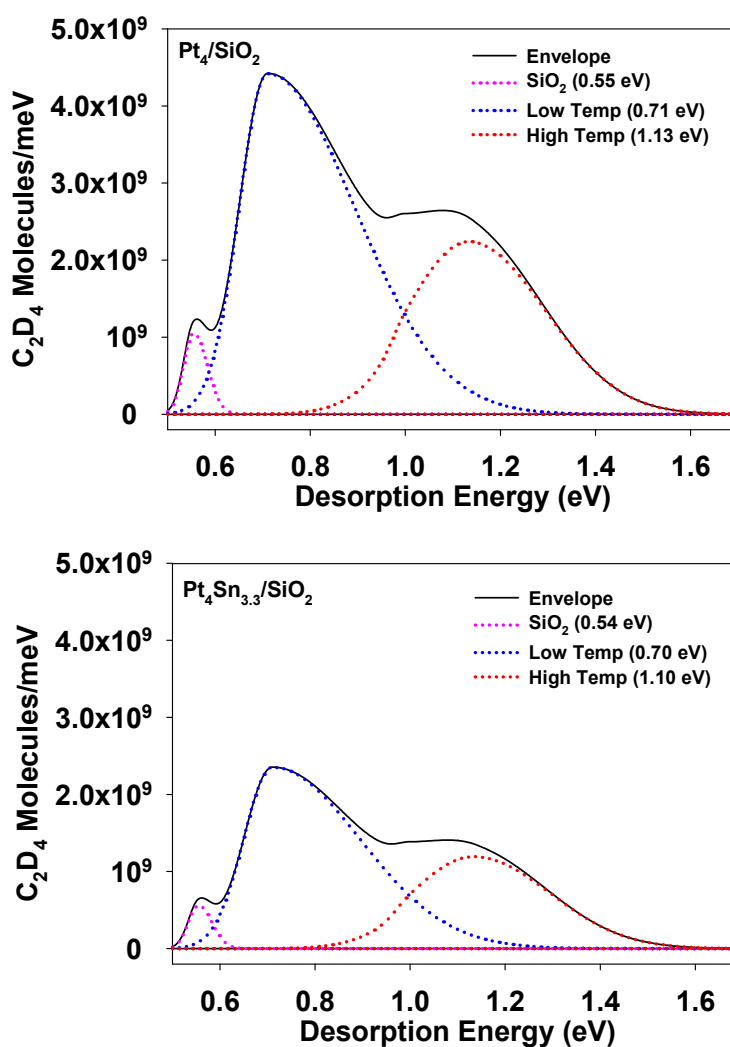


**Figure 3.** Energy desorption ( $E_{\text{des}}$ ) profiles for  $\text{Pt}_4/\text{SiO}_2$  (top) and  $\text{Pt}_4\text{Sn}_{3.3}/\text{SiO}_2$  (bottom).

be largely due to the reduction in ethylene binding energy. This was also the conclusion in our study of the effects of boron addition to Pt<sub>n</sub>/alumina model catalysts,<sup>4</sup> where boration shifted the ethylene desorption temperatures into the cryogenic range, thereby suppressing dehydrogenation. In contrast, for the Pt<sub>n</sub> vs. Pt<sub>n</sub>Sn<sub>x</sub> clusters here, there is no significant difference between the ethylene desorption temperatures or the extracted E<sub>des</sub> distributions, suggesting that suppression of dehydrogenation/carbon deposition must result from a different mechanism.

### ISS probing of the effects of TPD/R.

ISS experiments were carried out to probe differences in the structure of the Pt<sub>n</sub> and Pt<sub>n</sub>Sn<sub>x</sub> samples, and to provide insight regarding the changes in C<sub>2</sub>D<sub>4</sub> and D<sub>2</sub> desorption behavior that occur in multiple TPD runs for Pt<sub>n</sub>/SiO<sub>2</sub>. Peaks in ISS data result mostly from events in which He<sup>+</sup> scatters from a single atom in the surface layer, such that the retained energy, E<sub>k</sub>/E<sub>k0</sub>, depends on the target atom mass.<sup>37</sup> Multiple scattering, and scattering from atoms deeper in the surface result in low ion survival probability (ISP), and contribute mostly to the featureless background at low

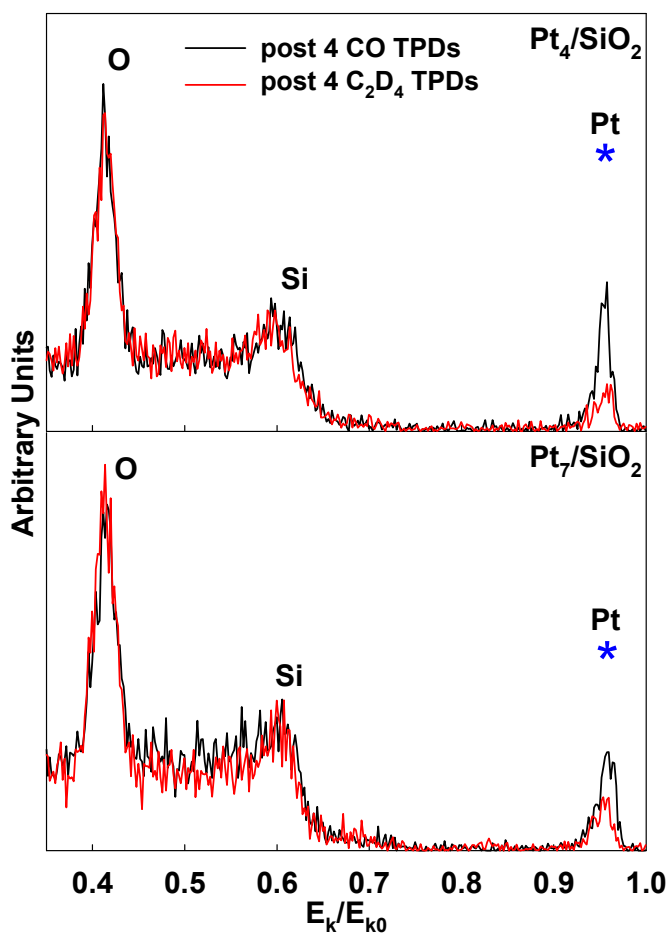


**Figure 4.** Raw ISS spectra for Pt<sub>n</sub>/SiO<sub>2</sub> samples after they have undergone four CO TPDs to 700 K (black) and four C<sub>2</sub>D<sub>4</sub> TPDs (red).



$E_k/E_{k0}$ . The usefulness of ISS here is that it is sensitive both to the cluster morphology and to the presence of adsorbates on the cluster surface, due to shadowing, blocking, and ISP effects.<sup>38-40</sup>

**Fig. 4** summarizes ISS data for Pt<sub>4</sub> and Pt<sub>7</sub> samples after four cycles of C<sub>2</sub>D<sub>4</sub> TPD/R. The results are compared to ISS (on separate samples) after four cycles of CO TPD under identical conditions, to show the effects of TPD with a non-coking adsorbate. Peaks for O, Si, and Pt are observed. For comparison, the intensities of the Pt peak for as-deposited, unheated Pt<sub>n</sub>/SiO<sub>2</sub> samples are indicated in **Fig. 4** by blue stars. The O and Si intensities for the as-deposited samples are not shown because they are essentially identical to the post-TPD/R results in the figure. All the samples were prepared with the same total number of Pt atoms, therefore, if the same fraction of Pt atoms are exposed in the surface layer, the Pt ISS intensities should be identical. It can be seen that the as-deposited Pt intensity is highest for Pt<sub>4</sub>, and ~28% lower for Pt<sub>7</sub>, indicating that some of the Pt atoms in Pt<sub>7</sub>/SiO<sub>2</sub> are not in the surface layer, as would be the case for a 3D cluster structure.

After four CO TPD runs, the Pt intensities for both sizes decrease significantly. This decrease suggests significant sintering of the clusters, although there may also be some contribution from isomerization to structures with fewer atoms in the surface layer.<sup>1-2, 39, 41-42</sup> To test for the possibility that CO adsorption might affect the sintering/isomerization process, a separate experiment was performed in which a Pt<sub>4</sub>/SiO<sub>2</sub> sample was simply flashed to 700 K four times in the absence of any deliberate adsorbate exposure. The resulting Pt ISS intensities were identical to those observed for clusters having undergone four CO TPDs, i.e., the effects are thermal, with no significant effect of small CO exposures.

The decreases in Pt ISS signal after 4 C<sub>2</sub>D<sub>4</sub> TPD/R experiments are substantially larger. This could be taken as evidence that C<sub>2</sub>D<sub>4</sub> enhances sintering, however, we know from the observation of D<sub>2</sub> desorption and the appearance of carbon in post-TPD/R XPS, that there is carbon deposition on these samples. The ISS results are, therefore, confirmation that this carbon is deposited on, and blocks access to Pt sites, as opposed to depositing on the SiO<sub>2</sub> support. Given that the clusters may also be sintering during TPD/R, it is most useful to compare the carbon deposition on a *per* Pt atom, rather than a *per* cluster basis. From the 1<sup>st</sup> TPD/R run data in (Fig. 1), we can see that Pt<sub>4</sub> has a higher density of C<sub>2</sub>D<sub>4</sub> binding sites (0.43/Pt atom), than Pt<sub>7</sub> (0.36/Pt atom), and a lower D<sub>2</sub>/C<sub>2</sub>D<sub>4</sub> desorption ratio (0.23), compared to 0.36 for Pt<sub>7</sub>. If we assume each D<sub>2</sub> desorption results in deposition on one C atom, then for Pt<sub>4</sub> the 1<sup>st</sup> TPD/R run deposits ~0.1 C/Pt atom, while for Pt<sub>7</sub>, it should deposit slightly more – 0.13 C/Pt. As can be seen from Fig. S1 the differences are smaller in subsequent TPD/R runs. After four runs, the final Pt ISS intensities are similar for the two clusters.

Analogous ISS experiments for Pt<sub>n</sub>Sn<sub>x</sub>/SiO<sub>2</sub> are shown in Fig. 5. Sets of

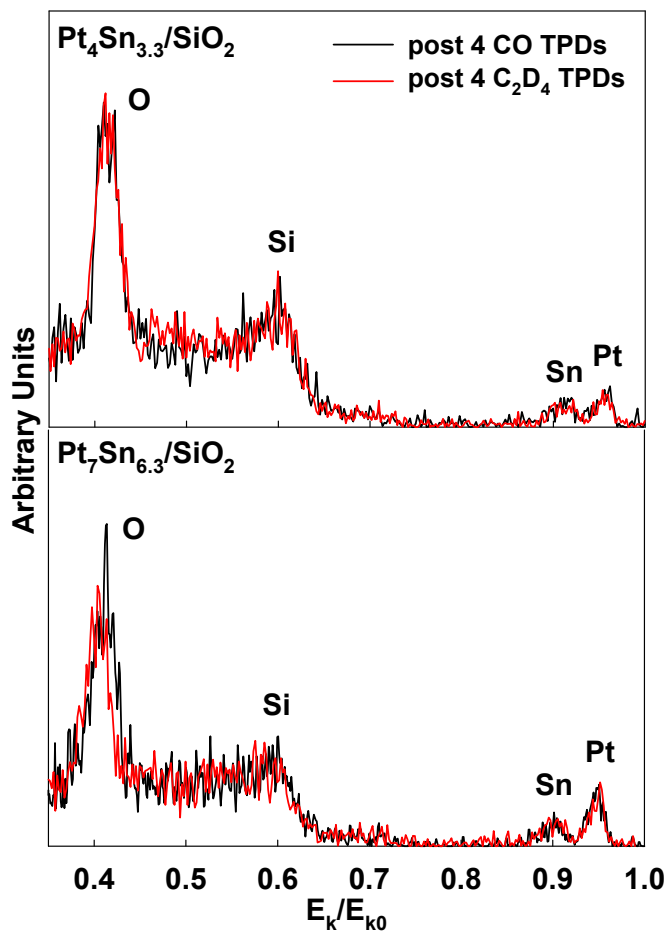


**Figure 5.** Raw ISS Scans for Pt<sub>4</sub>Sn<sub>3.3</sub>/SiO<sub>2</sub> and Pt<sub>7</sub>Sn<sub>6.3</sub>/SiO<sub>2</sub> after four C<sub>2</sub>D<sub>4</sub> TPDs (red) and 4 CO TPDs (black)

$Pt_nSn_x/SiO_2$  samples were prepared and exposed to either four  $C_2D_4$  TPD/R runs, or four CO TPD runs, then examined by ISS. It can be seen that the O and Si peaks are similar to those in the  $Pt_n/SiO_2$  samples, as expected because Sn deposits primarily on the Pt clusters,<sup>2</sup> but that the Pt peak is substantially less intense, and a peak for Sn is observed.

It is also interesting to compare the post TPD ISS to ISS measured just after the  $H_2/SnCl_2/H_2$  treatment (prior to any heating), and after the initial heating to drive off H

and Cl. For the treated, unheated sample, the Sn peak is larger and the Pt peak is smaller (Sn:Pt ratio  $\approx 2$ ) compared to those in Fig. 5, as might be expected for Sn initially deposited on top of the Pt clusters. After initial heating to drive off H and Cl, the spectrum is essentially identical to the post-TPD spectra shown in Fig. 5. i.e., neither of the repeated TPD/R experiments has any

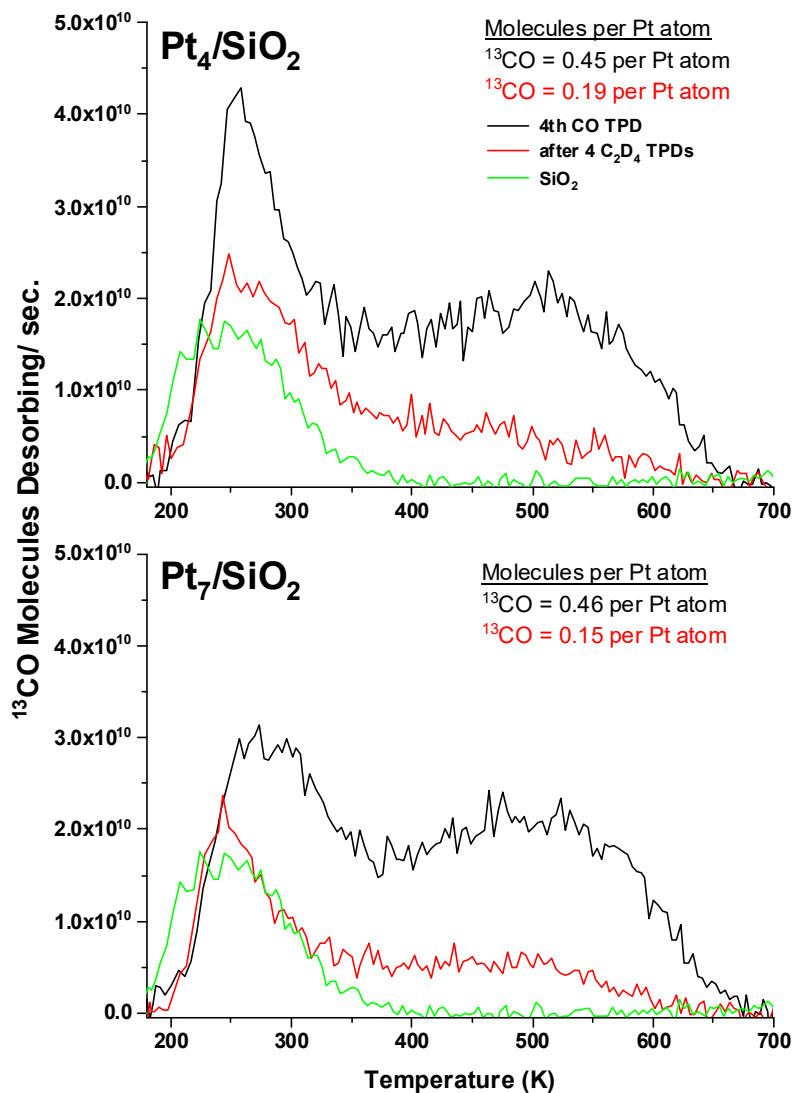


**Figure 6.**  $^{13}CO$  TPD after four CO TPDs (black line) and a  $^{13}CO$  TPD after four  $C_2D_4$  TPDs for  $Pt_n/SiO_2$  (red). CO desorption from  $SiO_2$  is also shown (green)

significant effect on the ISS. The stability with respect to repeated C<sub>2</sub>D<sub>4</sub> TPD/R runs is a consequence of the absence of carbon deposition on the clusters. Consistent with the TPD/R data in **Fig. 2**, ISS shows that Sn alloying significantly reduces the number accessible Pt binding sites, but that the sites present are quite stable.

**CO desorption as a probe of accessible Pt sites.**

The final approach used to probe the effects of repeated heating and C<sub>2</sub>D<sub>4</sub> exposure on the clusters was to carry out <sup>13</sup>CO TPD after the C<sub>2</sub>D<sub>4</sub> TPD/R sequence (on different samples than those used for ISS characterization). **Fig. 6** compares CO TPD measured for a sample first subjected to four C<sub>2</sub>D<sub>4</sub> TPD/R runs (red) to the CO desorption measured in the 4<sup>th</sup> in a series of sequential CO TPDs (black). For comparison, CO desorption from the SiO<sub>2</sub>

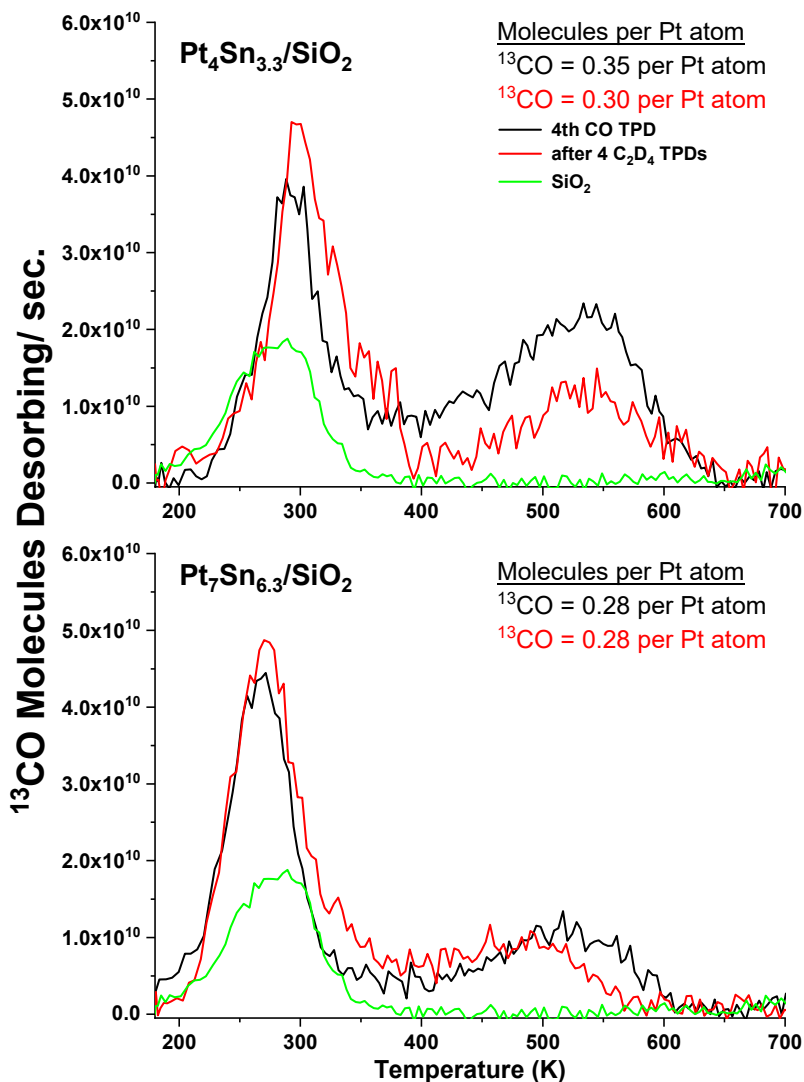


**Figure 7.** CO TPD spectra of Pt<sub>n</sub>Sn<sub>x</sub>/SiO<sub>2</sub> after four CO TPDs (black) and four C<sub>2</sub>D<sub>4</sub> TPDs (red). The 2<sup>nd</sup> <sup>13</sup>CO TPD from H<sub>2</sub>/SnCl<sub>4</sub>/H<sub>2</sub> – SiO<sub>2</sub> is also shown (green).

substrate is also shown (green). The ion signals were converted to numbers of CO molecules using the process described above, and the integrated number of CO molecules indicated in the text on each frame of the figure have been corrected for CO desorbing from the SiO<sub>2</sub> substrate, i.e., the numbers correspond to the CO desorbing from Pt sites. For Pt<sub>4</sub> and Pt<sub>7</sub>, repeated C<sub>2</sub>D<sub>4</sub> TPD/R results in far larger attenuation of Pt-associated CO binding sites, and particularly of the sites with high E<sub>des</sub>, compared to repeated CO TPD runs. This mirrors the ISS results, where C<sub>2</sub>D<sub>4</sub> TPD/R caused a much larger Pt intensity attenuation.

**Fig. 7** shows the analogous results for Sn ALD-treated samples. In this case, the desorption shown for the substrate (“H<sub>2</sub>/SnCl<sub>4</sub>/H<sub>2</sub> – SiO<sub>2</sub>”) is for SiO<sub>2</sub> subjected to the Sn ALD treatment, then heated to drive off any residual Cl or H, before being probed by CO TPD. For the Sn-treated samples, the differences in CO desorption for samples after repeated CO TPDs vs. repeated C<sub>2</sub>D<sub>4</sub> TPD/R runs are much smaller than for the Sn-free Pt<sub>n</sub>/SiO<sub>2</sub> samples. For Pt<sub>4</sub>Sn<sub>3.3</sub>, repeated C<sub>2</sub>D<sub>4</sub> TPD/R runs resulted in a shift in intensity from the higher to the lower temperature desorption feature, with a ~14% decrease in the integrated number of CO molecules desorbing, compared to the effects of four CO TPD runs. For Pt<sub>7</sub>Sn<sub>6.3</sub>, similar, but smaller changes in the desorption temperature dependence were observed, and the integrated number of CO molecules desorbing was identical for the samples subjected to multiple CO or C<sub>2</sub>D<sub>4</sub> TPD experiments. It is not clear why the difference between the effects of C<sub>2</sub>D<sub>4</sub> and CO TPD/R was larger for the smaller cluster size, however, for such a small cluster it would not be surprising if the degree of sintering occurring during the TPD heat ramps is affected by whether the clusters are saturated by CO or by C<sub>2</sub>D<sub>4</sub>. Note that in the analogous experiments on pure Pt<sub>4</sub>, both the low and high temperature desorption features decreased significantly more after C<sub>2</sub>D<sub>4</sub> TPD/R, such that the decrease in total number of

CO binding sites was almost 60% bigger than in multiple CO TPDs. Clearly, the carbon deposition occurring during C<sub>2</sub>D<sub>4</sub> TPD on pure Pt<sub>n</sub> has a large effect on the site availability.

### **DFT Analysis of the Effects of Sn Alloying on Ethylene Binding and Dehydrogenation.**

Supported cluster catalysts can have many structural isomers accessible in the  $\leq 700$  K temperature regime of interest here.<sup>43-46</sup> These isomers can have similar energies, despite having different morphologies, with different morphologies favoring different binding sites and chemical character. It is important to consider these different isomers in the mechanism, because they are expected to be thermally-populated due to high fluxionality of the clusters in this temperature regime.<sup>22, 47</sup> Due to the large amount of sampling needed for the reliable exploration of the potential energy surfaces, we focus the theory on Pt<sub>4</sub>/SiO<sub>2</sub> and Pt<sub>4</sub>Sn<sub>3</sub>/SiO<sub>2</sub>.

From the experiments, an average of  $\sim 1.4$  C<sub>2</sub>D<sub>4</sub> molecules are adsorbed *per* Pt<sub>4</sub> cluster; therefore, each isomer has also been optimized with either one or two C<sub>2</sub>H<sub>4</sub> molecules adsorbed. Structures obtained from the global optimization are shown in **Figs. 8 and S7**. Note that C<sub>2</sub>H<sub>4</sub> is able to bind in several configurations depending on the isomer. For instance, C<sub>2</sub>H<sub>4</sub> in the global minimum structure of C<sub>2</sub>H<sub>4</sub>/Pt<sub>4</sub>/SiO<sub>2</sub> preferentially binds in the di- $\sigma$  binding mode, whereas in the global minimum of (C<sub>2</sub>H<sub>4</sub>)<sub>2</sub>/Pt<sub>4</sub>/SiO<sub>2</sub> there is one di- $\sigma$  bound ethylene, and one  $\pi$ -bound ethylene. Note that other higher energy isomers, which are thermally accessible at higher temperatures, can have different C<sub>2</sub>H<sub>4</sub> binding preferences than the global minimum, as shown in **Fig. 8**. Previously, it was shown that the stronger di- $\sigma$  interaction favors dehydrogenation.<sup>1</sup>

Referencing the literature augments our interpretations, as ethylene dehydrogenation has been thoroughly studied via DFT and various surface analysis methods over extended Pt surfaces. For example, for temperatures around 100 K, LEED showed ethylene adsorption having a clear preference for di- $\sigma$  adsorption to Pt(100)<sup>48</sup> and Pt(111).<sup>49</sup> In contrast, EELS analysis of stepped/lower-coordinated Pt sites (Pt(210) and Pt(110)) showed  $\pi$ -binding of ethylene.<sup>50</sup> The di- $\sigma$  binding was probed using TPD of mixed C<sub>2</sub>D<sub>4</sub> and C<sub>2</sub>H<sub>4</sub> adsorbed on Pt(111) by Janssens *et al.*, who reported recombinative desorption of isotope-scrambled ethylene at ~285 K, indicating dissociative adsorption.<sup>51</sup> Just above the 285 K desorption peak, hydrogen evolution begins, with the first H loss resulting in a surface-bound ethylidyne, although this is largely considered to be a

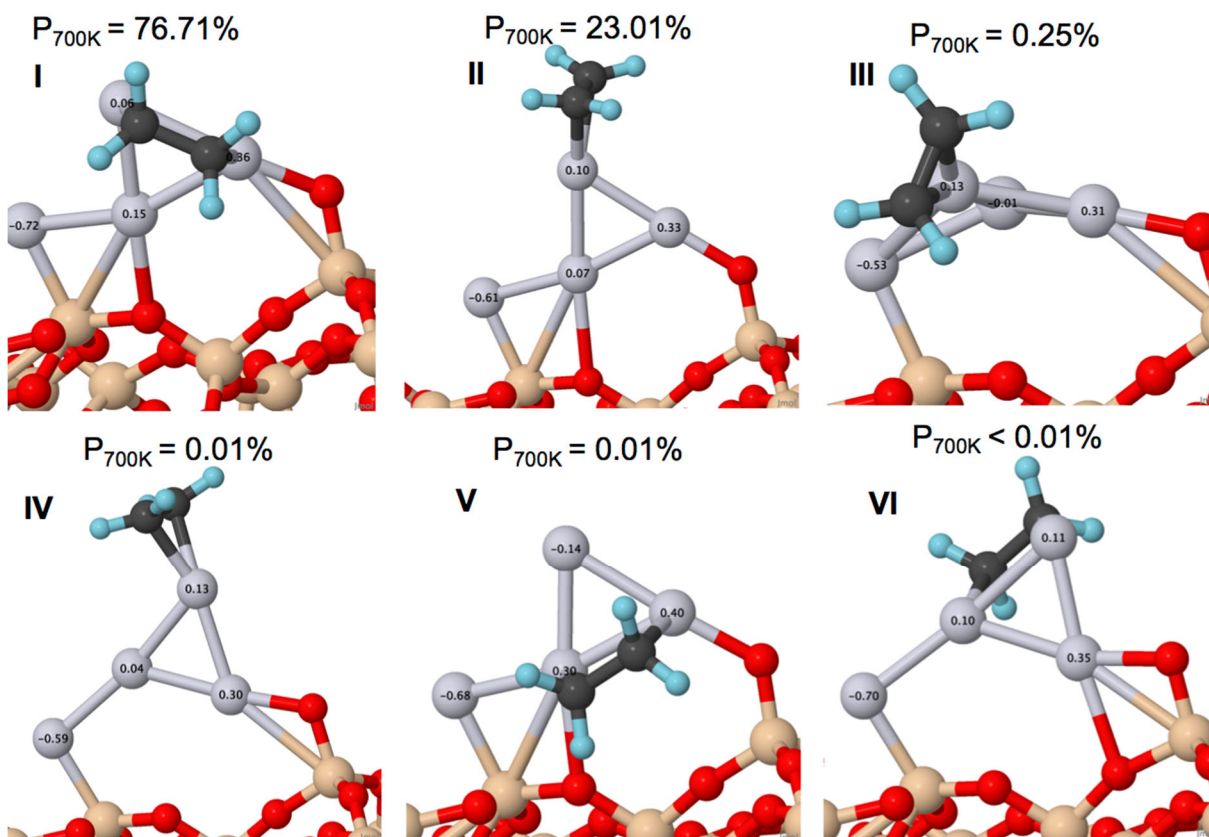


**Figure 8.** Thermally-accessible geometries of C<sub>2</sub>H<sub>4</sub>/Pt<sub>4</sub>/SiO<sub>2</sub> obtained from global optimization calculations. The geometries of (C<sub>2</sub>H<sub>4</sub>)<sub>2</sub>/Pt<sub>4</sub>/SiO<sub>2</sub> are shown in **Fig. S7**.

spectator between the first and remaining H dissociation events.<sup>52-54</sup> As the sample temperature continues to increase, additional dehydrogenation occurs, indicated by additional H<sub>2</sub> desorption until 700 K. Results for the  $\pi$ -bound molecules on low-coordinated stepped surfaces were quite different. For example Yagasaki *et al.* studied C<sub>2</sub>H<sub>4</sub> decomposition on Pt(210) and reported that some desorbs intact around 250 K, but the residual  $\pi$ -adsorbed C<sub>2</sub>H<sub>4</sub> undergoes dehydrogenation around 300 K, as shown by desorption of H<sub>2</sub> and detection of surface ethylidyne with both C atoms coordinated to the surface. Further heating the Pt(210) surface to 700 K drives dehydrogenation to completion.

Pt(110) showed different behavior, as reported by Yagasaki *et al.* Here, some of the  $\pi$ -adsorbed ethylene is isomerized to the di- $\sigma$  mode by 160 K. From 270 K–330 K, it undergoes decomposition to both C atoms and ethylidyne surface species, while evolving methane and hydrogen. The strongly bound ethylidyne then completes dehydrogenation by 450 K. For comparison, an IR absorption study<sup>55</sup> was done on Al<sub>2</sub>O<sub>3</sub>-supported Pt nanoparticles around 180 K that resulted in three ethylene adsorption modes:  $\pi$ -adsorption, di- $\sigma$  adsorption, and spontaneous ethylidyne formation. Interestingly, all  $\pi$ -adsorbed ethylene was found to desorb intact by room temperature, while the di- $\sigma$  bound ethylene is converted to ethylidyne and hydrogen.

Interpretation of our DFT and experimental results in light of these results allows conclusions to be made about the mechanism in our Pt<sub>n</sub>/SiO<sub>2</sub> experiments. The three structures I, II, and III shown in **Fig. 8** and structure I in **Fig. S7** each have significant contributions to the cluster ensemble and we thus expect surface-bound ethylene species to adsorb in both the  $\pi$  and di- $\sigma$  modes. We consider the comment by Mohsin *et al.*, that ethylidyne can spontaneously form at this temperature (as a result of dissociation of surface ethylene). In a D<sub>2</sub> thermal desorption study for Pt(100), Pasteur *et al.* showed recombinative desorption between 250 K and 500 K.<sup>56</sup> Spontaneous D<sub>2</sub>



desorption is therefore not expected; rather we would expect these species to exist as surface-bound.

The calculated structures for ethylene on bare Pt<sub>4</sub>/SiO<sub>2</sub> offer some explanation for the ISS experiments, which were conducted at 150 K, where only the lowest energy isomers are accessible, and all Pt atoms are in the surface layer. This results in the highest scattering intensity for as-deposited Pt<sub>4</sub> clusters, when compared to larger, multilayered clusters.<sup>1</sup> At higher temperatures, the catalytic activity observed experimentally is a result of a linear combination of the populated structures and the mechanisms they individually promote. With a combination of binding modes, diverse chemical behavior is expected, where both intact desorption of ethylene and dehydrogenation of ethylene would be expected, as observed.

In bulk, calorimetric experiments by Anres *et al.* showed that PtSn has a highly negative enthalpy of formation.<sup>57</sup> Similarly, Liu and Ascencio reported DFT simulations for clusters of a few hundred atoms that found PtSn clusters to be energetically favorable compared to pure Pt clusters.<sup>58</sup> For sub-nano clusters, DFT shows that Sn incorporation to size-selected Pt clusters results in substantial electron transfer from Sn to Pt atoms, and reduces the fluxionality of the clusters, such that one isomer dominates the ensemble.<sup>2</sup> The dominant isomer is an intermixed Pt<sub>4</sub>Sn<sub>3</sub> structure, with each atom showing a relatively high degree of coordination. From the chemistry perspective, one important result was that adding Sn quenches all unpaired spins on Pt, while in the pure Pt<sub>4</sub>/SiO<sub>2</sub> system there are low energy isomers with unpaired electrons available for adsorbate binding.

To examine the effects of ethylene adsorption on PtSn clusters, DFT calculations were performed for ethylene adsorbed on both the global minimum Pt<sub>4</sub>Sn<sub>3</sub>/SiO<sub>2</sub> structure, and on several of the lowest energy isomers. The lowest energy isomer changes when ethylene is adsorbed, thus

we expect the isomer ensemble to change as the clusters are heated with adsorbed ethylene. The most stable isomers for  $C_2H_4/Pt_4Sn_3/SiO_2$  are shown in **Fig. 9**, along with Boltzmann population and Bader charge data. Structures with two adsorbed ethylene molecules are shown in **Fig. S8**. As shown in **Fig. 9**, the most stable isomers for a single ethylene have it  $\pi$ -bonded to Pt atoms in the cluster, however, as shown **Fig. S8**, one isomer was found for  $(C_2D_4)_2/Pt_4Sn_3$  in which one of ethylene molecules is bound with one C atom bound to Sn, and one to an adjacent Pt atom. Note that for a single ethylene, di- $\sigma$  binding has been completely eliminated by incorporation of Sn into

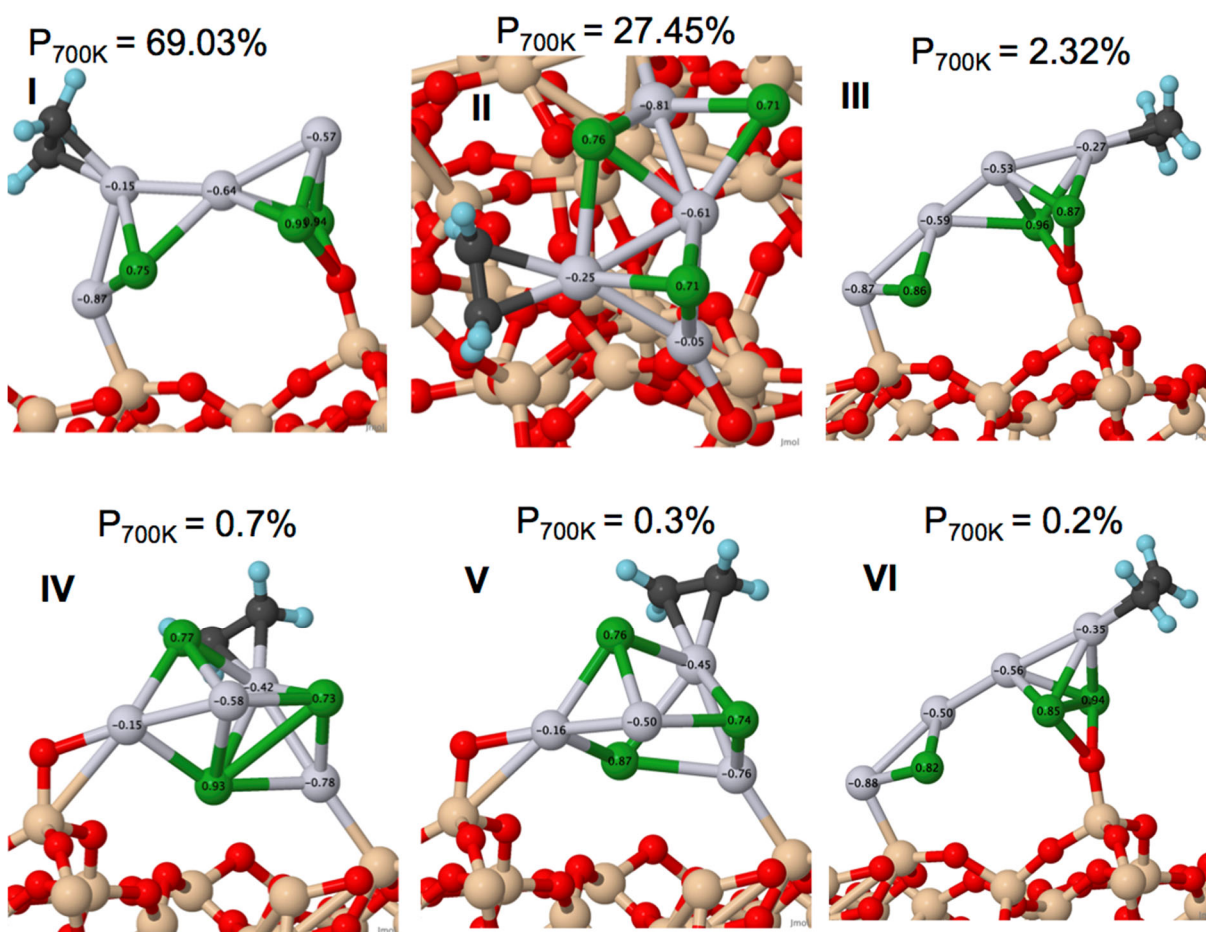


**Figure 9.** Thermally-accessible geometries of  $C_2H_4/Pt_4Sn_3/SiO_2$  obtained from global optimization calculations. Note that the ensemble is dominated by  $C_2H_4$   $\pi$ -binding mode. The geometries of  $(C_2H_4)_2/Pt_4Sn_3/SiO_2$  are shown in **Fig. S8**.

the Pt<sub>4</sub> clusters. Structure I is the preferred C<sub>2</sub>H<sub>4</sub>/Pt<sub>4</sub>Sn<sub>3</sub>/SiO<sub>2</sub> isomer, with greater than 69% of the population at 700 K. The only structure with di-σ C<sub>2</sub>H<sub>4</sub> is structure II for adsorption of two ethylene molecules (**Fig. S8**). While there is still some diversity in the lowest energy isomer distribution, C<sub>2</sub>H<sub>4</sub> is only able to adsorb via π interaction, which is expected to limit the catalytic branching toward the products of deeper dehydrogenation on the Pt<sub>4</sub>Sn<sub>3.3</sub>/SiO<sub>2</sub> catalyst.

In order to compare the barriers of C<sub>2</sub>H<sub>4</sub> dehydrogenation on Pt<sub>4</sub>/SiO<sub>2</sub> vs. Pt<sub>4</sub>Sn<sub>3</sub>/SiO<sub>2</sub>, CI-NEB calculations were done on the three structures of Pt<sub>4</sub>/SiO<sub>2</sub> and Pt<sub>4</sub>Sn<sub>3</sub>/SiO<sub>2</sub> that are most populated at 700 K. For every structure, the barrier to break each of the four C-H bonds is considered. The minimum energy pathway for each isomer along with the structures of reactants, transition states, and products are shown in **Fig. 10**. Additional CI-NEB reaction paths for other isomers and ethylene binding sites, along with the structures involved, are summarized in **Figs S9 - S13**.

The lowest reaction barrier of the most populated C<sub>2</sub>H<sub>4</sub>/Pt<sub>4</sub>/SiO<sub>2</sub> structure is 0.95 eV, whereas this value for C<sub>2</sub>H<sub>4</sub>/Pt<sub>4</sub>Sn<sub>3</sub>/SiO<sub>2</sub> is 1.29 eV. Isomer II of C<sub>2</sub>H<sub>4</sub>/Pt<sub>4</sub>Sn<sub>3</sub>/SiO<sub>2</sub> has a more accessible low-energy path (1.00 eV) which makes it the most active of the three lowest-energy isomers of the system. This confirms our working hypothesis that the less stable isomers tend to be more reactive, and they must be considered in order to accurately describe the catalytic properties of dynamic catalysts. Of course, the contributions of the isomers II and III to the reaction is smaller because of their smaller presence in the ensemble (see **Figs. 8 and 9**).

Additionally, **Fig. 11** gives the values for the 700 K ensemble-average rate constants ( $k_{ens}$ ) for C<sub>2</sub>H<sub>4</sub>/Pt<sub>4</sub>/SiO<sub>2</sub> and C<sub>2</sub>H<sub>4</sub>/Pt<sub>4</sub>Sn<sub>3</sub>/SiO<sub>2</sub> along with the rate constant calculated for each isomer, and the contribution of that isomer to the ensemble. The results show that the Pt<sub>4</sub>/SiO<sub>2</sub> ensemble is more active at 700 K toward ethylene dehydrogenation than the Pt<sub>4</sub>Sn<sub>3</sub>/SiO<sub>2</sub> ensemble. At lower temperatures, such as the ~300 K onset temperature for dehydrogenation, the difference would be

larger. These results confirm the experimental finding that introducing Sn to the cluster makes it

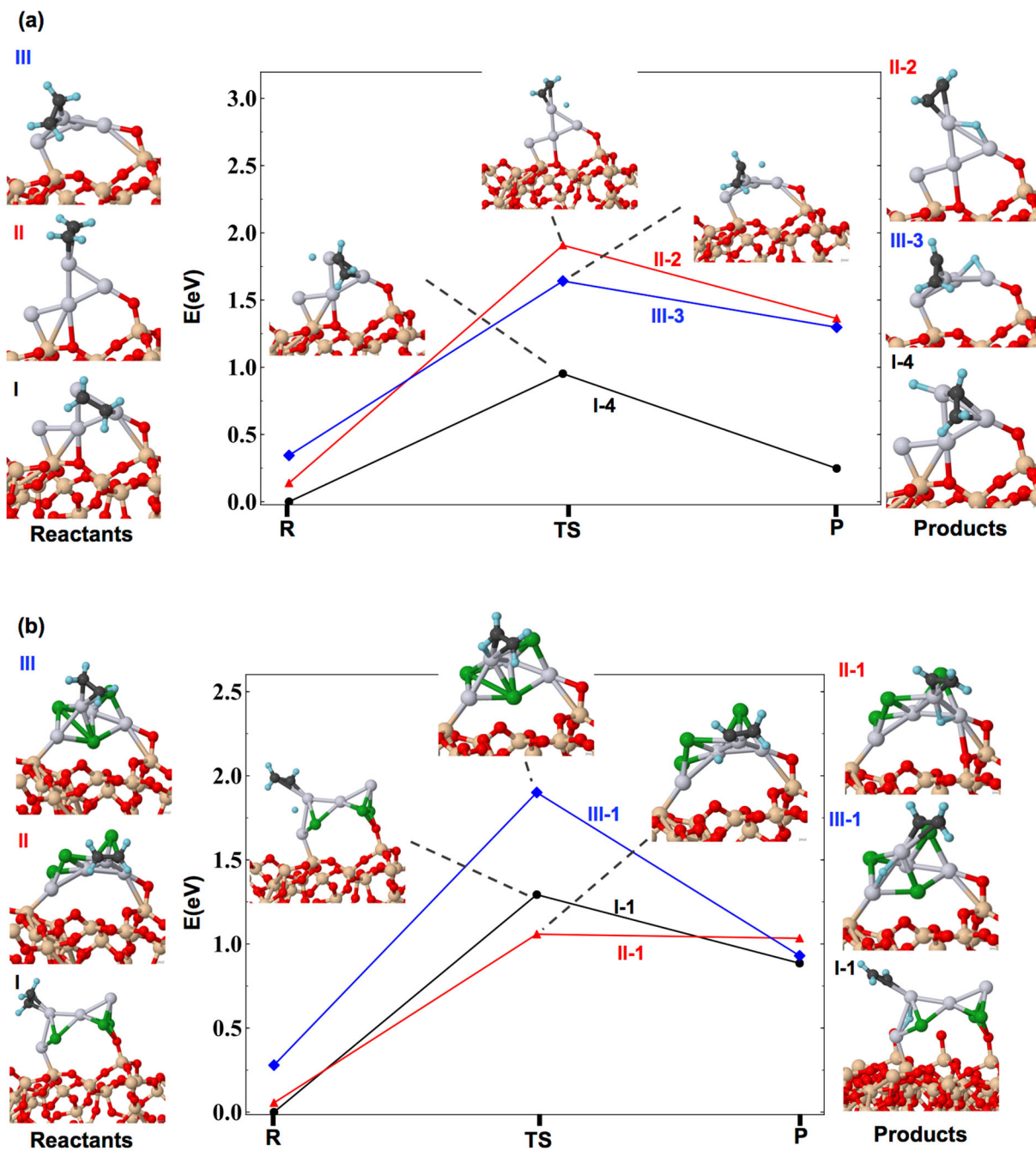


**Figure 10.** Lowest energy reaction profiles of breaking C-H bond obtained from CI-NEB calculations for each isomer of (a)  $C_2H_4/Pt_4/SiO_2$  and (b)  $C_2H_4/Pt_4Sn_3/SiO_2$  along with the structures of reactants, transition states, and products.

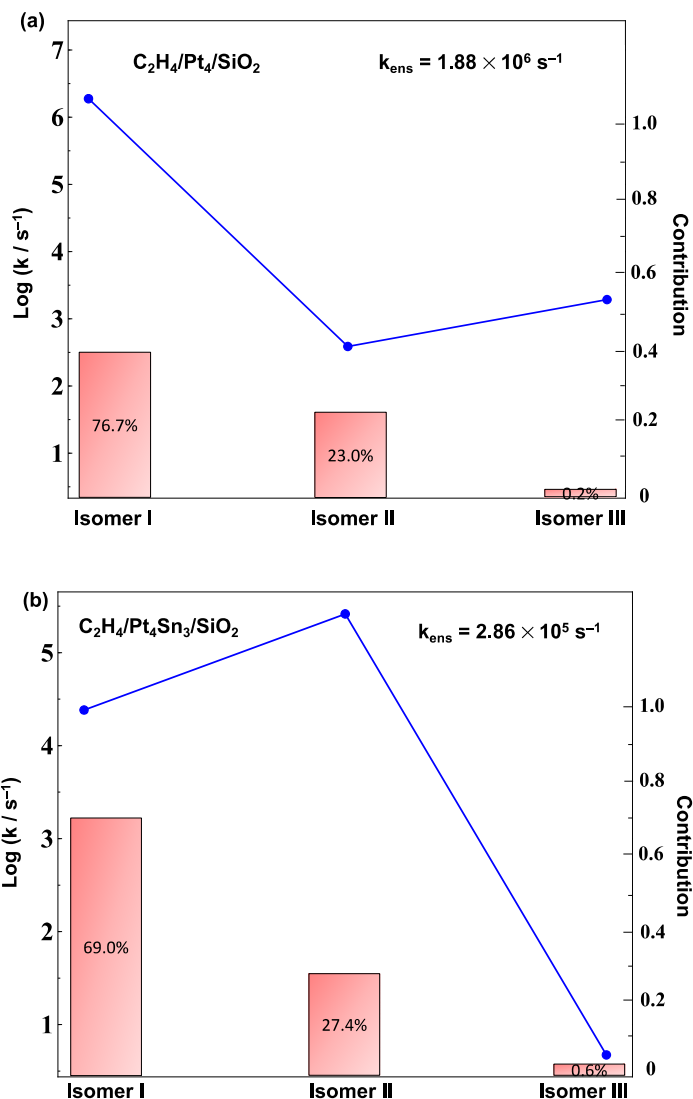


**Figure 11.** (a) Calculated rate constants along with their corresponding contribution to the  $k_{ens}$  at 700 K for each isomer of (a) C<sub>2</sub>H<sub>4</sub>/Pt<sub>4</sub>/SiO<sub>2</sub> and (b) C<sub>2</sub>H<sub>4</sub>/Pt<sub>4</sub>Sn<sub>3</sub>/SiO<sub>2</sub>. As expected, Pt<sub>4</sub>/SiO<sub>2</sub> is more active than Pt<sub>4</sub>Sn<sub>3</sub>/SiO<sub>2</sub> toward ethylene dehydrogenation.

harder for C<sub>2</sub>H<sub>4</sub> to undergo dehydrogenation.

Another interesting result is that on many cluster isomers, two of the hydrogens of ethylene can be removed significantly more easily than the other two. For instance, according to the C<sub>2</sub>H<sub>4</sub>/Pt<sub>4</sub>/SiO<sub>2</sub> isomer I reaction pathways in **Fig. S9**, the barriers corresponding to breaking C-H<sub>3</sub> and C-H<sub>4</sub>, which are plotted as I-3 and I-4, are almost 2 eV lower than those of C-H<sub>1</sub> and C-H<sub>2</sub> (I-1

and I-2). This can be understood by structure analysis (**Fig. S10**): the Pt atoms on the top of the cluster are more undercoordinated and active than the Pt atoms attached to the surface; thus, placing the detached H atoms on the top Pt sites is favorable (on either atop or bridge sites).

Note that all reaction profiles obtained from CI-NEB calculations along with the structures can be found in **Figs. S9–13**, and the corresponding numerical data is summarized in **Table S1**. By comparing these structures, we find that on Pt<sub>4</sub>Sn<sub>3</sub>/SiO<sub>2</sub>, in the product state, the Pt-C bonds between C<sub>2</sub>H<sub>3</sub> and the catalyst are elongated, compared to those on Pt<sub>4</sub>/SiO<sub>2</sub>. This suggests that the product might more easily leave Pt<sub>4</sub>Sn<sub>3</sub>/SiO<sub>2</sub> (or recombine and leave), whereas it is more likely to undergo further dehydrogenation on Pt<sub>4</sub>/SiO<sub>2</sub>.

Additionally, the properties of the ensemble of clusters with one and two adsorbed C<sub>2</sub>H<sub>4</sub> are summarized in **Tables S2** and **S3**. As can be seen, the Pt<sub>4</sub> cluster has negative charge due to electron transfer from the support, while the charge of Pt<sub>4</sub>Sn<sub>3</sub> is positive, as expected from the more electropositive nature of Sn. Moreover, the ethylene binding energy of Pt<sub>4</sub>Sn<sub>3</sub>/SiO<sub>2</sub> is ~0.7–0.8 eV weaker than that of Pt<sub>4</sub>/SiO<sub>2</sub> as is clear from **Table S3**; this makes it easier for ethylene to desorb from the cluster rather than undergo further dehydrogenation.

Next, MD simulations were run for 10 ps at 700 K to allow sampling of the adsorbate and cluster motion. The average C-C bond distance in C<sub>2</sub>H<sub>4</sub>/Pt<sub>4</sub>Sn<sub>3</sub>/SiO<sub>2</sub> is 0.1 Å shorter than that in C<sub>2</sub>H<sub>4</sub>/Pt<sub>4</sub>/SiO<sub>2</sub>, consistent with its looser binding to the PtSn clusters, and indicating the bond being closer to double in character (**Figs. S14 and S15**). Furthermore, the average ∠PtCC bond angle in C<sub>2</sub>H<sub>4</sub>/Pt<sub>4</sub>/SiO<sub>2</sub> is very close to the tetrahedral angle (104.94 °) showing the σ-bonding interaction between ethylene and the cluster. On the other hand, the average ∠HCC bond angle in C<sub>2</sub>H<sub>4</sub>/Pt<sub>4</sub>Sn<sub>3</sub>/SiO<sub>2</sub> is 120.47 ° showing a significant C-C double bond nature and π interaction between the adsorbate and the cluster. Note that during the MD simulations of C<sub>2</sub>H<sub>4</sub>/Pt<sub>4</sub>Sn<sub>3</sub>/SiO<sub>2</sub>,

ethylene becomes partially detached from the cluster at 5.059 ps, which is shown in **Fig. S17**, whereas on  $C_2H_4/Pt_4/SiO_2$  ethylene is always attached to the cluster. This again suggests that ethylene is more likely to desorb from the  $Pt_4Sn_3/SiO_2$  surface, rather than remaining on the surface and undergoing dehydrogenation.

Ethane-to-ethylene conversion is the ultimate target for these catalysts, but in UHV experiments, it is infeasible to probe  $C_2D_6$  dehydrogenation over  $Pt_n/SiO_2$  and  $Pt_nSn_x/SiO_2$ , because ethane does not stick at relevant temperatures. However, DFT can be useful to bridge the gap. We performed calculations of  $C_2H_6$  dehydrogenation on the pure and Sn-alloyed Pt clusters, to show that PtSn clusters can actually dehydrogenate  $C_2H_6$  and form the desired  $C_2H_4$  product. **Fig. 12** shows the barriers corresponding to ethane dehydrogenation on the  $Pt_4/SiO_2$  and  $Pt_4Sn_3/SiO_2$  global minimum structures. The reaction barriers are 0.22 eV for  $Pt_4/SiO_2$ , and 0.58 eV for  $Pt_4Sn_3/SiO_2$ , i.e. lower than the ones obtained for  $C_2H_4$  dehydrogenation (0.96 eV and 1.30 eV, for  $Pt_4/SiO_2$  and  $Pt_4Sn_3/SiO_2$ , respectively). The reason PtSn can dehydrogenate ethane relatively easily, but not ethylene, has to do with the type of sites required for the two reactions. Whereas di- $\sigma$  ethylene activation requires the binding to two Pt atoms, ethane binds to a single Pt atom with both the H and the C atoms of the activated C-H bond. Such sites are available on both pure and Sn-alloyed Pt clusters. These results suggest that both catalysts should successfully dehydrogenate alkanes, whereas dehydrogenation of alkenes is harder, and further hindered by alloying of the cluster catalyst with Sn. This justifies the use of  $C_2H_4$  as a model for selectivity of dehydrogenation catalysis.

In the past, we proposed that Si and Ge as new highly competitive alloying elements for Pt.<sup>59-60</sup> Both Si and Ge have very similar effect on Pt clusters to the effect of Sn: mixing, Pt site separations, and electronic spin quenching. Both Ge and Si were shown to suppress

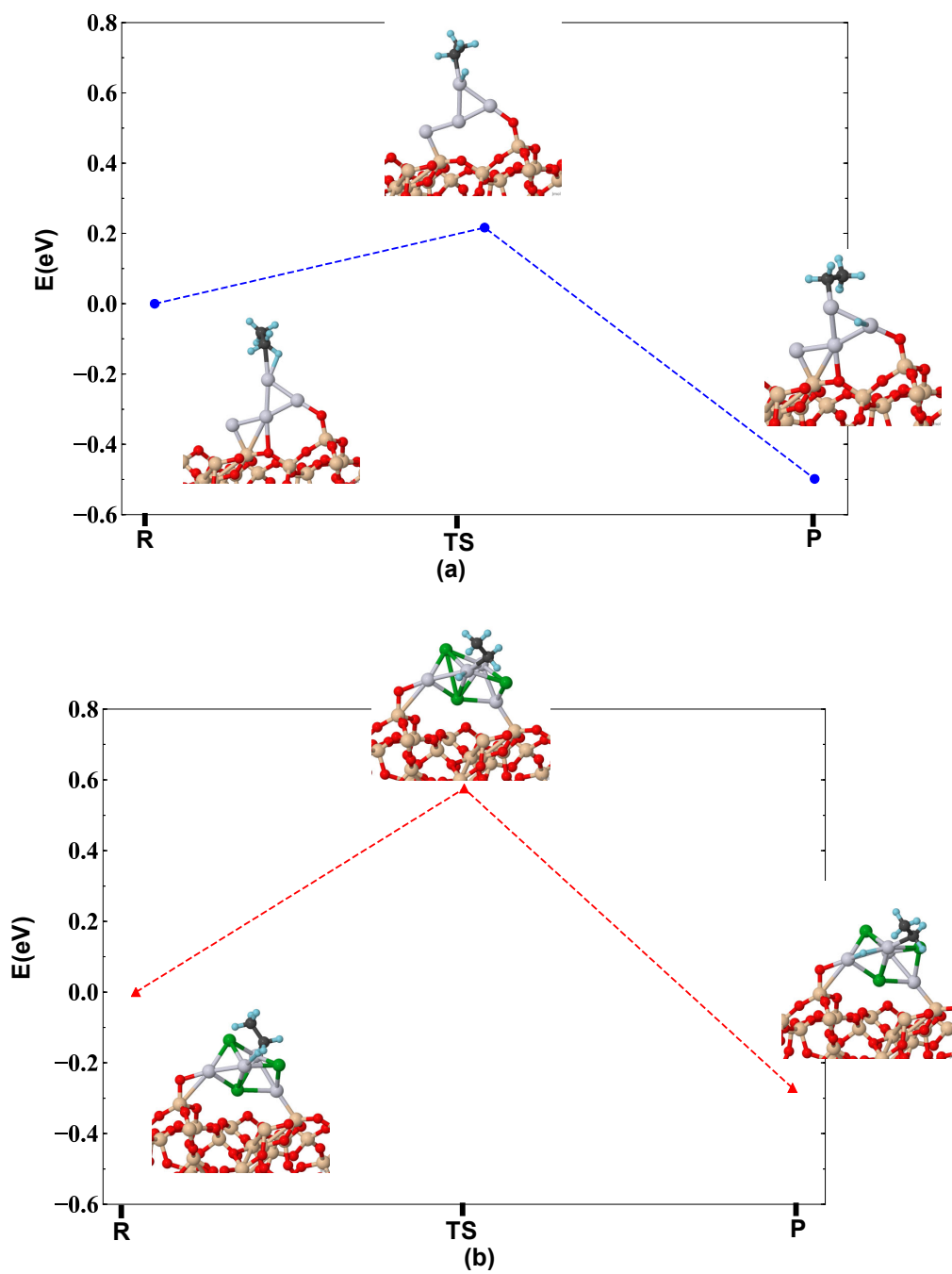


**Figure 12.** Lowest energy reaction profiles of breaking C-H bond obtained from CI-NEB calculations for the global minimum isomer of (a)  $C_2H_6/Pt_4/SiO_2$  and (b)  $C_2H_6/Pt_4Sn_3/SiO_2$  along with the structures of reactants, transition states, and products.



dehydrogenation beyond ethylene. However, for PtGe, the step of ethane dehydrogenation was actually accelerated compared to the process on pure Pt, and that is different from the effect of Sn, which makes ethane dehydrogenation less facile (though still quite accessible).

## CONCLUSIONS

We have presented a study comparing the activity and selectivity of Pt<sub>n</sub>/SiO<sub>2</sub> and Pt<sub>n</sub>Sn<sub>x</sub>/SiO<sub>2</sub> for ethylene desorption vs. dehydrogenation and carbon deposition. Alloying of sub-nano Pt<sub>n</sub> clusters with Sn resulted in considerable improvement in selectivity by blocking the di-σ binding mode of ethylene, while preserving the π-mode. The origin of this selectivity is electronic and geometric. Adding Sn quenches all unpaired spins on Pt, which are required for the di-σ ethylene binding. Also, Sn intermixes with Pt and separates Pt atoms from each other, thus again preventing di-σ ethylene binding. This resulted in suppression of the dehydrogenation mechanism, allowing ethylene to desorb from the catalytic surface intact before decomposition into high binding energy coke precursor surface species. The improvement in catalyst selectivity thus results in an improvement in run-to-run stability, suggesting that sub-nano PtSn alloy clusters could be a promising candidate for high temperature dehydrogenation catalysts.

On the mechanistic side, we find that many different pathways can feasibly contribute to the reaction mechanism, due to the co-existence of multiple cluster isomers, multiple binding geometries of ethylene to the clusters, and multiple accessible C-H bond dissociation paths. Metastable cluster isomers with attached ethylene can have lower barriers to C-H dissociation than the corresponding global minima of the same stoichiometry, and thus contribute substantially to the overall ensemble-average rate of the reaction. It is indeed important that the selectivity of the cluster catalyst is an ensemble property. Pure Pt cluster catalysts usually bind ethylene in the di-

$\sigma$  mode and efficiently dehydrogenate it, but they can also bind ethylene in the  $\pi$ -mode that discourages dehydrogenation and have high reaction barriers that are within thermal reach to the population. PtSn clusters, on the other hand, mostly favor the  $\pi$ -mode of ethylene binding, favoring desorption instead of dehydrogenation, however, to the extent that some higher energy cluster isomers contribute, they may have thermally-accessible dehydrogenation pathways. DFT calculations combined with statistical analysis confirm that adding Sn to Pt clusters significantly slows down ethylene dehydrogenation.

## METHODS

**Experimental.** Experiments were performed using an instrument described in detail elsewhere,<sup>3, 5, 61-62</sup> which allows sample creation by size-selected cluster deposition in ultra-high vacuum (UHV), with characterization of physical and chemical properties in *in situ*. The cluster deposition beamline includes a laser vaporization cluster source, ion guides for transport through several differential pumping stages, a quadrupole mass filter for cluster size selection, a valve/lens that isolates the cluster beamline from the UHV system, and a final ion guide that transports ions to the sample, where they are deposited through a 2 mm diameter mask. Samples are mounted via heater wires to a liquid N<sub>2</sub> cryostat that is mounted to a precision manipulator on a rotating “lid” assembly that allows samples to be positioned for sample exchange, cleaning, film growth, cluster deposition, and characterization. Temperature can be controlled in the range from ~120 K to 2100 K.

The UHV section (base pressure  $1.0 \times 10^{-10}$  Torr) includes capabilities for X-ray and UV photoelectron spectroscopy, low energy He<sup>+</sup> ion scattering spectroscopy, and ion neutralization electron spectroscopy, with analysis area set to 1.1 mm diameter, i.e., smaller than the 2.0 mm

cluster spot. The instrument is also equipped with a differentially pumped mass spectrometer that views the sample through a 2.5 mm diameter aperture in the end of skimmer cone. The cone is surrounded by dosing tubes that are connected to either leak valves or pulsed valves, allowing calibrated continuous or pulsed gas doses with local pressure at the sample position roughly an order of magnitude higher than the increase in background pressure.

A small UHV-compatible antechamber chamber is attached to the main UHV section, isolated by a gate valve. When the valve is opened, the sample can be inserted into the antechamber, and when in position, the two chambers are isolated by a triple differentially pumped seal that mates to the cryostat. This allows the antechamber to be vented for sample exchange, or used for “gassy” processes such as annealing in O<sub>2</sub> or Sn deposition, without exposing the main UHV system to high gas loads.

Model Pt<sub>n</sub>/SiO<sub>2</sub>/Si(100) and Pt<sub>n</sub>Sn<sub>x</sub>/SiO<sub>2</sub>/Si(100) catalysts were prepared on substrates consisting of 10 mm x 14 mm pieces of oxidized Si(100), using a fresh substrate for each experiment. The SiO<sub>2</sub>/Si(100) substrates are referred to throughout as “SiO<sub>2</sub>” substrates. Substrates were cleaned by annealing at 700 K in 5.0 x 10<sup>-6</sup> Torr O<sub>2</sub> for 20 minutes, followed by 2 min of annealing in UHV. After cleaning, the initial adventitious carbon from air exposure was largely removed, but a small C 1s signal remaining, which we roughly estimated to be ~ ~0.1 ML equivalent. We attempted to remove this residual carbon by sputtering, followed by various annealing protocols in both vacuum and O<sub>2</sub> at temperatures up to 1100 K, and while sputtering does remove the carbon, it creates a large number of defect sites that do not completely anneal away. These create large desorption signals during temperature-programmed desorption (TPD) experiments, interfering with detection of species desorbing from the low coverage of clusters, therefore, we opted to use just O<sub>2</sub> annealing for sample cleaning.

The thickness of the oxidized surface layer was estimated to be 1.1 nm, from modeling<sup>39</sup> of the Si<sup>4+</sup> and Si<sup>0</sup> relative intensities measured by XPS, with photoemission cross sections and asymmetry parameters taken from work by Yeh and Lindau<sup>63</sup> and electron effective attenuation lengths calculated using the NIST EAL database program of Powell and Jablonski.<sup>64</sup> Prior to cluster deposition, the sample cryostat was cooled, and then the sample was flashed to 700 K to drive off any adventitious species that might have adsorbed during cooling. As the sample cooled after the 700 K flash, Pt<sub>n</sub> cluster deposition was initiated once the sample reached 300 K and continued as the sample cooled to 180 K. To allow easy exchange of SiO<sub>2</sub> substrates, they are mounted using a tungsten clip to clamp the substrates to a molybdenum backing plate, which is spot welded to Ta heater wires that also act as thermal conductors to the sample cryostat. A type C thermocouple is spot welded to back of the backing plate for temperature measurement.

We chose to study two small clusters, Pt<sub>4</sub> and Pt<sub>7</sub>, both deposited at ~1 eV/atom, as measured using retarding potential analysis of the ion beam on the substrate. Deposition was monitored by integrating the Pt<sub>n</sub><sup>+</sup> neutralization current, and for all samples here, the coverage was 1.5 x 10<sup>14</sup> Pt atoms/cm<sup>2</sup>, equivalent to ~10% of a close-packed Pt monolayer. The absolute coverage of clusters is thus 1.5x10<sup>14</sup>/n clusters/cm<sup>2</sup>, where n = 4 or 7.

The method used to prepare size- and composition-selected PtSn alloy clusters, along with experimental and theoretical characterization of the cluster properties, has been described in detail,<sup>2</sup> and additional information is given in the Supporting Information. Briefly, size-selected Pt<sub>n</sub> (n = 4, 7) clusters deposited on SiO<sub>2</sub> substrates were used to “seed” selective Sn deposition via a self-limiting reaction sequence, carried out at 300 K. Pt<sub>n</sub>/SiO<sub>2</sub> samples were first exposed to ~21000 L of H<sub>2</sub>, which saturates the Pt clusters with H atoms, with essentially no effect on the SiO<sub>2</sub> substrate.<sup>5</sup> Next, the samples were exposed to ~24 L of SnCl<sub>4</sub> vapor, which reacts with

hydrogenated Pt sites, leading to HCl desorption and binding of SnCl<sub>x</sub>. The samples were then exposed to an additional 21000 L of H<sub>2</sub>, causing additional HCl desorption, such that <10% of the Cl remained on the cluster surface, along with H and Sn. Finally, the samples were heated briefly to 700 K, desorbing the remaining H and Cl, but with no loss of Sn. ISS showed evidence that heating also allowed the Sn to mix into the Pt cluster, forming an alloy.

Sn deposition was found to be >40 times more efficient on hydrogenated Pt sites than on the SiO<sub>2</sub> support. The cluster Pt:Sn stoichiometry estimated by XPS for the Pt<sub>4</sub> and Pt<sub>7</sub> seed clusters (Pt<sub>4</sub>Sn<sub>3.3</sub>, Pt<sub>7</sub>Sn<sub>6.3</sub>) was close to 1:1. It is important to note that the Pt:Sn stoichiometry is unaffected by increasing the reactant exposures,<sup>2</sup> i.e., the stoichiometry is controlled by the seed cluster size<sup>2</sup> and the saturation coverage of the ALD reactants on the clusters. Therefore, we expect that the stoichiometry to be reasonably uniform from cluster to cluster, at least as initially prepared.

Desorption and dehydrogenation of ethylene on Pt<sub>n</sub>/SiO<sub>2</sub> and Pt<sub>n</sub>Sn<sub>x</sub>/SiO<sub>2</sub> was characterized by C<sub>2</sub>D<sub>4</sub> TPD/R. Samples were cooled to 180 K and exposed to 10 L of C<sub>2</sub>D<sub>4</sub>, which is roughly twice the dose needed to saturate cluster-associated binding sites that are stable at this temperature.<sup>1</sup> 180 K was chosen to minimize adsorption on the amorphous SiO<sub>2</sub> substrate. After the C<sub>2</sub>D<sub>4</sub> exposure, samples were positioned 0.5 mm away from the 2.5 mm diameter aperture that allows desorbing molecules to pass into the ion source of the differentially pumped mass spectrometer (UTI 100C with Extrel electronics). The sample temperature was then ramped at 3 K/sec up to 700 K, while monitoring signal for D<sub>2</sub><sup>+</sup>, H<sub>2</sub>O<sup>+</sup>, <sup>12</sup>CO<sup>+</sup>, <sup>13</sup>CO<sup>+</sup>, C<sub>2</sub>D<sub>4</sub><sup>+</sup>, H<sup>35</sup>Cl<sup>+</sup>, <sup>12</sup>CO<sub>2</sub><sup>+</sup>, <sup>13</sup>CO<sub>2</sub><sup>+</sup>, and Cl<sub>2</sub><sup>+</sup>.

CO TPD was used to examine changes in the number and properties of accessible Pt sites accompanying the ethylene TPD experiments. As with the C<sub>2</sub>D<sub>4</sub> TPD/R experiments, samples were exposed to 10 L of <sup>13</sup>CO at 180 K, then positioned 0.5 mm away from the 2.5 mm diameter

skimmer cone aperture, and the sample temperature was ramped at 3 K/s, to 700 K while monitoring the same masses as above.

After completion of each set of TPD/R experiments, the sample was moved away from the aperture, and the mass spectrometer sensitivity was calibrated by leaking  $2.0 \times 10^{-8}$  Torr of  $C_2D_4$ ,  $D_2$ ,  $^{13}CO$ , and Ar into the main UHV chamber background. Taking the ionization gauge sensitivity into account, these background pressures create well-defined fluxes of the molecules of interest through the skimmer cone aperture into the mass spectrometer ionization source. Ar was used as a UHV-friendly calibrant for HCl. The masses are similar and should therefore have similar transmission efficiency, and the difference in ionization cross-sections was taken into account using ionization gauge sensitivity factors reported by the gauge manufacturer. This calibration information was used to convert ion signals for  $C_2D_4^+$ ,  $D_2^+$ ,  $CO^+$ , and  $H^{35}Cl^+$  to the corresponding number of desorbing molecules, based on the assumption that detection efficiency should be similar for molecules desorbing from the surface and effusing from the gas phase. We previously compared calibrations obtained by this method to calibration by desorption of well-defined (2x2)-CO layers from Pd single crystals, and obtained very similar results.<sup>40, 65</sup> We conservatively estimate that the *absolute* uncertainty in the calibrated desorption signals to be  $\sim\pm 50\%$ , with uncertainty for comparing experiment to experiment of  $\sim\pm 15\%$ .

**Computational.** Global optimization done in this study was performed based on plane wave density functional theory (PW-DFT) calculations with the Vienna Ab initio Simulation Package (VASP)<sup>66-69</sup> using projector augmented wave (PAW) potentials<sup>70</sup> and the PBE<sup>71</sup> functional. Plane waves were chosen based on the kinetic energy cutoff of 400.0 eV. Moreover, the convergence parameters of  $10^{-5}$  ( $10^{-6}$ ) eV for geometric(electronic) relaxations and Gaussian

smearing with the sigma value of 0.1 eV were used. In order to model the substrate used in the experiment, the chosen SiO<sub>2</sub> slab was previously optimized<sup>72</sup> elsewhere at the B3LYP/6-31G(d,p)<sup>73-76</sup> level. The obtained cell parameters used in this study are  $a = 12.4 \text{ \AA}$ ,  $b = 13.1 \text{ \AA}$ ,  $c = 32.0 \text{ \AA}$ ,  $\alpha = 90^\circ$ ,  $\beta = 90^\circ$ , and  $\gamma = 88^\circ$  which includes the vacuum gap of 10  $\text{\AA}$  in the z-direction. Note that the lower half of the slab was kept fixed during the global optimization and only the  $\Gamma$ -point sampling was used to obtain the energy thanks to the fairly large super cell used in this study.

The supported Pt<sub>4</sub> and Pt<sub>4</sub>Sn<sub>3</sub> clusters, without and with the adsorbed ethylene, were globally optimized. Larger Pt<sub>7</sub>-based clusters were not considered due to the enormous computational expense, additionally given the need for a larger super cell representing the slab. To produce the initial cluster geometries on the surface, we use our in-house code, parallel global optimization and pathway toolkit PGOPT, that automatically generates structures based on the bond length distribution algorithm (BLDA).<sup>43</sup> Initial structures for the global optimization calculations should be created, such that they are less prone to encounter Self-Consistent Field (SCF) convergence problems. This can be done by avoiding chemically unfavorable configurations, which results in the reduction of configuration search space and the computational cost of calculation. By constraining the distance of atoms to their closest and second closest neighbors to follow a normal distribution, one can achieve this goal. That is to say, both closest and second closest distances are fitted to normal distribution based on which the initial structures are generated. Subsequently, each generated structure was optimized using DFT and duplicate structures were removed thereafter. The ethylene molecules were placed on the clusters in a multitude of possible orientations and binding sites. Then each structure was optimized using DFT, and duplicates were filtered out. In this study, 200 unique structures were generated and optimized to find the putative global

minimum and the accessible local minima. To take into account the effect of coverage, we also optimized the clusters with two ethylene adsorbed per cluster. A cut-off energy of 0.4 eV was used to select the thermodynamically accessible isomers at relevant temperatures. More detailed discussion about obtaining the vibrational partition functions and corrected Boltzmann population was published before.<sup>43</sup> The Bader charge analysis<sup>77-80</sup> was used to obtain partial atomic charges. Furthermore, Boltzmann populations were calculated with the assumption that the system can sufficiently equilibrate as

$$P_i = \frac{Z_{elec,i} Z_{trans,i} Z_{vib,i} Z_{rot,i}}{\sum_i Z_i} \approx \frac{g_i e^{-\beta E_i}}{\sum_i g_i e^{-\beta E_i}}$$

where  $Z_{elec,i}$ ,  $Z_{trans,i}$ ,  $Z_{vib,i}$ , and  $Z_{rot,i}$  are electronic, translational, vibrational, and rotational partition functions, respectively. For the lowest-energy isomers with adsorbed ethylene, which contributed significantly into the respective thermal ensembles, the reaction profile for ethylene dehydrogenation were calculated using climbing image nudged elastic band (CI-NEB) method.<sup>81</sup> Three isomers of each cluster with adsorbed ethylene were chosen and the dissociation of every C-H bond within every adsorbed configuration was tested. All transition states were confirmed by phonon calculations. The distance between the structures (images) in CI-NEB calculations used as reaction coordinate is defined as

$$d_{12} = \sqrt{\frac{1}{N} \sum_i^N (x_{i,1} - x_{i,2})^2 + (y_{i,1} - y_{i,2})^2 + (z_{i,1} - z_{i,2})^2}$$

Rate constants for each pathway were calculated based on harmonic transition state theory.<sup>82</sup> The ensemble-average rate constant were calculated based on the contribution of each isomer using its Boltzmann population at 700 K:



$$k_{ens} = k_1P_1 + k_2P_2 + k_3P_3$$

, where  $P_i$  is the Boltzmann population and  $k_i$  ( $i = 1-3$ ) is the sum over all four pathway rate constants obtained from CI-NEB for isomer  $i$ .

Finally, *ab initio* MD simulations ran for 10 ps at 700 K with the time step of 1 fs starting from Pt<sub>4</sub>/SiO<sub>2</sub> and Pt<sub>4</sub>Sn<sub>3</sub>/SiO<sub>2</sub> global minimum structures. Nosé–Hoover thermostat was utilized for equilibration during the MD simulations.<sup>83</sup>

## ASSOCIATED CONTENT

### Supporting Information Available:

Contains complete sets of C<sub>2</sub>D<sub>4</sub> TPD for Pt<sub>n</sub>/SiO<sub>2</sub> and Pt<sub>n</sub>Sn<sub>x</sub>/SiO<sub>2</sub>, HCl desorption during the first C<sub>2</sub>D<sub>4</sub> TPD for Pt<sub>n</sub>Sn<sub>x</sub>/SiO<sub>2</sub>, an C 1s XPS regional spectra, the remaining Arrhenius fit plots for Pt<sub>7</sub>/SiO<sub>2</sub> and Pt<sub>7</sub>Sn<sub>6.3</sub>/SiO<sub>2</sub>, structures of reactants, products, transition states obtained from CI-NEB, Bader charge of all local minima structures along with their Boltzmann populations, Ethylene binding energies obtained from DFT, bond length and bond angle distribution of C<sub>2</sub>H<sub>4</sub>/Pt<sub>4</sub>/SiO<sub>2</sub> and C<sub>2</sub>H<sub>4</sub>/Pt<sub>4</sub>Sn<sub>3</sub>/SiO<sub>2</sub> obtained MD simulations, XYZ coordinates of minimum energy pathways obtained from CI-NEB.

## AUTHOR INFORMATION

### Corresponding Authors

\*(Scott L. Anderson, Anastassia N. Alexandrova) E-mails: anderson@chem.utah.edu, ana@chem.uscla.edu

### ORCIDs

Scott L. Anderson: 0000-0001-9985-8178

Anastassia Alexandrova: 0000-0002-3003-1911

Timothy J. Gorey: 0000-0002-7491-9648

Borna Zandkarimi: 0000-0002-7633-132X

### **Notes**

The authors declare no competing financial interest.

### **ACKNOWLEDGEMENT**

This work was supported by the U.S. Air Force Office of Scientific Research under AFOSR Grants FA9550-19-1-0261 and FA9550-16-1-0141.

## REFERENCES

1. Baxter, E. T.; Ha, M.-A.; Alexandrova, A.; Anderson, S. L., Ethylene Dehydrogenation on Pt<sub>4,7,8</sub> Clusters on Al<sub>2</sub>O<sub>3</sub>: Strong Cluster-Size Dependence Linked to Preferred Catalyst Morphologies. *ACS Catal.* **2017**, *7*, 3322-3335. DOI:10.1021/acscatal.7b00409
2. Gorey, T. J.; Zandkarimi, B.; Li, G.; Baxter, E. T.; Alexandrova, A. N.; Anderson, S. L., Preparation of Size and Composition Controlled Pt<sub>n</sub>Sn<sub>x</sub>/SiO<sub>2</sub> (n = 4, 7, 24) Bimetallic Model Catalysts with Atomic Layer Deposition. *J. Phys. Chem. C.* **2019**, *123* (26), 15. DOI:10.1021/acs.jpcc.9b02745
3. Baxter, E. T.; Ha, M.-A.; Cass, A. C.; Zhai, H.; Alexandrova, A. N.; Anderson, S. L., Diborane Interactions with Pt<sub>7</sub>/alumina: Preparation of Size-Controlled Boronated Pt Model Catalysts with Improved Coking Resistance. *J. Phys. Chem. C.* **2018**, *122*, 1631-1644. DOI:10.1021/acs.jpcc.7b10423
4. Ha, M.-A.; Baxter, E. T.; Cass, A. C.; L.Anderson, S.; Alexandrova, A. N., Boron Switch for Selectivity of Catalytic Dehydrogenation on Size-Selected Pt Clusters on Al<sub>2</sub>O<sub>3</sub>. *J. Am. Chem. Soc.* **2017**, *139*, 11568-11575. DOI:10.1021/jacs.7b05894
5. Dai, Y.; Gorey, T. J.; Anderson, S. L.; Lee, S.; Lee, S.; Seifert, S.; Winans, R. E., Inherent Size Effects on XANES of Nanometer Metal Clusters: Size-Selected Platinum Clusters on Silica. *J. Phys. Chem. C.* **2017**, *121*, 361-374. DOI:10.1021/acs.jpcc.6b10167
6. von Weber, A.; Scott L. Anderson, Electrocatalysis by Mass-Selected Pt<sub>n</sub> Clusters. *Acc. Chem. Res.* **2016**, *49*, 2632–2639. DOI:10.1021/acs.accounts.6b00387

7. Roberts, F. S.; Anderson, S. L.; Reber, A. C.; Khanna, S. N., Initial and Final State Effects in the Ultraviolet and X-ray Photoelectron Spectroscopy (UPS and XPS) of Size-Selected Pd<sub>n</sub> Clusters Supported on TiO<sub>2</sub>(110). *J. Phys. Chem. C* **2015**, *119* (11), 6033-6046.  
DOI:10.1021/jp512263w
8. Kaden, W. E.; Kunkel, W. A.; Kane, M. D.; Roberts, F. S.; Anderson, S. L., Size-Dependent Oxygen Activation Efficiency over Pd<sub>n</sub>/TiO<sub>2</sub>(110) for the CO Oxidation Reaction. *J. Am. Chem. Soc.* **2010**, *132*, 13097–13099. DOI:10.1021/ja103347v
9. Crampton, A. S.; Roetzer, M. D.; Schweinberger, F. F.; Yoon, B.; Landman, U.; Heiz, U., Ethylene Hydrogenation on Supported Ni, Pd and Pt Nanoparticles: Catalyst Activity, Deactivation and the d-band Model. *J. Catal.* **2016**, *333*, 51-58. DOI:10.1016/j.jcat.2015.10.023
10. Crampton, A. S.; Roetzer, M. D.; Ridge, C. J.; Schweinberger, F. F.; Heiz, U.; Yoon, B.; Landman, U., Structure Sensitivity in the Non-scalable Regime Explored via Catalyzed Ethylene Hydrogenation on Supported Platinum Nanoclusters. *Nat. Commun.* **2016**, *7*, 10389pp.  
DOI:10.1038/ncomms10389
11. Schweinberger, F. F.; Berr, M. J.; Doeblinger, M.; Wolff, C.; Sanwald, K. E.; Crampton, A. S.; Ridge, C. J.; Jaeckel, F.; Feldmann, J.; Tschurl, M.; Heiz, U., Cluster Size Effects in the Photocatalytic Hydrogen Evolution Reaction. *J. Am. Chem. Soc.* **2013**, *135* (36), 13262-13265.  
DOI:10.1021/ja406070q
12. Habibpour, V.; Wang, Z. W.; Palmer, R. E.; Heiz, U., Size-selected Metal Clusters: New Models for Catalysis with Atomic Precision. *J. Appl. Sci.* **2011**, *11* (7), 1164-1170.  
DOI:10.3923/jas.2011.1164.1170

13. Halder, A.; Curtiss, L. A.; Fortunelli, A.; Vajda, S., Perspective: Size Selected Clusters for Catalysis and Electrochemistry. *J. Chem. Phys.* **2018**, *148* (11), 110901/1-110901/15.  
DOI:10.1063/1.5020301
14. Vajda, S.; White, M. G., Catalysis Applications of Size-Selected Cluster Deposition. *ACS Catal.* **2015**, *5* (12), 7152-7176. DOI:10.1021/acscatal.5b01816
15. Tyo, E. C.; Vajda, S., Catalysis by Clusters with Precise Numbers of Atoms. *Nat. Nanotechnol.* **2015**, *10* (7), 577-588. DOI:10.1038/nnano.2015.140
16. Fukamori, Y.; Koenig, M.; Yoon, B.; Wang, B.; Esch, F.; Heiz, U.; Landman, U., Fundamental Insight into the Substrate-Dependent Ripening of Monodisperse Clusters. *ChemCatChem* **2013**, *5* (11), 3330-3341. DOI:10.1002/cctc.201300250
17. Harding, C.; Habibpour, V.; Kunz, S.; Farnbacher, A. N.-S.; Heiz, U.; Yoon, B.; Landman, U., Control and Manipulation of Gold Nanocatalysis: Effects of Metal Oxide Support Thickness and Composition. *J. Am. Chem. Soc.* **2009**, *131* (2), 538-548.
18. Sanchez, A.; Abbet, S.; Heiz, U.; Schneider, W. D.; Haekkinen, H.; Barnett, R. N.; Landman, U., When Gold Is Not Noble: Nanoscale Gold Catalysts. *J. Phys. Chem. A.* **1999**, *103* (48), 9573-9578.
19. Reber, A. C.; Khanna, S. N., Effect of N- and P-Type Doping on the Oxygen-Binding Energy and Oxygen Spillover of Supported Palladium Clusters. *J. Phys. Chem. C.* **2014**, *118*, 20306–20313. DOI:10.1021/jp5045145

20. Ong, S. V.; Khanna, S. N., Theoretical Studies of the Stability and Oxidation of Pd<sub>n</sub> (n = 1-7) Clusters on Rutile TiO<sub>2</sub>(110): Adsorption on the Stoichiometric Surface. *J. Phys. Chem. C.* **2012**, *116* (4), 3105-3111. DOI:10.1021/jp212504x
21. Zandkarimi, B.; Alexandrova, A. N., Dynamics of Subnanometer Pt Clusters Can Break the Scaling Relationships in Catalysis. *J. Phys. Chem. Lett.* **2019**, *10* (3), 460-467. DOI:10.1021/acs.jpcclett.8b03680
22. Jimenez-Izal, E.; Alexandrova, A. N., Computational Design of Clusters for Catalysis. *Annu. Rev. Phys. Chem.* **2018**, *69*, 377-400. DOI:10.1146/annurev-physchem-050317-014216
23. Moulijn, J. A.; van Diepen, A. E.; Kapteijn, F., Catalyst Deactivation: Is it Predictable?: What to do? *Appl. Catal. A. Gen.* **2001**, *212* (1), 3-16. DOI:10.1016/S0926-860X(00)00842-5
24. Wolf, E. E.; Alfani, F., Catalysts Deactivation by Coking. *Catal. Rev.* **1982**, *24* (3), 329-371. DOI:10.1080/03602458208079657
25. Trimm, D., Catalysts for the Control of Coking during Steam Reforming. *Catal. Today.* **1999**, *49* (1), 3-10.
26. Macleod, N.; Fryer, J. R.; Stirling, D.; Webb, G., Deactivation of Bi- and Multimetallic Reforming Catalysts: Influence of Alloy Formation on Catalyst Activity. *Catal. Today.* **1998**, *46* (1), 37-54. DOI:10.1016/S0920-5861(98)00349-6
27. Rovik, A. K.; Klitgaard, S. K.; Dahl, S.; Christensen, C. H.; Chorkendorff, I., Effect of Alloying on Carbon Formation during Ethane Dehydrogenation. *Appl. Catal. A. Gen.* **2009**, *358* (2), 269-278. DOI:10.1016/j.apcata.2009.02.020

28. Iglesias-Juez, A.; Beale, A. M.; Maaijen, K.; Weng, T. C.; Glatzel, P.; Weckhuysen, B. M., A Combined in situ Time-resolved UV–Vis, Raman and High-energy Resolution X-ray Absorption Spectroscopy Study on the Deactivation Behavior of Pt and PtSn Propane Dehydrogenation Catalysts under Industrial Reaction Conditions. *J. Catal.* **2010**, *276* (2), 268-279. DOI:10.1016/j.jcat.2010.09.018
29. Natal-Santiago, M.; Podkolzin, S.; Cortright, R.; Dumesic, J., Microcalorimetric Studies of Interactions of Ethene, Isobutene, and Isobutane with Silica-supported Pd, Pt, and PtSn. *Catal. Lett.* **1997**, *45* (3-4), 155-163.
30. Shen, J.; Hill, J. M.; Watwe, R. M.; Spiewak, B. E.; Dumesic, J. A., Microcalorimetric, Infrared Spectroscopic, and DFT Studies of Ethylene Adsorption on Pt/SiO<sub>2</sub> and Pt– Sn/SiO<sub>2</sub> Catalysts. *J. Phys. Chem. B.* **1999**, *103* (19), 3923-3934.
31. Tsai, Y.-L.; Xu, C.; Koel, B. E., Chemisorption of Ethylene, Propylene and Isobutylene on Ordered Sn/Pt(111) Surface Alloys. *Surf. Sci.* **1997**, *385* (1), 37-59.
32. Paffett, M. T.; Gebhard, S. C.; Windham, R. G.; Koel, B. E., Chemisorption of Ethylene on Ordered Tin/platinum(111) Surface Alloys. *Surf. Sci.* **1989**, *223* (3), 449-64.
33. Hook, A.; Massa, J. D.; Celik, F. E., Effect of Tin Coverage on Selectivity for Ethane Dehydrogenation over Platinum–tin Alloys. *J. Phys. Chem. C.* **2016**, *120* (48), 27307-27318. DOI:10.1021/acs.jpcc.6b08407
34. Pham, H. N.; Sattler, J. J.; Weckhuysen, B. M.; Datye, A. K., Role of Sn in the Regeneration of Pt/ $\gamma$ -Al<sub>2</sub>O<sub>3</sub> Light Alkane Dehydrogenation Catalysts. *ACS Catal.* **2016**, *6* (4), 2257-2264. DOI:10.1021/acscatal.5b02917

35. Li, G.; Zandkarimi, B.; Cass, A. C.; Gorey, T. J.; Allen, B. J.; Alexandrova, A. N.; Anderson, S. L., Sn-modification of Pt<sub>7</sub>/alumina Model Catalysts: Suppression of Carbon Deposition and Enhanced Thermal Stability. *J. Chem. Phys.* **2020**, *152* (2), 024702. DOI:10.1063/1.5129686
36. Windham, R. G.; Bartram, E.; Koel, B. E., Coadsorption of Ethylene and Potassium on Pt(111). 1. Formation of a pi-Bonded State of Ethylene. *J. Phys. Chem.* **1988**, *92*, 2862-2870.
37. Rabalais, J. W., *Principles and Applications of Ion Scattering Spectrometry : Surface Chemical and Structural Analysis*. Wiley: New York, 2003; p 336.
38. Aizawa, M.; Lee, S.; Anderson, S. L., Deposition Dynamics and Chemical Properties of Size-selected Ir Clusters on TiO<sub>2</sub>. *Surf. Sci.* **2003**, *542* (3), 253-275. DOI:10.1016/S0039-6028(03)00984-1
39. Kaden, W. E.; Kunkel, W. A.; Anderson, S. L., Cluster Size Effects on Sintering, CO Adsorption, and Implantation in Ir/SiO<sub>2</sub>. *J. Chem. Phys.* **2009**, *131*, 114701, 1-15. DOI:10.1063/1.3224119
40. Kaden, W. E.; Kunkel, W. A.; Roberts, F. S.; Kane, M.; Anderson, S. L., CO Adsorption and Desorption on Size-selected Pd<sub>n</sub>/TiO<sub>2</sub>(110) Model Catalysts: Size Dependence of Binding Sites and Energies, and Support-mediated Adsorption. *J. Chem. Phys.* **2012**, *136*, 204705/1-204705/12. DOI:10.1063/1.4721625
41. Kane, M. D.; Roberts, F. S.; Anderson, S. L., Mass-selected Supported Cluster Catalysts: Size Effects on CO Oxidation Activity, Electronic Structure, and Thermal Stability of



Pd<sub>n</sub>/alumina (n ≤ 30) Model Catalysts. *Int. J. Mass Spectrom.* **2014**, *370*, 1-15.

DOI:10.1016/j.ijms.2014.06.018 and see also 10.1016/j.ijms.2014.07.044

42. Kaden, W. E.; Kunkel, W. A.; Roberts, F. S.; Kane, M.; Anderson, S. L., Thermal and Adsorbate Effects on the Activity and Morphology of Size-selected Pd<sub>n</sub>/TiO<sub>2</sub> Model Catalysts. *Surf. Sci.* **2014**, *621* (0), 40-50. DOI:10.1016/j.susc.2013.11.002

43. Zhai, H.; Alexandrova, A. N., Ensemble-Average Representation of Pt Clusters in Conditions of Catalysis Accessed through GPU Accelerated Deep Neural Network Fitting Global Optimization. *J. Chem. Theory Comput.* **2016**, *12* (12), 6213-6226.

DOI:10.1021/acs.jctc.6b00994

44. Zhai, H.; Alexandrova, A. N., Local Fluxionality of Surface-Deposited Cluster Catalysts: the Case of Pt<sub>7</sub> on Al<sub>2</sub>O<sub>3</sub> *J. Phys. Chem. Lett.* **2018**, *9*, 1696-1702.

DOI:10.1021/acs.jpcclett.8b00379

45. Zhai, H.; Alexandrova, A. N., Fluxionality of Catalytic Clusters: When It Matters and How to Address It. *ACS Catal.* **2017**, *7* (3), 1905-1911. DOI:10.1021/acscatal.6b03243

46. Zhai, H.; Alexandrova, A. N., Correction to “Local Fluxionality of Surface-Deposited Cluster Catalysts: The Case of Pt<sub>7</sub> on Al<sub>2</sub>O<sub>3</sub>”. *J. Phys. Chem. Lett.* **2018**, *9* (20), 6011-6011.

DOI:10.1021/acs.jpcclett.8b03007

47. Zandkarimi, B.; Alexandrova, A. N., Surface-supported Cluster Catalysis: Ensembles of Metastable States Run the Show. *Wiley Interdiscip.* **2019**, *9*, e1420. DOI:10.1002/wcms.1420

48. Hatzikos, G. H.; Masel, R. I., Structure Sensitivity of Ethylene Adsorption on Pt(100): Evidence for Vinylidene Formation on (1×1) Pt(100). *Surf. Sci.* **1987**, *185* (3), 479-494.  
DOI:10.1016/S0039-6028(87)80172-3
49. Steininger, H.; Ibach, H.; Lehwald, S., Surface Reactions of Ethylene and Oxygen on Pt(111). *Surf. Sci.* **1982**, *117* (1), 685-698. DOI:/10.1016/0039-6028(82)90549-0
50. Yagasaki, E.; Backman, A. L.; Masel, R. I., The Adsorption and Decomposition of Ethylene on Pt(210), (1 · 1)Pt(110) and (2 · 1)Pt(110). *Vacuum* **1990**, *41* (1), 57-59.  
DOI:10.1016/0042-207X(90)90270-9
51. Janssens, T. V. W.; Zaera, F., The Role of Hydrogen-deuterium Exchange Reactions in the Conversion of Ethylene to Ethylidyne on Pt(111). *Surf. Sci.* **1995**, *344* (1), 77-84.  
DOI:10.1016/0039-6028(95)00836-5
52. Neurock, M.; van Santen, R. A., A First Principles Analysis of C–H Bond Formation in Ethylene Hydrogenation. *J. Phys. Chem. B.* **2000**, *104* (47), 11127-11145.  
DOI:10.1021/jp994082t
53. Anderson, A. B.; Choe, S., Ethylene Hydrogenation Mechanism on the Platinum (111) Surface: Theoretical Determination. *J. Phys. Chem.* **1989**, *93* (16), 6145-6149.  
DOI:10.1021/j100353a039
54. Shaikhutdinov, S. K.; Frank, M.; Bäumer, M.; Jackson, S. D.; Oldman, R. J.; Hemminger, J. C.; Freund, H. J., Effect of Carbon Deposits on Reactivity of Supported Pd Model Catalysts. *Catal. Lett.* **2002**, *80* (3), 115-122. DOI:10.1023/A:1015452207779

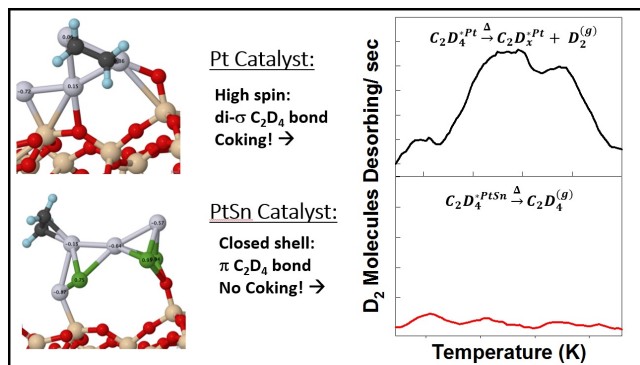
55. Mohsin, S. B.; Trenary, M.; Robota, H. J., Infrared Identification of the Low-temperature Forms of Ethylene Adsorbed on Platinum/alumina. *J. Phys. Chem.* **1988**, *92* (18), 5229-5233. DOI:10.1021/j100329a032
56. Pasteur, A. T.; Dixon-Warren, S. J.; King, D. A., Hydrogen Dissociation on Pt{100}: Nonlinear Power Law in Hydrogen Induced Restructuring. *J. Chem. Phys.* **1995**, *103* (6), 2251-2260. DOI:10.1063/1.469701
57. Anres, P.; Gaune-Escard, M.; Bros, J.; Hayer, E., Enthalpy of Formation of the (Pt-Sn) System. *J. Alloys Compd.* **1998**, *280* (1-2), 158-167.
58. Liu, H.; Ascencio, J. A. In *Structural stability and thermal transformation of Pt-Sn bimetallic nano clusters*, Journal of Nano Research, Trans Tech Publ: 2010; pp 131-138.
59. Jimenez-Izal, E.; Liu, J.-Y.; Alexandrova, A., *Germanium as key dopant to boost the catalytic performance of small platinum clusters for alkane dehydrogenation*. 2019; Vol. 374, p 93-100.
60. Jimenez-Izal, E.; Zhai, H.; Alexandrova, A. N., Nanoalloying MgO-Deposited Pt Clusters with Si for Controlling the Selectivity of Alkane Dehydrogenation. *ACS Catal.* **2018**, *8*, 8346-8356. DOI:10.1021/acscatal.8b02443
61. Gorey, T. J.; Dai, Y.; Anderson, S. L.; Lee, S.; Lee, S.; Seifert, S.; Winans, R. E., Selective growth of Al<sub>2</sub>O<sub>3</sub> on Size-selected Platinum Clusters by Atomic Layer Deposition. *Surf. Sci.* **2020**, *691*, 121485. DOI:10.1016/j.susc.2019.121485

62. Lee, S.; Fan, C.; Wu, T.; Anderson, S. L., CO Oxidation on Au<sub>n</sub>/TiO<sub>2</sub> Catalysts Produced by Size-Selected Cluster Deposition. *J. Am. Chem. Soc.* **2004**, *126* (18), 5682-5683.  
DOI:10.1021/ja049436v
63. Yeh, J. J.; Lindau, I., Atomic Subshell Photoionization Cross Sections and Asymmetry Parameters:  $1 < Z < 103$ . *Atomic Data and Nuclear Data Tables* **1985**, *32*, 1-155.
64. Powell, C. J.; Jablonski, A., *NIST Electron Effective-Attenuation-Length Database v. 1.3*, SRD 82. 1.1 ed.; NIST: Gaithersburg, MD, 2011.
65. Wu, T.; Kaden, W. E.; Kunkel, W. A.; Anderson, S. L., Size-dependent Oxidation of Pd<sub>n</sub> ( $n \leq 13$ ) on Alumina/NiAl(110): Correlation with Pd Core Level Binding Energies. *Surf. Sci.* **2009**, *603* (17), 2764-2770. DOI:10.1016/j.susc.2009.07.014
66. Kresse, G.; Furthmüller, J., Efficiency of ab-initio Total Energy Calculations for Metals and Semiconductors using a Plane-wave Basis Set. *Comput. Mater. Sci.* **1996**, *6*, 15-50.  
DOI:10.1016/0927-0256(96)00008-0
67. Kresse, G.; Furthmüller, J., Efficient Iterative Schemes for ab initio Total-energy Calculations using a Plane-wave Basis Set. *Phys. Rev. B* **1996**, *54*, 11169.  
DOI:10.1103/PhysRevB.54.11169
68. Kresse, G.; Hafner, J., Ab initio Molecular Dynamics for Liquid Metals. *Phys. Rev. B* **1993**, *47*, 558. DOI:10.1103/physrevb.47.558

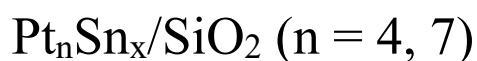
69. Kresse, G.; Hafner, J., Ab initio Molecular-dynamics Simulation of the Liquid-metal-amorphous-semiconductor Transition in Germanium. *Phys. Rev. B* **1994**, *49*, 14251.  
DOI:10.1103/PhysRevB.49.14251
70. Kresse, G.; Joubert, D., From Ultrasoft Pseudopotentials to the Projector Augmented-wave Method. *Phys. Rev. B.* **1999**, *59* (3), 1758-1775. DOI:10.1103/PhysRevB.59.1758
71. Perdew, J. P.; Burke, K.; Ernzerhof, M., Generalized Gradient Approximation Made Simple. *Phys. Rev. Lett.* **1996**, *77*, 3865. DOI:10.1103/PhysRevLett.77.3865
72. Ugliengo, P.; Sodupe, M.; Musso, F.; Bush, I. J.; Orlando, R.; Dovesi, R., Realistic Models of Hydroxylated Amorphous Silica Surfaces and MCM-41 Mesoporous Material Simulated by Large-scale Periodic B3LYP Calculations. *Adv. Mater.* **2008**, *20* (23), 4579-4583.  
DOI:10.1002/adma.200801489
73. Becke, A. D., Density-functional Thermochemistry. III. The Role of Exact Exchange. *J. Chem. Phys.* **1993**, *98* (7), 5648-5652. DOI:10.1063/1.464913
74. Lee, C.; Yang, W.; Parr, R. G., Development of the Colle-Salvetti Correlation-energy Formula into a Functional of the Electron Density. *Phys. Rev. B.* **1988**, *37* (2), 785-789.  
DOI:10.1103/PhysRevB.37.785
75. Vosko, S. H.; Wilk, L.; Nusair, M., Accurate spin-dependent Electron Liquid Correlation Energies for Local Spin Density Calculations: a Critical Analysis. *Can. J. Phys.* **1980**, *58* (8), 1200-1211. DOI:10.1139/p80-159

76. Stephens, P. J.; Devlin, F. J.; Chabalowski, C. F.; Frisch, M. J., Ab Initio Calculation of Vibrational Absorption and Circular Dichroism Spectra Using Density Functional Force Fields. *J. Phys. chem.* **1994**, *98* (45), 11623-11627. DOI:10.1021/j100096a001
77. Tang, W.; Sanville, E.; Henkelman, G., A Grid-based Bader Analysis Algorithm without Lattice Bias. *J. Condens. Matter. Phys.* **2009**, *21* (8), 084204. DOI:10.1088/0953-8984/21/8/084204
78. Sanville, E.; Kenny, S. D.; Smith, R.; Henkelman, G., Improved Grid-based Algorithm for Bader Charge Allocation. *J. Comput. Chem.* **2007**, *28* (5), 899-908. DOI:10.1002/jcc.20575
79. Henkelman, G.; Arnaldsson, A.; Jónsson, H., A Fast and Robust Algorithm for Bader Decomposition of Charge Density. *Comput. Mater.* **2006**, *36* (3), 354-360. DOI:10.1016/j.commatsci.2005.04.010
80. Yu, M.; Trinkle, D. R., Accurate and Efficient Algorithm for Bader Charge Integration. *J. Chem. Phys.* **2011**, *134* (6), 064111. DOI:10.1063/1.3553716
81. Henkelman, G.; Uberuaga, B. P.; Jónsson, H., A Climbing Image Nudged Elastic Band Method for Finding Saddle Points and Minimum Energy Paths. *J. Chem. Phys.* **2000**, *113* (22), 9901-9904. DOI:10.1063/1.1329672
82. Vineyard, G. H., Frequency Factors and Isotope Effects in Solid State Rate Processes. *J. Phys. Chem. Solids* **1957**, *3* (1), 121-127. DOI:10.1016/0022-3697(57)90059-8
83. Evans, D. J.; Holian, B. L., The Nose–Hoover Thermostat. *J. Chem. Phys.* **1985**, *83* (8), 4069-4074. DOI:10.1063/1.449071

## TOC GRAPHIC



# Coking-Resistant Sub-Nano Dehydrogenation Catalysts:



*Timothy J. Gorey,<sup>a†</sup> Borna Zandkarimi,<sup>b†</sup> Guangjing Li,<sup>a</sup> Eric T. Baxter,<sup>a</sup>*

*Anastassia N. Alexandrova,<sup>b,c\*</sup> and Scott L. Anderson<sup>a\*</sup>*

<sup>a</sup>Chemistry Department, University of Utah, 315 S. 1400 E., Salt Lake City, UT 84112

<sup>b</sup>Chemistry and Biochemistry, University of California, Los Angeles, and <sup>c</sup>California NanoSystems Institute, Los Angeles, CA 90095

## Supporting information

<sup>†</sup> These authors contributed equally to this work.

<sup>\*</sup>Senior Authors

Corresponding Authors: Scott Anderson, (801) 585-7289, [anderson@utah.edu](mailto:anderson@utah.edu), Anastassia Alexandrova, (310) 825-3769, [ana@chem.ucla.edu](mailto:ana@chem.ucla.edu)





**Fig. S1** shows four sequential  $C_2D_4$  TPD runs from  $Pt_4/SiO_2$  (top) and  $Pt_7/SiO_2$  (bottom). As discussed in the main text and shown in **Table 1**, the overall number of available  $C_2D_4$  decreased incrementally with each cycle. Similarly, the amount of liberated  $D_2$  incrementally decreases.  $C_2D_4$  desorption from clean  $SiO_2$  is also shown for each cluster size. There are two distinguishable features for  $Pt_4$ , and less so for  $Pt_7$ .  $C_2D_4$  desorption begins at the onset of the heat ramp (180 K), peaking around 260 K, and decreasing to baseline by  $\sim 500$  K. Incremental loss in the number of desorbed  $C_2D_4$ (intact) and  $D_2$  molecules is consistent with coke deposition.

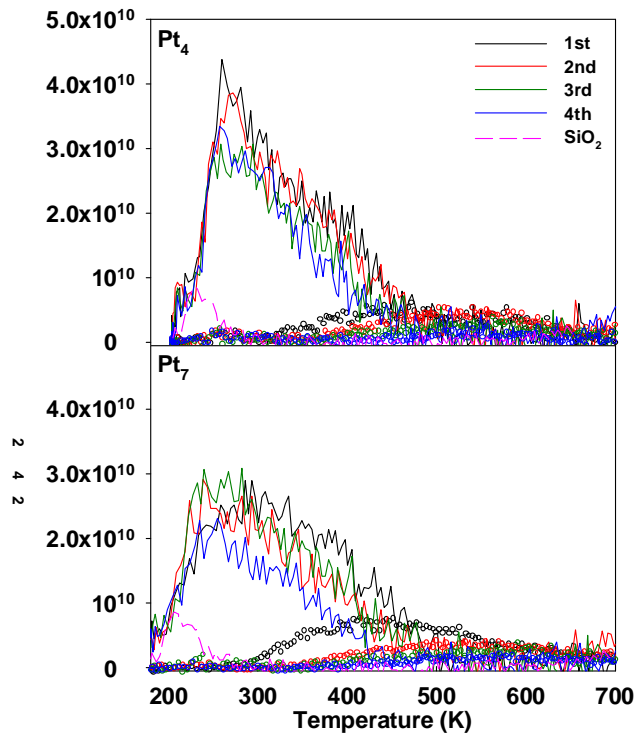


**Figure S1.** Four sequential  $C_2D_4$  TPD from  $Pt_4/SiO_2$ . Intact  $C_2D_4$  is shown as solid lines, and  $D_2$  desorption is shown at hollow symbols. Intact  $C_2D_4$  desorption from clean  $SiO_2$  is also shown in each panel as a dashed pink line.

As was done for **Fig. S1**, four sequential  $C_2D_4$  TPDs were carried out on the  $Pt_4Sn_{3.3}/SiO_2$  catalyst. Numbers of  $C_2D_4$  molecules *per* Pt atom are shown in **Table 2** of the manuscript.

Results are plotted in **Fig. S2** along with  $C_2D_4$  desorption from a cluster-free  $SiO_2$  surface that has been exposed to a  $H_2/SnCl_4/H_2$  treatment.

All four spectra are shown for  $Pt_4Sn_{3.3}/SiO_2$  and  $Pt_7Sn_{6.3}/SiO_2$ , with the  $D_2$  desorption plotted separately on inset plots.

Note the anomalous behavior of the first ethylene TPD (red) in **Fig. S2**. This is attributed to the surface being covered with residual H and Cl atoms as a result of the Sn deposition process. The removal of these adsorbates has been described in detail previously, and the mass 36 (HCl) desorption during the first  $C_2D_4$  TPD is shown in **Fig. S3** for both cluster sizes.

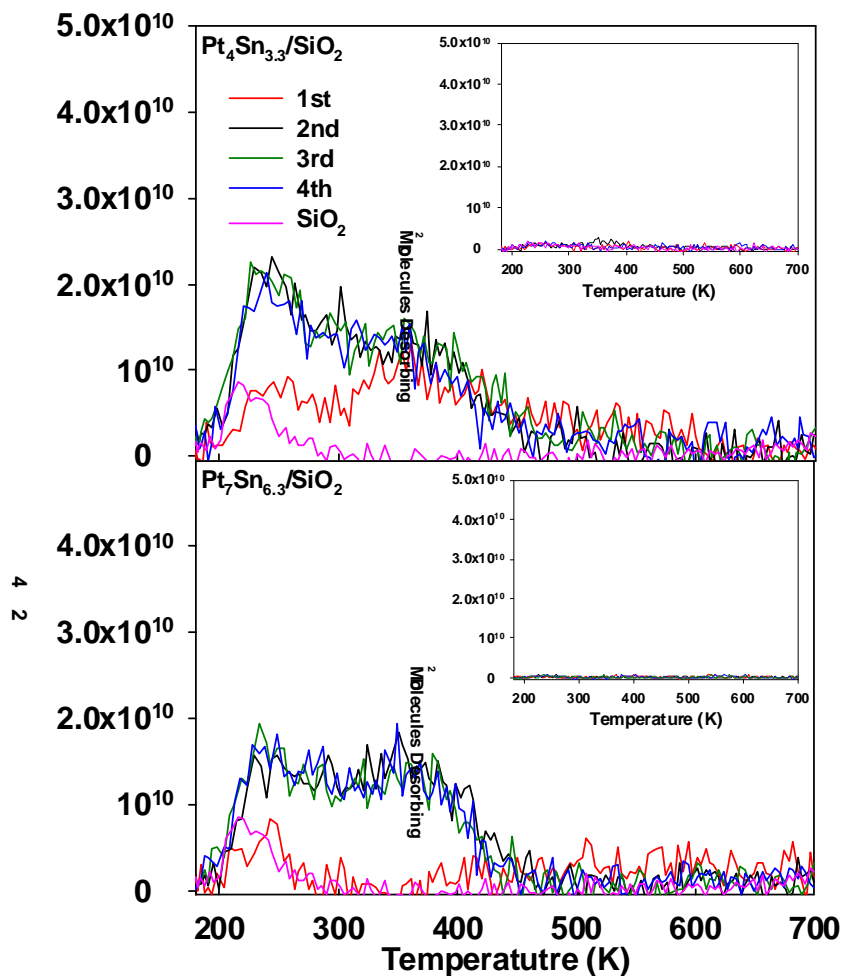


**Figure S2.** Four sequential desorption spectra of  $C_2D_4$  (solid lines) and  $D_2$  (inset plots) from the first (red) and fourth (blue)  $C_2D_4$  TPD. Each spectra was collected after a 10 L dose of  $C_2D_4$  to  $Pt_nSn_x/SiO_2$  ( $n = 4, 7$ ).  $C_2D_4$  desorption from bare  $SiO_2$  treated with 1 ALD cycle is also plotted (pink line), no  $D_2$  is observed.

Using a method described previously<sup>1-2</sup>, the C<sub>2</sub>D<sub>4</sub> thermal desorption spectra can be fit to extract desorption energy distributions by using the first order rate equation:

$$I(t) \propto \frac{-d\theta}{dt} = (\theta(E_{des}) \cdot \nu) e^{-\frac{E_{des}}{kT(t)}}$$

with I(t) being the time-dependent

C<sub>2</sub>D<sub>4</sub> desorption signal, E<sub>des</sub> the desorption energy, ν the exponential pre-factor, T(t) is the heat ramp, and θ(E<sub>des</sub>) is the distribution of occupied binding site energies. For all experiments here, a nominal heat ramp rate of 3 K/s was used, but temperature versus time data is always collected during TPD acquisition in order to account for fluctuations in the heating ramp rate, though no corrections were needed. For the fit, a simulated θ(E<sub>des</sub>) is calculated for each contributing peak and plotted to match the experimentally measured I(t). The greatest source of uncertainty here is the pre-exponential factor, ν. It is not practicable to carry out the series of studies that would be required to estimate ν from the TPD data, and we simply assumed a value of 10<sup>14</sup> s<sup>-1</sup>, which is in the range of values often used for CO TPD.<sup>3-7</sup> In previous studies<sup>2</sup>, the effect of varying ν between 10<sup>13</sup> s<sup>-1</sup> to 10<sup>15</sup> s<sup>-1</sup> was tested, and found to shift the θ(E<sub>des</sub>) distribution by only ~7%.

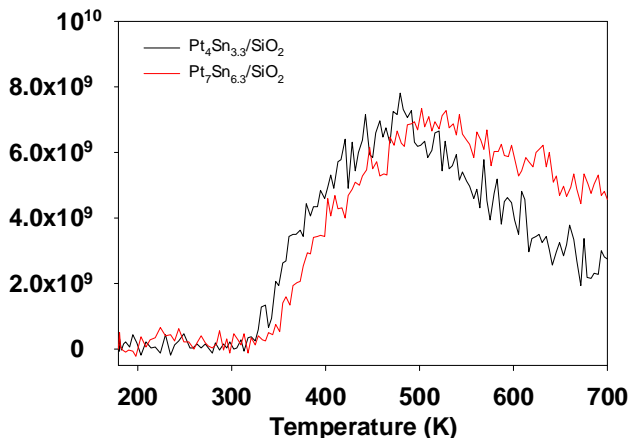


**Figure S3.** Mass 36 desorption (HCl) during the first C<sub>2</sub>D<sub>4</sub> TPD for Pt<sub>n</sub>Sn<sub>x</sub>/SiO<sub>2</sub>. No HCl is detected in subsequent runs.

## XPS Characterization of Carbon Deposition.

Because the C 1s photoemission cross section is quite small,<sup>8</sup> and carbon is deposited only on the clusters, it was difficult to quantify carbon deposition for samples of the sort discussed above. To increase the carbon coverage, we prepared Pt<sub>4</sub>/SiO<sub>2</sub> and Pt<sub>4</sub>Sn<sub>3.3</sub>/SiO<sub>2</sub> samples with twice the usual cluster coverage, and subjected them to eight sequential C<sub>2</sub>D<sub>4</sub> TPD/R runs. The results are compared in **Fig. S4**. A broad C 1s peak is observed for the blank SiO<sub>2</sub> substrate, attributed to adventitious carbon remaining after the substrate was cleaned by annealing in O<sub>2</sub>. The binding energy is in the range expected for partially oxidized carbon, as might be expected after annealing in O<sub>2</sub>.

For Pt<sub>4</sub>/SiO<sub>2</sub> after C<sub>2</sub>D<sub>4</sub> TPD/R, this adventitious carbon feature is still present, as expected, but a sharper C 1s feature appears at lower binding energy, which we attribute to carbon deposited on the Pt clusters by C<sub>2</sub>D<sub>4</sub> dehydrogenation. Subtracting the contribution from adventitious carbon, the intensity of this low binding energy feature corresponds to eight TPD/R runs having deposited ~1.5 C atom/Pt atom.

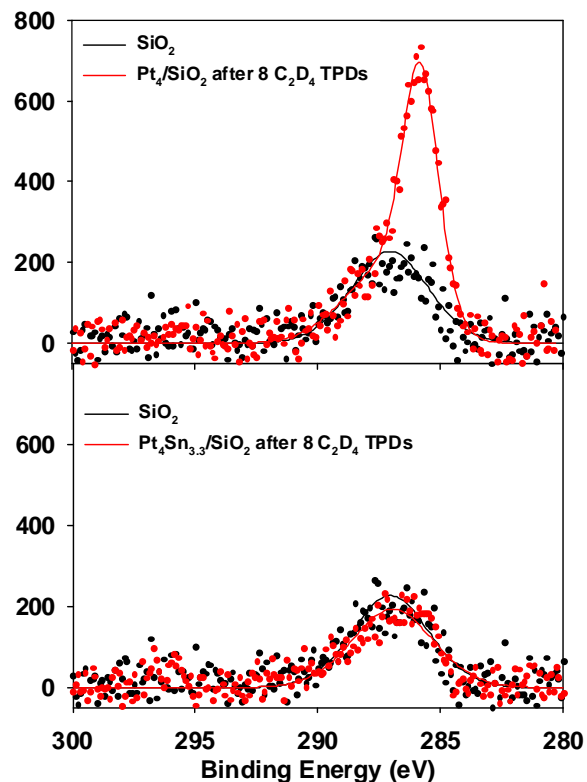


**Figure S4.** Comparison of C 1s XP spectra for an SiO<sub>2</sub> substrate, a Pt<sub>4</sub>/SiO<sub>2</sub> sample, and a Pt<sub>4</sub>Sn<sub>3.3</sub>/SiO<sub>2</sub> sample, subjected to eight sequential C<sub>2</sub>D<sub>4</sub> TPD/R runs.

The lower frame of the figure shows analogous data for Pt<sub>4</sub>Sn<sub>3.3</sub>/SiO<sub>2</sub> after eight C<sub>2</sub>D<sub>4</sub> TPD runs. No increase in carbon intensity was observed, compared to the SiO<sub>2</sub> substrate, consistent with the TPD/R results showing no significant D<sub>2</sub> desorption from the Sn-alloyed clusters.

**Fig. S5** shows the fit for TPD spectra. Here, we use the first C<sub>2</sub>D<sub>4</sub> TPD run from Pt<sub>4</sub>/SiO<sub>2</sub> as a representative example; this method was carried out for all energy desorption profile plots in this paper. Fits were performed using a two component model, representing low temperature and high temperature feature. Using these fits, the desorption profile was computed and plotted as a function

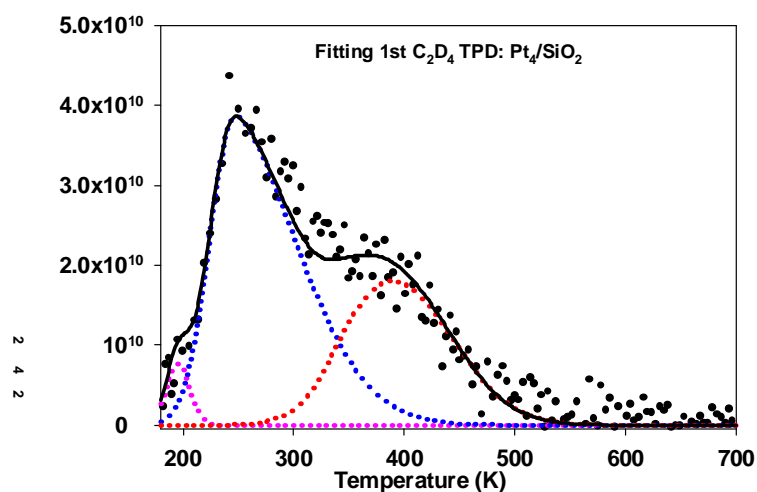


**Figure S5.** 1<sup>st</sup> C<sub>2</sub>D<sub>4</sub> TPD from Pt<sub>4</sub>/SiO<sub>2</sub>. The spectrum was fit with low(blue) and high(red) temperature components. The fits can be used to calculate energy desorption profiles.

of binding energy. This model makes the critical assumption of first order desorption kinetics. While we expect some 2<sup>nd</sup> order behavior for surface-bound C<sub>2</sub>D<sub>4</sub>, i.e., dissociative adsorption → recombinative desorption, the first order fit was carried out simply to approximate the binding energies for comparison to DFT studies.

Desorption energy distributions for  $\text{Pt}_7/\text{SiO}_2$  and  $\text{Pt}_7\text{Sn}_{6.3}/\text{SiO}_2$  were calculated as described above. Briefly, the first  $\text{C}_2\text{D}_4$  TPD from  $\text{Pt}_7/\text{SiO}_2$  was fit with a low and high temperature component and then modeled using a first order kinetics relation. The same was done for the *second*  $\text{C}_2\text{D}_4$  for the  $\text{Pt}_7\text{Sn}_{6.3}/\text{SiO}_2$  sample.

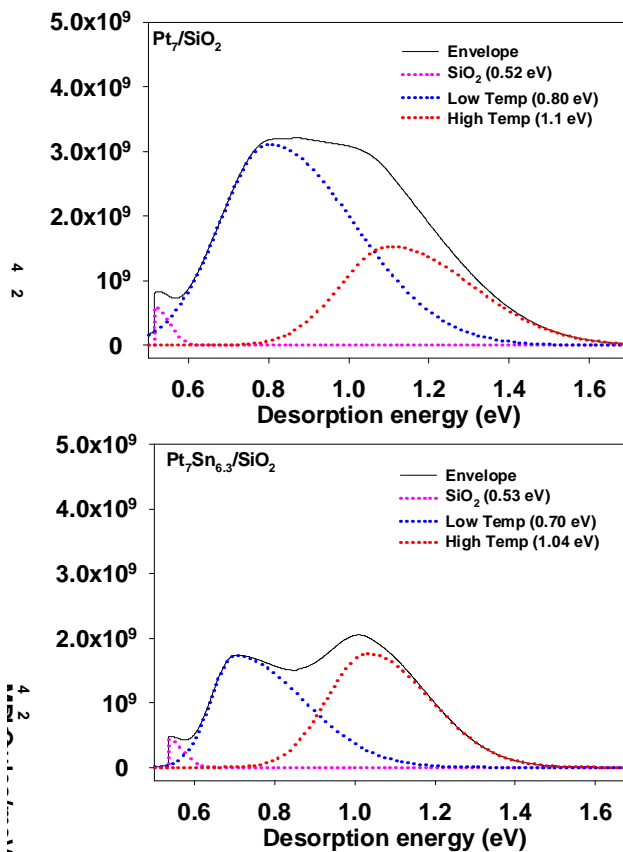


**Figure S6.** Arrhenius fits for the  $\text{C}_2\text{D}_4$  TPD from  $\text{Pt}_7/\text{SiO}_2$  and  $\text{Pt}_7\text{Sn}_{6.3}/\text{SiO}_2$  spectra in **Fig. 1**.

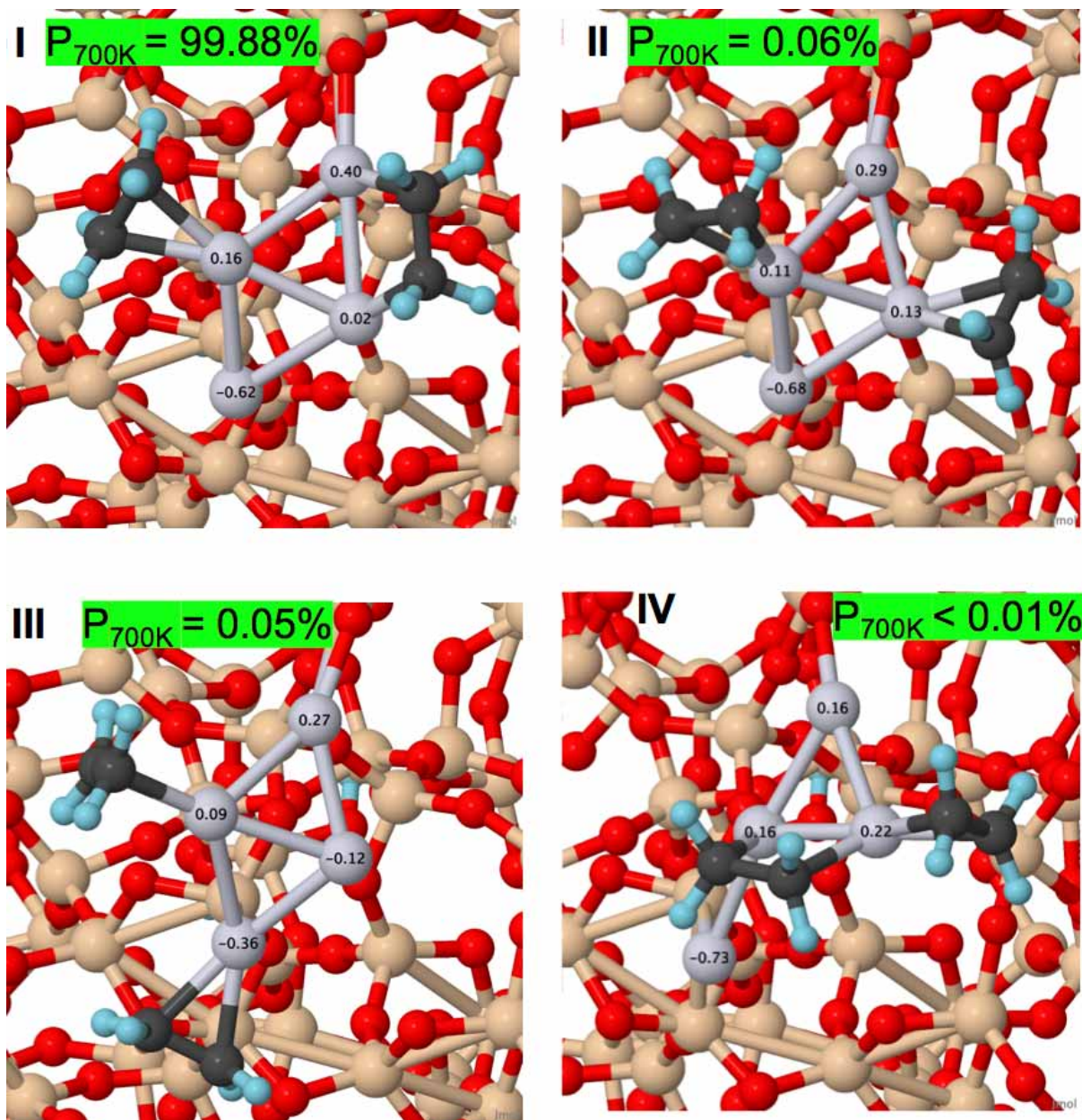


**Figure S7.** Thermally-accessible geometries of  $(C_2H_4)_2/Pt_4/SiO_2$  obtained from global optimization calculations along with their Boltzmann populations at 700 K.



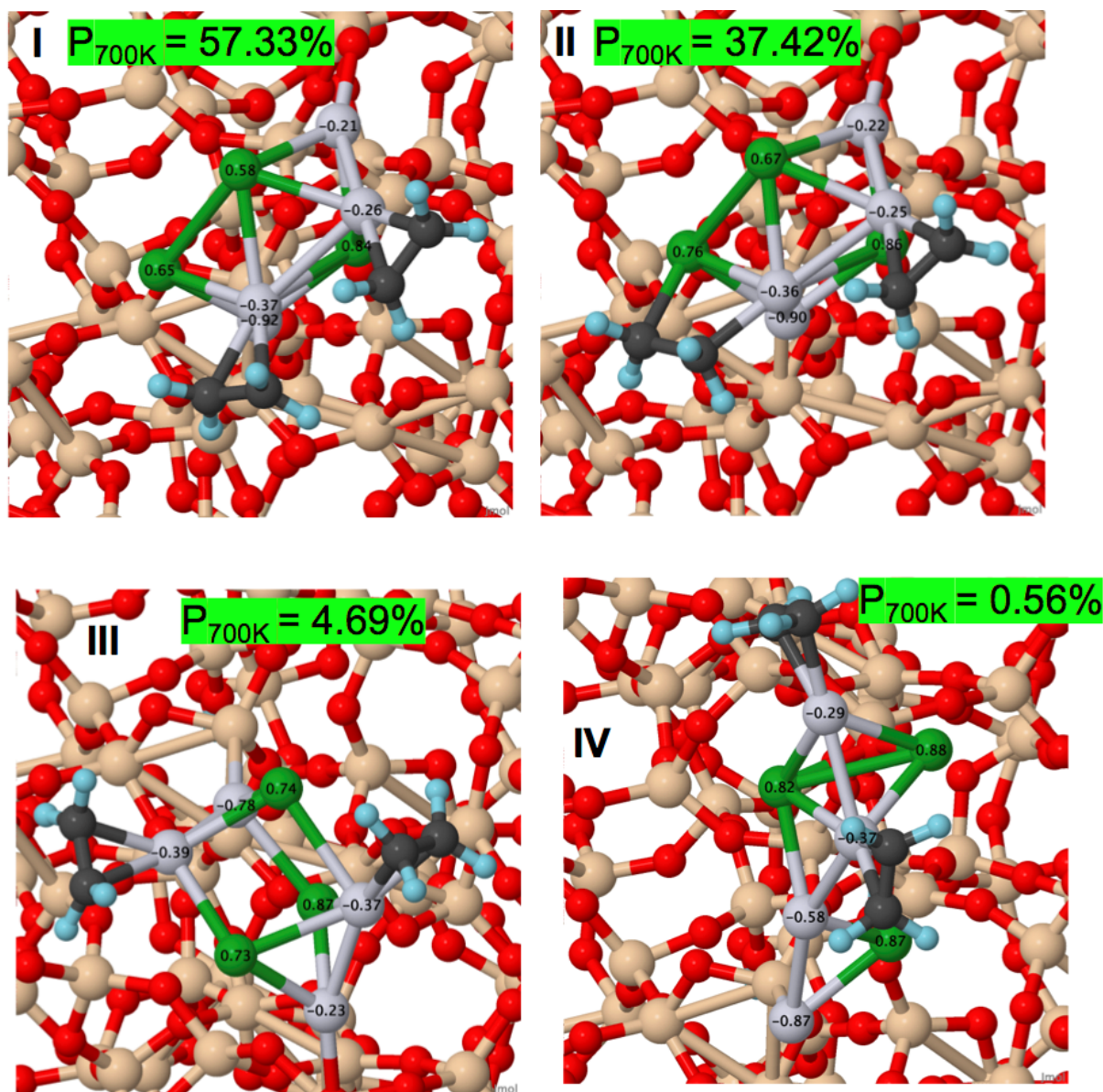


**Figure S8.** Thermally-accessible geometries of  $(\text{C}_2\text{H}_4)_2/\text{Pt}_4\text{Sn}_3/\text{SiO}_2$  obtained from global optimization calculations along with their Boltzmann populations at 700 K. Note that the ensemble is dominated by  $\text{C}_2\text{H}_4$   $\pi$ -binding mode.

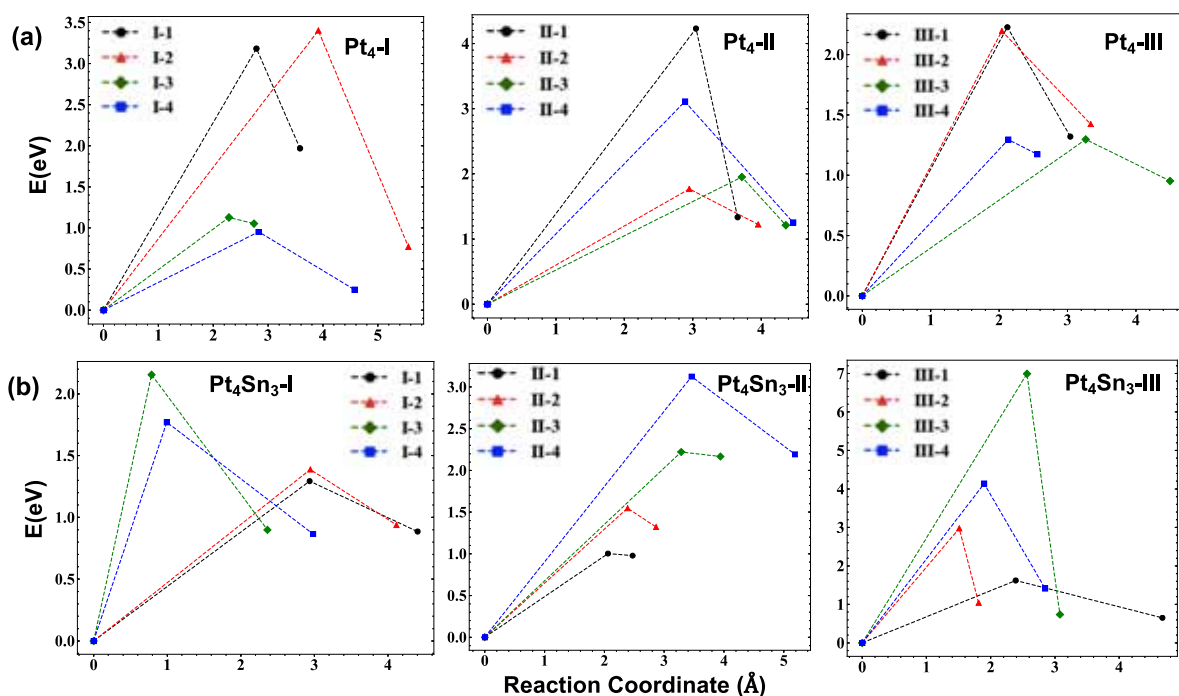


**Figure S9.** Reaction profiles of breaking C-H bond obtained from CI-NEB calculations for (a) C<sub>2</sub>H<sub>4</sub>/Pt<sub>4</sub>/SiO<sub>2</sub> and (b) C<sub>2</sub>H<sub>4</sub>/Pt<sub>4</sub>Sn<sub>3</sub>/SiO<sub>2</sub>. The reaction barrier corresponding to the highest populated C<sub>2</sub>H<sub>4</sub>/Pt<sub>4</sub>Sn<sub>3</sub>/SiO<sub>2</sub> isomer is 0.3 eV higher than that of C<sub>2</sub>H<sub>4</sub>/Pt<sub>4</sub>/SiO<sub>2</sub>. The reaction coordinate is defined as the root mean square distance from the reactant, which can be found in the computational methods section.

**Table S1.** All reaction barriers of C<sub>2</sub>H<sub>4</sub>/Pt<sub>4</sub>/SiO<sub>2</sub> and C<sub>2</sub>H<sub>4</sub>/Pt<sub>4</sub>Sn<sub>3</sub>/SiO<sub>2</sub> obtained from CI-NEB calculations along with their contribution to the final *k<sub>ens</sub>* at 700 K.

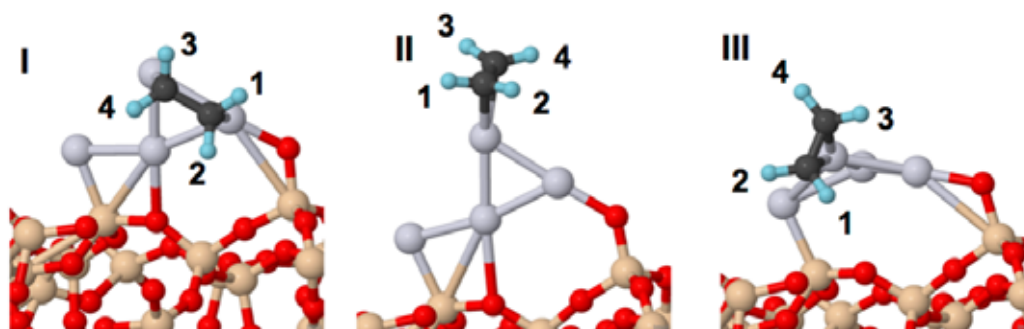
C <sub>2</sub> H <sub>4</sub> /Pt <sub>4</sub> /SiO <sub>2</sub>	Barrier (eV)				P <sub>700K</sub>
	Path-1	Path-2	Path-3	Path-4	
I	0.95	1.13	3.18	3.40	76.71%
II	1.77	1.95	3.11	4.23	23.02%
III	1.29	1.30	2.20	2.23	0.01%
C <sub>2</sub> H <sub>4</sub> /Pt <sub>4</sub> Sn <sub>3</sub> /SiO <sub>2</sub>					
I	1.29	1.39	1.77	2.15	69.03%
II	1.00	1.55	2.22	3.12	27.45%
III	1.62	2.97	4.14	6.99	6.70%

**Table S2.** Charge on the cluster, ethylene binding mode, and Boltzmann population at 700 K obtained for C<sub>2</sub>H<sub>4</sub>/Pt<sub>4</sub>/SiO<sub>2</sub>, (C<sub>2</sub>H<sub>4</sub>)<sub>2</sub>/Pt<sub>4</sub>/SiO<sub>2</sub>, C<sub>2</sub>H<sub>4</sub>/Pt<sub>4</sub>Sn<sub>3</sub>/SiO<sub>2</sub>, and (C<sub>2</sub>H<sub>4</sub>)<sub>2</sub>/Pt<sub>4</sub>Sn<sub>3</sub>/SiO<sub>2</sub>.

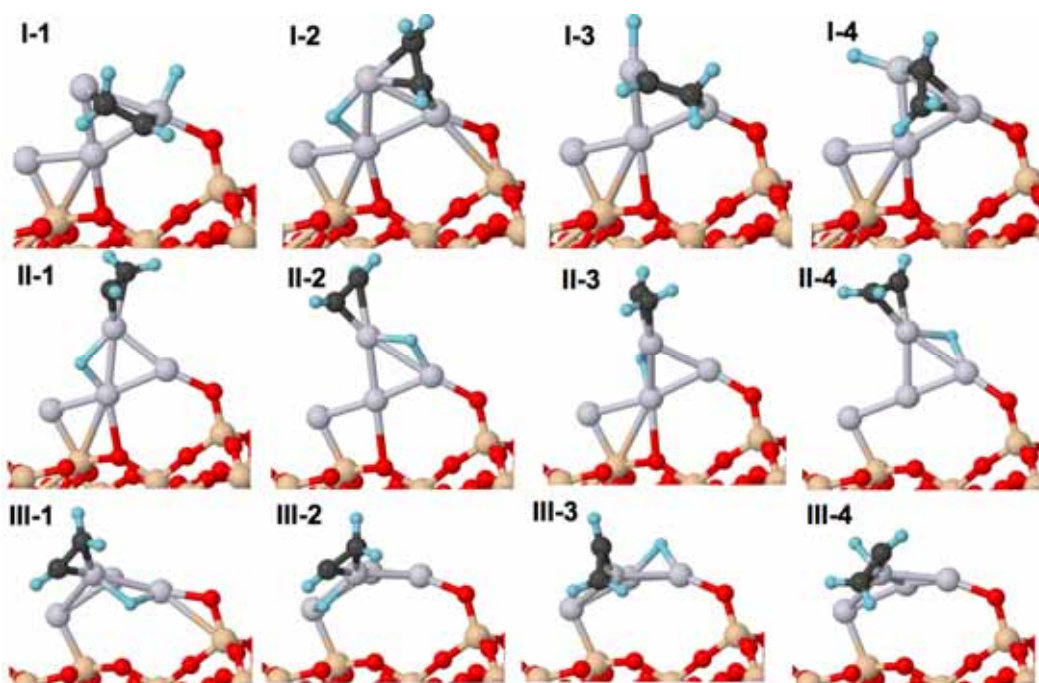
Isomer	Q <sub>cluster</sub> (e)		C <sub>2</sub> H <sub>4</sub> Binding mode		P <sub>700K</sub>	
	Pt <sub>4</sub>	Pt <sub>4</sub> Sn <sub>3</sub>	Pt <sub>4</sub>	Pt <sub>4</sub> Sn <sub>3</sub>	Pt <sub>4</sub>	Pt <sub>4</sub> Sn <sub>3</sub>
C <sub>2</sub> H <sub>4</sub> /Pt <sub>4</sub> Sn <sub>0,3</sub> /SiO <sub>2</sub>						
I	-0.15	0.39	di-σ	π	76.71%	69.03%
II	-0.11	0.46	π	π	23.01%	27.45%
III	-0.10	0.43	π	π	0.25%	2.32%
IV	-0.12	0.50	π	π	0.01%	0.7%
V	-0.12	0.50	di-σ	π	0.01%	0.3%
VI	-0.14	0.32	di-σ	π	<0.01%	0.2%
(C <sub>2</sub> H <sub>4</sub> ) <sub>2</sub> /Pt <sub>4</sub> Sn <sub>0,3</sub> /SiO <sub>2</sub>						
I	-0.04	0.31	π, di-σ	π, π	99.88%	57.33%
II	-0.16	0.56	π, π	π, di-σ	0.06%	37.42%
III	-0.11	0.58	π, π	π, π	0.05%	4.69%
IV	-0.19	0.45	π, di-σ	π, π	<0.01%	0.56%

**Table S3.** Ensemble averaged first and second C<sub>2</sub>H<sub>4</sub> binding energies on Pt<sub>4</sub>/SiO<sub>2</sub> and Pt<sub>4</sub>Sn<sub>3</sub>/SiO<sub>2</sub> calculated at 700 K.

Structure	E <sub>b1</sub> (eV)	E <sub>b2</sub> (eV)
Pt <sub>4</sub> /SiO <sub>2</sub>	-1.91	-1.76
Pt <sub>4</sub> Sn <sub>3</sub> /SiO <sub>2</sub>	-1.11	-1.04

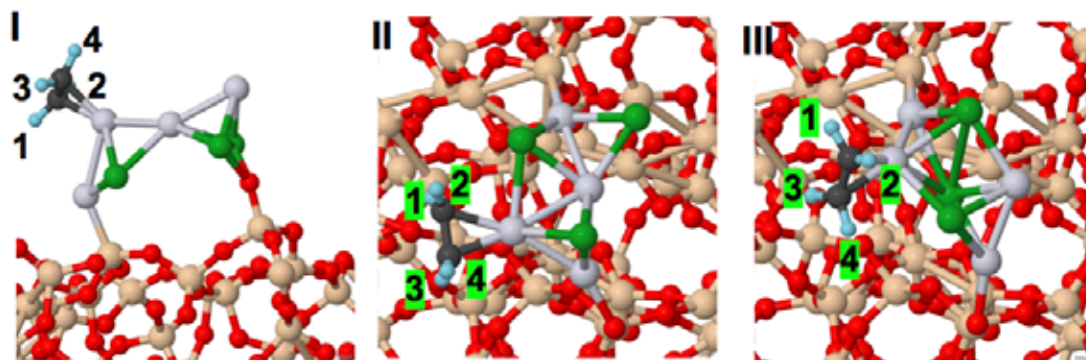


(a)

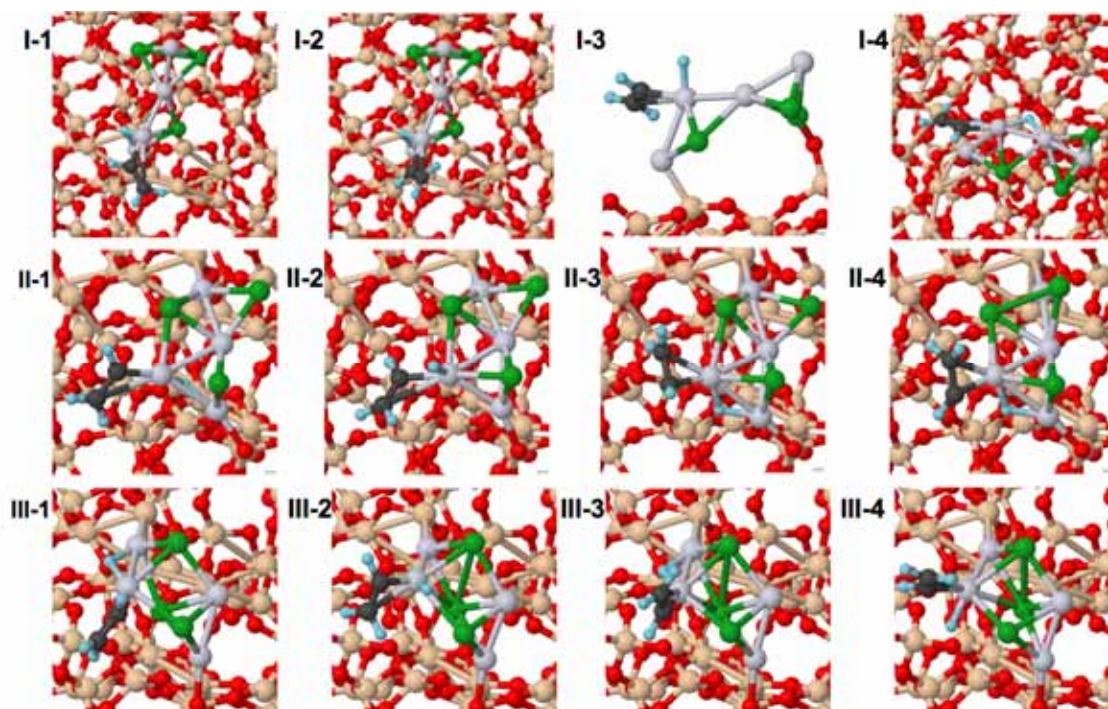


(b)

**Figure S10.** (a) 3 most populated  $C_2H_4/Pt_4/SiO_2$  isomers used in CI-NEB calculations and (b) all 12 products (4 for each structure) obtained by cleaving every C-H bond in  $C_2H_4$  on  $Pt_4/SiO_2$ .



(a)



(b)

**Figure S11.** (a) Three most populated  $C_2H_4/Pt_4Sn_3/SiO_2$  isomers used in CI-NEB calculations and (b) all 12 products (four for each structure) obtained by cleaving every C-H bond in  $C_2H_4$  on  $Pt_4Sn_3/SiO_2$ .

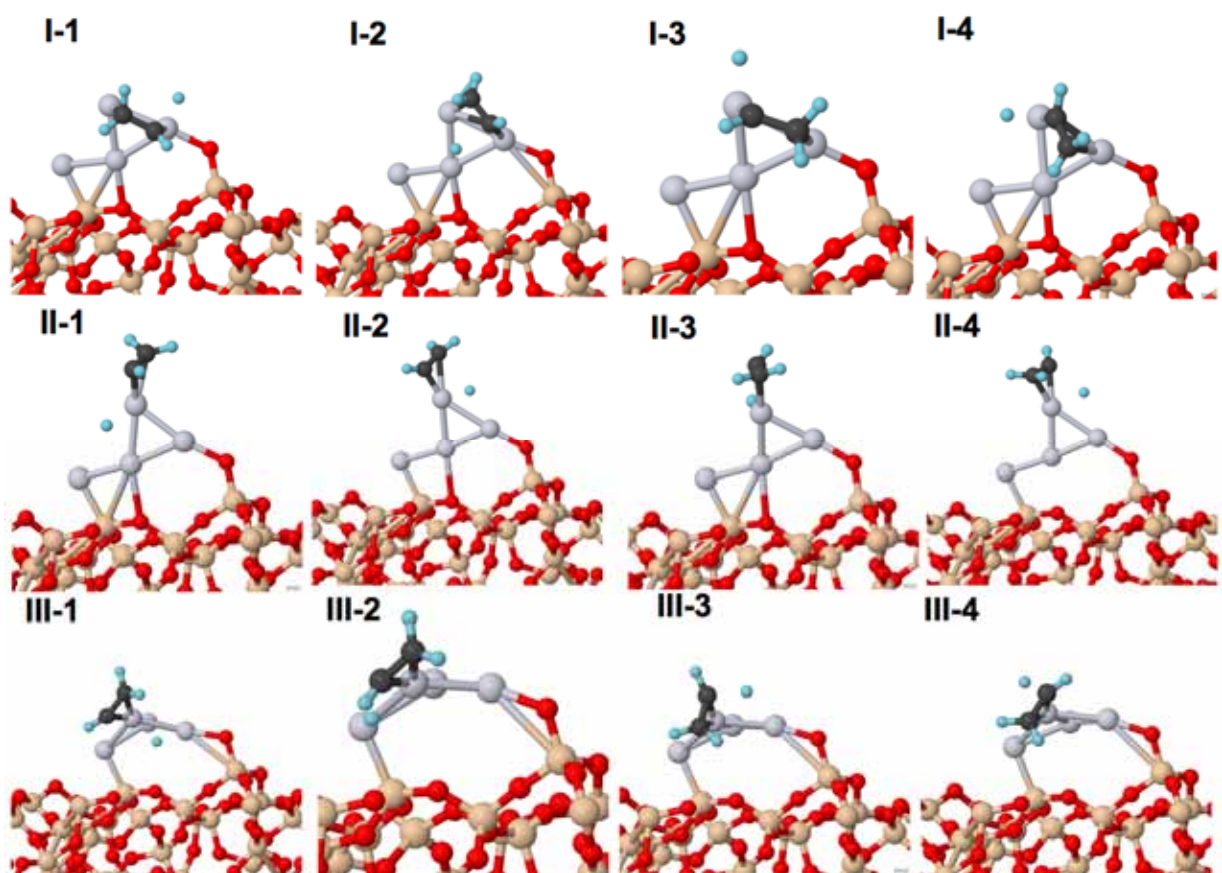


**Figure S12.** Transition state structures corresponding to all 12 different pathways of C-H bond dissociation on Pt<sub>4</sub>/SiO<sub>2</sub> obtained from CI-NEB calculations.

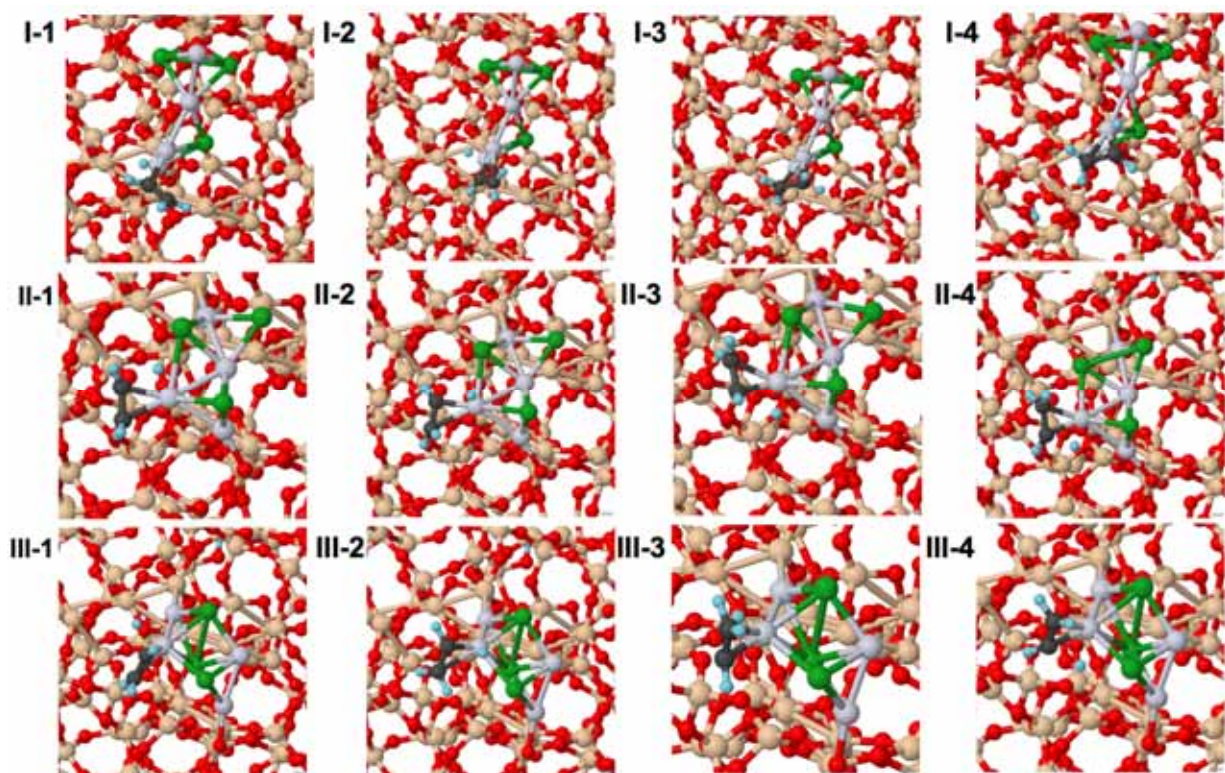


**Figure S13.** Transition state structures corresponding to all 12 different pathways of C-H bond dissociation on Pt<sub>4</sub>Sn<sub>3</sub>/SiO<sub>2</sub> obtained from CI-NEB calculations.

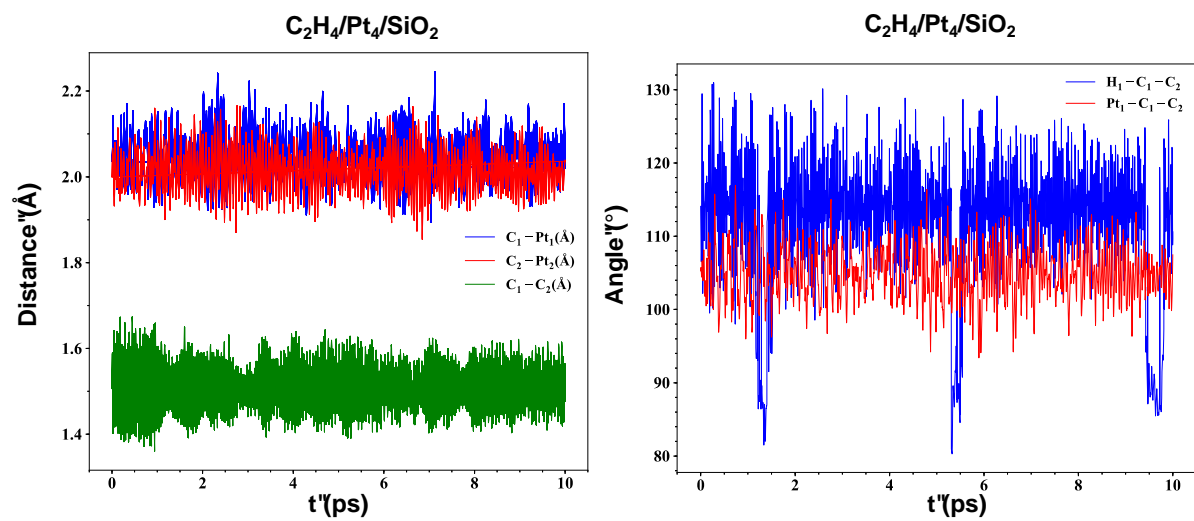


**Figure S14.** C-C and C-Pt Bond distance, and  $\angle HCC$  and  $\angle PtCC$  bond angle during the MD simulations of  $C_2H_4/Pt_4/SiO_2$ . The time step is 1 fs and the total run time is 10 ps.



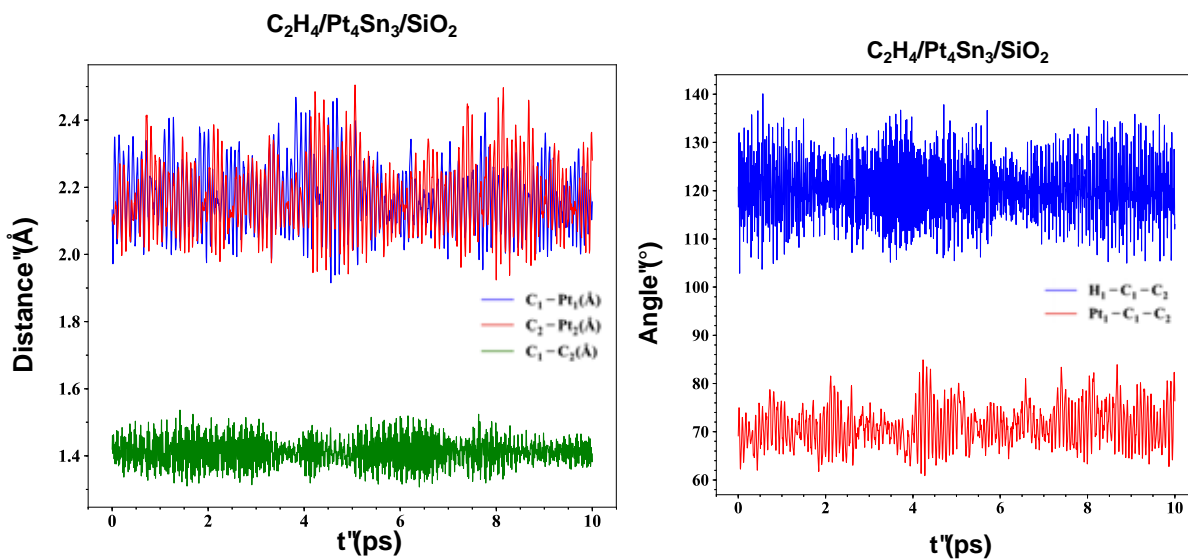


**Figure S15.** C-C and C-Pt Bond distance, and  $\angle HCC$  and  $\angle PtCC$  bond angle during the MD simulations of  $C_2H_4/Pt_4Sn_3/SiO_2$ . The time step is 1 fs and the total run time is 10 ps.

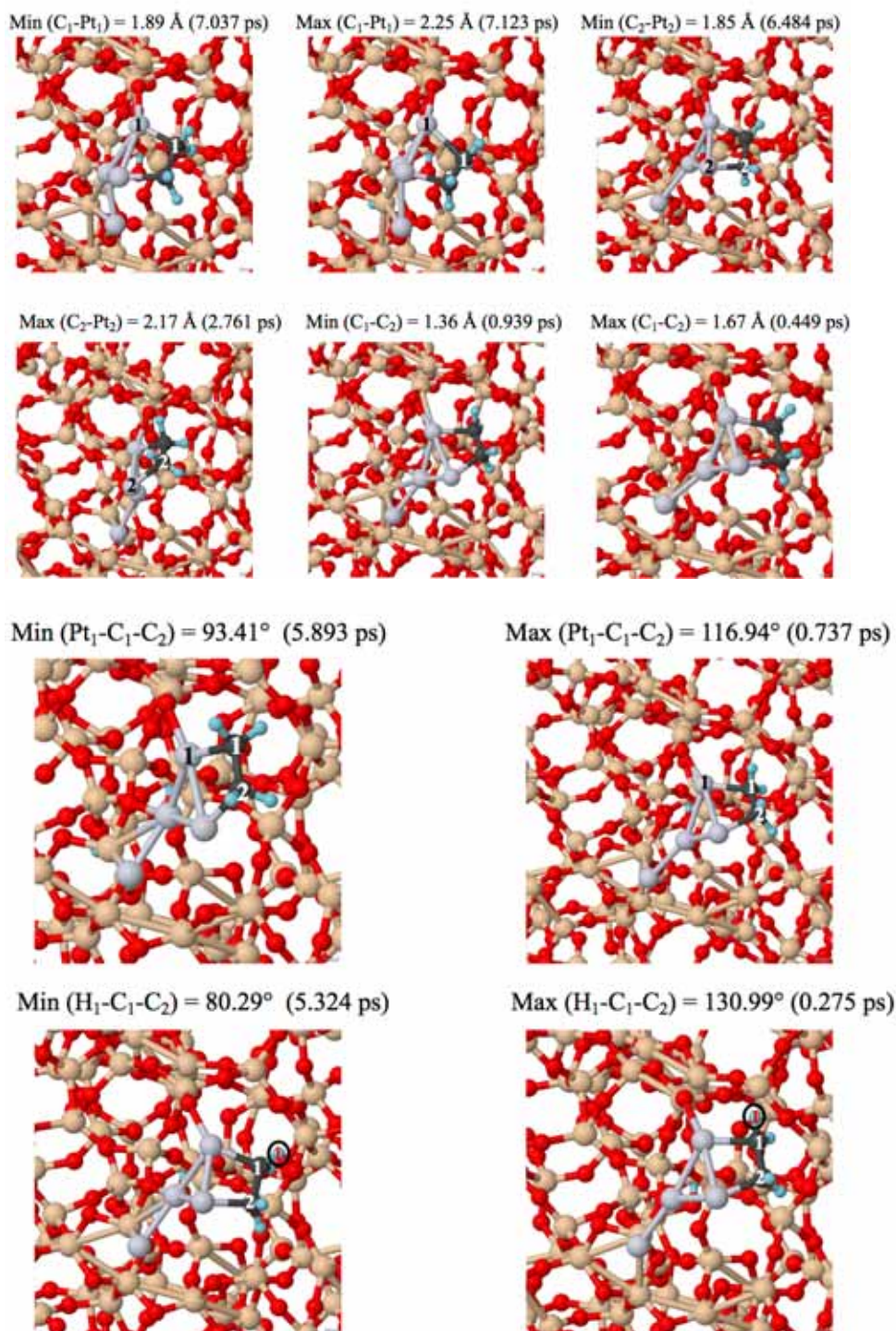


**Figure S16.** All structures corresponding to an extreme in bond distance or bond angle during the MD simulations of C<sub>2</sub>H<sub>4</sub>/Pt<sub>4</sub>/SiO<sub>2</sub> with their corresponding value.

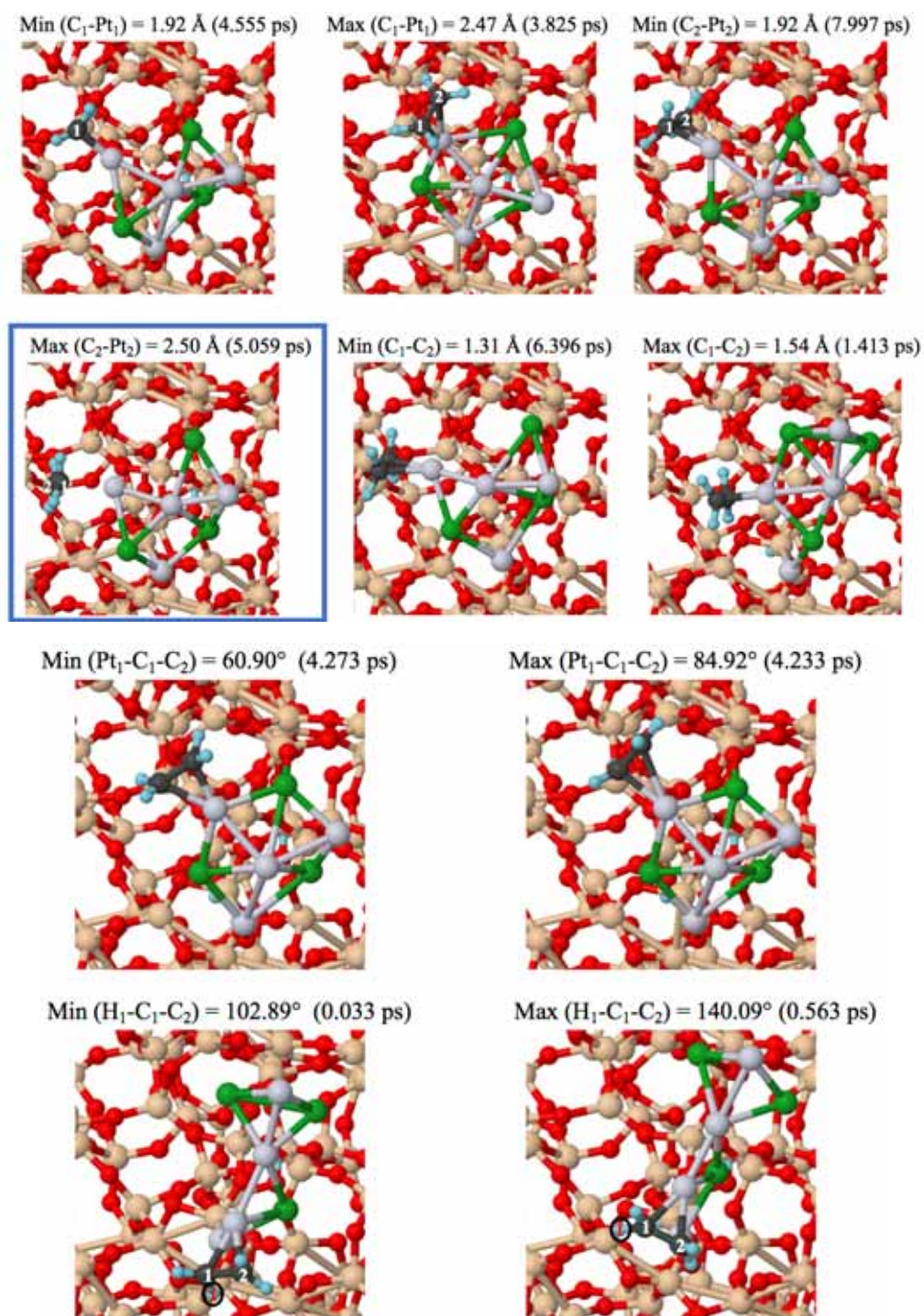


**Figure S17.** All structures corresponding to an extreme in bond distance or bond angle during the MD simulations of C<sub>2</sub>H<sub>4</sub>/Pt<sub>4</sub>Sn<sub>3</sub>/SiO<sub>2</sub> with their corresponding value. Note that at 5.059 ps C<sub>2</sub>H<sub>4</sub> is almost detached from the cluster.

## REFERENCES

1. Roberts, F. S.; Kane, M. D.; Baxter, E. T.; Anderson, S. L., Oxygen Activation and CO Oxidation over Size-selected Pt<sub>n</sub>/alumina/Re(0001) Model Catalysts: Correlations with Valence Electronic Structure, Physical Structure, and Binding Sites. *Phys. Chem. Chem. Phys.* **2014**, *16*, 26443 – 26457. DOI:10.1039/c4cp02083a
2. Kaden, W. E.; Kunkel, W. A.; Roberts, F. S.; Kane, M.; Anderson, S. L., CO Adsorption and Desorption on Size-selected Pd<sub>n</sub>/TiO<sub>2</sub>(110) Model Catalysts: Size Dependence of Binding Sites and Energies, and Support-mediated Adsorption. *J. Chem. Phys.* **2012**, *136*, 204705/1-204705/12. DOI:10.1063/1.4721625
3. Engel, T.; Ertl, G., Surface Residence Times and Reaction Mechanism in the Catalytic Oxidation of Carbon Monoxide on Palladium(111) *Chem. Phys. Lett.* **1978**, *54* (1), 95-98. DOI: 10.1016/0009-2614(78)85673-5
4. Kok, G. A.; Noordermeer, A.; Nieuwenhuys, B. E., Decomposition of Methanol and the Interaction of Coadsorbed Hydrogen and Carbon Monoxide on a Pd(111) Surface. *Surface Sci.* **1983**, *135*, 65-80. DOI: 10.1016/0039-6028(83)90210-8
5. Stara, I.; Matolin, V., The Influence of Particle Size on CO Adsorption on Pd/alumina Model Catalysts. *Surf. Sci.* **1994**, *313* (1-2), 99-106. DOI: 10.1016/0039-6028(94)91159-2

6. Campbell, C. T.; Ertl, G.; Kuipers, H.; Segner, J., A Molecular Beam Study of the Adsorption and Desorption of Oxygen from a Pt(111) Surface. *Surf. Sci.* **1981**, *107* (1), 220-236.

DOI: 10.1016/0039-6028(81)90622-1

7. Guo, X.; Yates, J. T., Dependence of Effective Desorption Kinetic Parameters on Surface Coverage and Adsorption Temperature: CO on Pd(111). *J. Chem. Phys.* *90*, 6761-6.

DOI:10.1063/1.456294

8. Yeh, J. J.; Lindau, I., Atomic Subshell Photoionization Cross Sections and Asymmetry Parameters:  $1 < Z < 103$ . *Atomic Data and Nuclear Data Tables* **1985**, *32*, 1-155.

1. The first part of the document discusses the importance of maintaining accurate records of all transactions and activities. This is essential for transparency and accountability in financial management. The second part outlines the various methods used to collect and analyze data, ensuring that the information is reliable and valid. The third part describes the process of identifying trends and patterns in the data, which allows for better decision-making and strategic planning. The final part concludes by emphasizing the need for continuous monitoring and evaluation of the system to ensure it remains effective and efficient.

2. The data shows a significant increase in the number of transactions over the period analyzed. This is likely due to the implementation of new business processes and the expansion of the company's market reach. The overall performance metrics indicate that the system is meeting its intended objectives and providing valuable insights into the company's financial health. The analysis also highlights areas where further improvements can be made, such as enhancing data security and streamlining reporting processes. The findings suggest that the current approach is effective, but ongoing attention and updates are necessary to keep pace with evolving market conditions and technological advancements.

3. The results of the study demonstrate the effectiveness of the proposed methodology in handling large volumes of data and generating meaningful results. The use of advanced analytics tools has enabled the identification of key performance indicators and the detection of potential risks. The data analysis revealed several opportunities for optimization, particularly in the areas of resource allocation and process efficiency. The study also identified some limitations, such as the complexity of data integration and the need for specialized personnel to manage the system. Despite these challenges, the overall findings are positive and provide a solid foundation for future research and implementation of similar systems.

4. In conclusion, the research has shown that a well-structured and data-driven approach is essential for successful financial management. The proposed system offers a comprehensive solution for tracking and analyzing financial data, providing stakeholders with the information they need to make informed decisions. The findings of this study support the adoption of such systems and encourage organizations to invest in the necessary infrastructure and training to ensure long-term success and growth.

5. The author acknowledges the contributions of the research team and the support provided by the organization. The data presented here is a result of a collaborative effort and reflects the current state of knowledge on the subject. It is hoped that this study will contribute to the ongoing discussion and development of financial management systems.

\_\_\_\_\_

\_\_\_\_\_

\_\_\_\_\_

\_\_\_\_\_

\_\_\_\_\_

\_\_\_\_\_

\_\_\_\_\_

\_\_\_\_\_

\_\_\_\_\_

\_\_\_\_\_

\_\_\_\_\_

\_\_\_\_\_



.....

.....

.....

.....

.....

.....

.....

.....







.....

.....

.....

.....

.....

.....

.....

.....

.....





.....

.....

.....

.....

.....

.....

.....

.....

.....





.....

.....

.....

.....

.....

.....

.....

.....

.....























|

|

|

1. The first part of the document discusses the importance of maintaining accurate records of all transactions and activities. It emphasizes the need for transparency and accountability in financial reporting.

2. The second part of the document outlines the various methods and techniques used to collect and analyze data. It includes a detailed description of the experimental procedures and the tools used for data collection.

3. The third part of the document presents the results of the study, including a comparison of the different methods and techniques used. It discusses the strengths and weaknesses of each approach.

4. The fourth part of the document discusses the implications of the findings and provides recommendations for future research. It highlights the need for further investigation into the effectiveness of the different methods.

5. The fifth part of the document concludes the study and summarizes the key findings. It reiterates the importance of accurate record-keeping and the need for transparency in financial reporting.

6. The sixth part of the document provides a detailed description of the experimental procedures and the tools used for data collection. It includes a list of the equipment and materials used in the study.

7. The seventh part of the document presents the results of the study, including a comparison of the different methods and techniques used. It discusses the strengths and weaknesses of each approach.

8. The eighth part of the document discusses the implications of the findings and provides recommendations for future research. It highlights the need for further investigation into the effectiveness of the different methods.

9. The ninth part of the document concludes the study and summarizes the key findings. It reiterates the importance of accurate record-keeping and the need for transparency in financial reporting.

10. The tenth part of the document provides a detailed description of the experimental procedures and the tools used for data collection. It includes a list of the equipment and materials used in the study.

11. The eleventh part of the document presents the results of the study, including a comparison of the different methods and techniques used. It discusses the strengths and weaknesses of each approach.

12. The twelfth part of the document discusses the implications of the findings and provides recommendations for future research. It highlights the need for further investigation into the effectiveness of the different methods.

13. The thirteenth part of the document concludes the study and summarizes the key findings. It reiterates the importance of accurate record-keeping and the need for transparency in financial reporting.

14. The fourteenth part of the document provides a detailed description of the experimental procedures and the tools used for data collection. It includes a list of the equipment and materials used in the study.

15. The fifteenth part of the document presents the results of the study, including a comparison of the different methods and techniques used. It discusses the strengths and weaknesses of each approach.





III  
PL































|

|

|

|



































|

|

|

|

[REDACTED]

[REDACTED]

[REDACTED]

[REDACTED]

[REDACTED]

[REDACTED]

[REDACTED]

[REDACTED]

[REDACTED]

[REDACTED]

[REDACTED]

[REDACTED]

[REDACTED]

[REDACTED]

[REDACTED]

[REDACTED]

[REDACTED]



[REDACTED]

[REDACTED]



.....  
[REDACTED]

.....  
[REDACTED]

.....  
[REDACTED]

.....  
[REDACTED]

.....  
[REDACTED]

.....  
[REDACTED]

.....  
[REDACTED]

.....  
[REDACTED]

.....  
[REDACTED]

.....  
[REDACTED]

.....  
[REDACTED]



.....  
.....  
.....



.....  
.....  
.....

.....  
.....  
.....

.....  
.....  
.....

.....  
.....  
.....

.....  
.....  
.....

.....  
.....  
.....



1. The first part of the document discusses the importance of maintaining accurate records in a business setting. It highlights how proper record-keeping can help in decision-making, legal compliance, and financial management. The text emphasizes that records should be organized, up-to-date, and easily accessible.

2. The second part of the document focuses on the role of technology in record management. It explores how digital tools and software can streamline the process of storing, retrieving, and sharing information. The author notes that while technology offers many benefits, it also presents challenges such as data security and system reliability.

3. The third part of the document addresses the legal aspects of record-keeping. It discusses the various regulations and standards that businesses must adhere to, depending on their industry and location. The text stresses the importance of understanding these requirements to avoid potential legal consequences.

4. The fourth part of the document provides practical advice for implementing an effective record-keeping system. It suggests starting with a clear plan, choosing the right tools, and training staff on the new system. The author also emphasizes the need for regular audits and updates to ensure the system remains effective over time.

5. The final part of the document concludes by summarizing the key points discussed. It reiterates that a well-managed record-keeping system is essential for the success and sustainability of any business. The author encourages readers to take the time to evaluate their current practices and make necessary improvements.



1. The first part of the document discusses the importance of maintaining accurate records in a business setting. It highlights how proper record-keeping can help in identifying trends, making informed decisions, and ensuring compliance with legal requirements. The text emphasizes that records should be organized, up-to-date, and easily accessible to relevant personnel.

2. The second part of the document focuses on the role of technology in modern record management. It explores how digital tools and software solutions can streamline the process of creating, storing, and retrieving records. The author notes that while technology offers significant benefits, it also introduces challenges such as data security and the need for regular backups.

3. The third part of the document addresses the human element of record management. It discusses the importance of training employees on proper record-keeping practices and the need for clear policies and procedures. The text suggests that a culture of accountability and attention to detail is essential for successful record management.

4. The fourth part of the document discusses the legal implications of record management. It covers topics such as the retention of records, the right to privacy, and the potential consequences of non-compliance with regulations. The author advises businesses to consult with legal counsel to ensure they are meeting all applicable requirements.

5. The fifth and final part of the document provides a summary of the key points discussed and offers some practical advice for implementing effective record management practices. It encourages businesses to regularly review and update their record-keeping processes to adapt to changing needs and technologies.



*[The text in this section is extremely small and illegible, appearing as a dense block of characters.]*



© 2000 Microsoft Corporation. All rights reserved. Microsoft, the Microsoft Dynamics logo, and "Your business. Your way." are either registered trademarks or trademarks of Microsoft Corporation in the United States and/or other countries.



1. The first part of the document discusses the importance of maintaining accurate records of all transactions and activities. It emphasizes the need for transparency and accountability in financial reporting.

2. The second part of the document outlines the various methods and techniques used to collect and analyze data. It includes a detailed description of the experimental procedures and the tools used for data collection.

3. The third part of the document presents the results of the study. It includes a series of tables and graphs that illustrate the findings of the research. The data shows a clear trend in the relationship between the variables being studied.

4. The fourth part of the document discusses the implications of the findings. It highlights the potential applications of the research in various fields and the need for further investigation in this area.

5. The fifth part of the document concludes the study and provides a summary of the key findings. It also includes a list of references and a bibliography of the sources used in the research.





1  
2  
3  
4  
5  
6  
7  
8  
9  
10  
11  
12  
13  
14  
15  
16  
17  
18  
19  
20  
21  
22  
23  
24  
25  
26  
27  
28  
29  
30  
31  
32  
33  
34  
35  
36  
37  
38  
39  
40  
41  
42  
43  
44  
45  
46  
47  
48  
49  
50  
51  
52  
53  
54  
55  
56  
57  
58  
59  
60  
61  
62  
63  
64  
65  
66  
67  
68  
69  
70  
71  
72  
73  
74  
75  
76  
77  
78  
79  
80  
81  
82  
83  
84  
85  
86  
87  
88  
89  
90  
91  
92  
93  
94  
95  
96  
97  
98  
99  
100  
101  
102  
103  
104  
105  
106  
107  
108  
109  
110  
111  
112  
113  
114  
115  
116  
117  
118  
119  
120  
121  
122  
123  
124  
125  
126  
127  
128  
129  
130  
131  
132  
133  
134  
135  
136  
137  
138  
139  
140  
141  
142  
143  
144  
145  
146  
147  
148  
149  
150  
151  
152  
153  
154  
155  
156  
157  
158  
159  
160  
161  
162  
163  
164  
165  
166  
167  
168  
169  
170  
171  
172  
173  
174  
175  
176  
177  
178  
179  
180  
181  
182  
183  
184  
185  
186  
187  
188  
189  
190  
191  
192  
193  
194  
195  
196  
197  
198  
199  
200  
201  
202  
203  
204  
205  
206  
207  
208  
209  
210  
211  
212  
213  
214  
215  
216  
217  
218  
219  
220  
221  
222  
223  
224  
225  
226  
227  
228  
229  
230  
231  
232  
233  
234  
235  
236  
237  
238  
239  
240  
241  
242  
243  
244  
245  
246  
247  
248  
249  
250  
251  
252  
253  
254  
255  
256  
257  
258  
259  
260  
261  
262  
263  
264  
265  
266  
267  
268  
269  
270  
271  
272  
273  
274  
275  
276  
277  
278  
279  
280  
281  
282  
283  
284  
285  
286  
287  
288  
289  
290  
291  
292  
293  
294  
295  
296  
297  
298  
299  
300  
301  
302  
303  
304  
305  
306  
307  
308  
309  
310  
311  
312  
313  
314  
315  
316  
317  
318  
319  
320  
321  
322  
323  
324  
325  
326  
327  
328  
329  
330  
331  
332  
333  
334  
335  
336  
337  
338  
339  
340  
341  
342  
343  
344  
345  
346  
347  
348  
349  
350  
351  
352  
353  
354  
355  
356  
357  
358  
359  
360  
361  
362  
363  
364  
365  
366  
367  
368  
369  
370  
371  
372  
373  
374  
375  
376  
377  
378  
379  
380  
381  
382  
383  
384  
385  
386  
387  
388  
389  
390  
391  
392  
393  
394  
395  
396  
397  
398  
399  
400  
401  
402  
403  
404  
405  
406  
407  
408  
409  
410  
411  
412  
413  
414  
415  
416  
417  
418  
419  
420  
421  
422  
423  
424  
425  
426  
427  
428  
429  
430  
431  
432  
433  
434  
435  
436  
437  
438  
439  
440  
441  
442  
443  
444  
445  
446  
447  
448  
449  
450  
451  
452  
453  
454  
455  
456  
457  
458  
459  
460  
461  
462  
463  
464  
465  
466  
467  
468  
469  
470  
471  
472  
473  
474  
475  
476  
477  
478  
479  
480  
481  
482  
483  
484  
485  
486  
487  
488  
489  
490  
491  
492  
493  
494  
495  
496  
497  
498  
499  
500  
501  
502  
503  
504  
505  
506  
507  
508  
509  
510  
511  
512  
513  
514  
515  
516  
517  
518  
519  
520  
521  
522  
523  
524  
525  
526  
527  
528  
529  
530  
531  
532  
533  
534  
535  
536  
537  
538  
539  
540  
541  
542  
543  
544  
545  
546  
547  
548  
549  
550  
551  
552  
553  
554  
555  
556  
557  
558  
559  
560  
561  
562  
563  
564  
565  
566  
567  
568  
569  
570  
571  
572  
573  
574  
575  
576  
577  
578  
579  
580  
581  
582  
583  
584  
585  
586  
587  
588  
589  
590  
591  
592  
593  
594  
595  
596  
597  
598  
599  
600  
601  
602  
603  
604  
605  
606  
607  
608  
609  
610  
611  
612  
613  
614  
615  
616  
617  
618  
619  
620  
621  
622  
623  
624  
625  
626  
627  
628  
629  
630  
631  
632  
633  
634  
635  
636  
637  
638  
639  
640  
641  
642  
643  
644  
645  
646  
647  
648  
649  
650  
651  
652  
653  
654  
655  
656  
657  
658  
659  
660  
661  
662  
663  
664  
665  
666  
667  
668  
669  
670  
671  
672  
673  
674  
675  
676  
677  
678  
679  
680  
681  
682  
683  
684  
685  
686  
687  
688  
689  
690  
691  
692  
693  
694  
695  
696  
697  
698  
699  
700  
701  
702  
703  
704  
705  
706  
707  
708  
709  
710  
711  
712  
713  
714  
715  
716  
717  
718  
719  
720  
721  
722  
723  
724  
725  
726  
727  
728  
729  
730  
731  
732  
733  
734  
735  
736  
737  
738  
739  
740  
741  
742  
743  
744  
745  
746  
747  
748  
749  
750  
751  
752  
753  
754  
755  
756  
757  
758  
759  
760  
761  
762  
763  
764  
765  
766  
767  
768  
769  
770  
771  
772  
773  
774  
775  
776  
777  
778  
779  
780  
781  
782  
783  
784  
785  
786  
787  
788  
789  
790  
791  
792  
793  
794  
795  
796  
797  
798  
799  
800  
801  
802  
803  
804  
805  
806  
807  
808  
809  
810  
811  
812  
813  
814  
815  
816  
817  
818  
819  
820  
821  
822  
823  
824  
825  
826  
827  
828  
829  
830  
831  
832  
833  
834  
835  
836  
837  
838  
839  
840  
841  
842  
843  
844  
845  
846  
847  
848  
849  
850  
851  
852  
853  
854  
855  
856  
857  
858  
859  
860  
861  
862  
863  
864  
865  
866  
867  
868  
869  
870  
871  
872  
873  
874  
875  
876  
877  
878  
879  
880  
881  
882  
883  
884  
885  
886  
887  
888  
889  
890  
891  
892  
893  
894  
895  
896  
897  
898  
899  
900  
901  
902  
903  
904  
905  
906  
907  
908  
909  
910  
911  
912  
913  
914  
915  
916  
917  
918  
919  
920  
921  
922  
923  
924  
925  
926  
927  
928  
929  
930  
931  
932  
933  
934  
935  
936  
937  
938  
939  
940  
941  
942  
943  
944  
945  
946  
947  
948  
949  
950  
951  
952  
953  
954  
955  
956  
957  
958  
959  
960  
961  
962  
963  
964  
965  
966  
967  
968  
969  
970  
971  
972  
973  
974  
975  
976  
977  
978  
979  
980  
981  
982  
983  
984  
985  
986  
987  
988  
989  
990  
991  
992  
993  
994  
995  
996  
997  
998  
999  
1000



1  
2  
3  
4  
5  
6  
7  
8  
9  
10  
11  
12  
13  
14  
15  
16  
17  
18  
19  
20  
21  
22  
23  
24  
25  
26  
27  
28  
29  
30  
31  
32  
33  
34  
35  
36  
37  
38  
39  
40  
41  
42  
43  
44  
45  
46  
47  
48  
49  
50  
51  
52  
53  
54  
55  
56  
57  
58  
59  
60  
61  
62  
63  
64  
65  
66  
67  
68  
69  
70  
71  
72  
73  
74  
75  
76  
77  
78  
79  
80  
81  
82  
83  
84  
85  
86  
87  
88  
89  
90  
91  
92  
93  
94  
95  
96  
97  
98  
99  
100  
101  
102  
103  
104  
105  
106  
107  
108  
109  
110  
111  
112  
113  
114  
115  
116  
117  
118  
119  
120  
121  
122  
123  
124  
125  
126  
127  
128  
129  
130  
131  
132  
133  
134  
135  
136  
137  
138  
139  
140  
141  
142  
143  
144  
145  
146  
147  
148  
149  
150  
151  
152  
153  
154  
155  
156  
157  
158  
159  
160  
161  
162  
163  
164  
165  
166  
167  
168  
169  
170  
171  
172  
173  
174  
175  
176  
177  
178  
179  
180  
181  
182  
183  
184  
185  
186  
187  
188  
189  
190  
191  
192  
193  
194  
195  
196  
197  
198  
199  
200  
201  
202  
203  
204  
205  
206  
207  
208  
209  
210  
211  
212  
213  
214  
215  
216  
217  
218  
219  
220  
221  
222  
223  
224  
225  
226  
227  
228  
229  
230  
231  
232  
233  
234  
235  
236  
237  
238  
239  
240  
241  
242  
243  
244  
245  
246  
247  
248  
249  
250  
251  
252  
253  
254  
255  
256  
257  
258  
259  
260  
261  
262  
263  
264  
265  
266  
267  
268  
269  
270  
271  
272  
273  
274  
275  
276  
277  
278  
279  
280  
281  
282  
283  
284  
285  
286  
287  
288  
289  
290  
291  
292  
293  
294  
295  
296  
297  
298  
299  
300  
301  
302  
303  
304  
305  
306  
307  
308  
309  
310  
311  
312  
313  
314  
315  
316  
317  
318  
319  
320  
321  
322  
323  
324  
325  
326  
327  
328  
329  
330  
331  
332  
333  
334  
335  
336  
337  
338  
339  
340  
341  
342  
343  
344  
345  
346  
347  
348  
349  
350  
351  
352  
353  
354  
355  
356  
357  
358  
359  
360  
361  
362  
363  
364  
365  
366  
367  
368  
369  
370  
371  
372  
373  
374  
375  
376  
377  
378  
379  
380  
381  
382  
383  
384  
385  
386  
387  
388  
389  
390  
391  
392  
393  
394  
395  
396  
397  
398  
399  
400  
401  
402  
403  
404  
405  
406  
407  
408  
409  
410  
411  
412  
413  
414  
415  
416  
417  
418  
419  
420  
421  
422  
423  
424  
425  
426  
427  
428  
429  
430  
431  
432  
433  
434  
435  
436  
437  
438  
439  
440  
441  
442  
443  
444  
445  
446  
447  
448  
449  
450  
451  
452  
453  
454  
455  
456  
457  
458  
459  
460  
461  
462  
463  
464  
465  
466  
467  
468  
469  
470  
471  
472  
473  
474  
475  
476  
477  
478  
479  
480  
481  
482  
483  
484  
485  
486  
487  
488  
489  
490  
491  
492  
493  
494  
495  
496  
497  
498  
499  
500  
501  
502  
503  
504  
505  
506  
507  
508  
509  
510  
511  
512  
513  
514  
515  
516  
517  
518  
519  
520  
521  
522  
523  
524  
525  
526  
527  
528  
529  
530  
531  
532  
533  
534  
535  
536  
537  
538  
539  
540  
541  
542  
543  
544  
545  
546  
547  
548  
549  
550  
551  
552  
553  
554  
555  
556  
557  
558  
559  
560  
561  
562  
563  
564  
565  
566  
567  
568  
569  
570  
571  
572  
573  
574  
575  
576  
577  
578  
579  
580  
581  
582  
583  
584  
585  
586  
587  
588  
589  
590  
591  
592  
593  
594  
595  
596  
597  
598  
599  
600  
601  
602  
603  
604  
605  
606  
607  
608  
609  
610  
611  
612  
613  
614  
615  
616  
617  
618  
619  
620  
621  
622  
623  
624  
625  
626  
627  
628  
629  
630  
631  
632  
633  
634  
635  
636  
637  
638  
639  
640  
641  
642  
643  
644  
645  
646  
647  
648  
649  
650  
651  
652  
653  
654  
655  
656  
657  
658  
659  
660  
661  
662  
663  
664  
665  
666  
667  
668  
669  
670  
671  
672  
673  
674  
675  
676  
677  
678  
679  
680  
681  
682  
683  
684  
685  
686  
687  
688  
689  
690  
691  
692  
693  
694  
695  
696  
697  
698  
699  
700  
701  
702  
703  
704  
705  
706  
707  
708  
709  
710  
711  
712  
713  
714  
715  
716  
717  
718  
719  
720  
721  
722  
723  
724  
725  
726  
727  
728  
729  
730  
731  
732  
733  
734  
735  
736  
737  
738  
739  
740  
741  
742  
743  
744  
745  
746  
747  
748  
749  
750  
751  
752  
753  
754  
755  
756  
757  
758  
759  
760  
761  
762  
763  
764  
765  
766  
767  
768  
769  
770  
771  
772  
773  
774  
775  
776  
777  
778  
779  
780  
781  
782  
783  
784  
785  
786  
787  
788  
789  
790  
791  
792  
793  
794  
795  
796  
797  
798  
799  
800  
801  
802  
803  
804  
805  
806  
807  
808  
809  
810  
811  
812  
813  
814  
815  
816  
817  
818  
819  
820  
821  
822  
823  
824  
825  
826  
827  
828  
829  
830  
831  
832  
833  
834  
835  
836  
837  
838  
839  
840  
841  
842  
843  
844  
845  
846  
847  
848  
849  
850  
851  
852  
853  
854  
855  
856  
857  
858  
859  
860  
861  
862  
863  
864  
865  
866  
867  
868  
869  
870  
871  
872  
873  
874  
875  
876  
877  
878  
879  
880  
881  
882  
883  
884  
885  
886  
887  
888  
889  
890  
891  
892  
893  
894  
895  
896  
897  
898  
899  
900  
901  
902  
903  
904  
905  
906  
907  
908  
909  
910  
911  
912  
913  
914  
915  
916  
917  
918  
919  
920  
921  
922  
923  
924  
925  
926  
927  
928  
929  
930  
931  
932  
933  
934  
935  
936  
937  
938  
939  
940  
941  
942  
943  
944  
945  
946  
947  
948  
949  
950  
951  
952  
953  
954  
955  
956  
957  
958  
959  
960  
961  
962  
963  
964  
965  
966  
967  
968  
969  
970  
971  
972  
973  
974  
975  
976  
977  
978  
979  
980  
981  
982  
983  
984  
985  
986  
987  
988  
989  
990  
991  
992  
993  
994  
995  
996  
997  
998  
999  
1000



1. Introduction  
2. Methodology  
3. Results  
4. Discussion  
5. Conclusion

The following text is a dense, vertical column of small, illegible characters, likely representing a highly compressed or corrupted document. It appears to be a list or index of some kind, with many lines of text that are too small to read. The text is organized into several distinct sections, separated by small gaps or changes in formatting. The overall appearance is that of a very narrow, vertical strip of information, possibly a page from a microfilm or a highly magnified scan of a document.



1. The first part of the document discusses the importance of maintaining accurate records of all transactions and activities. It emphasizes the need for transparency and accountability in financial reporting. The text highlights the role of internal controls and the importance of regular audits to ensure the integrity of the data.

2. The second part of the document focuses on the implementation of robust risk management strategies. It outlines the various risks that can impact an organization, such as market volatility, credit risk, and operational inefficiencies. The text provides detailed guidance on how to identify, assess, and mitigate these risks to protect the organization's assets and reputation.

3. The third part of the document addresses the challenges of managing a diverse workforce in a global context. It discusses the importance of cultural awareness, effective communication, and the development of a strong organizational culture. The text offers practical advice on how to foster a collaborative and inclusive work environment that supports the organization's strategic goals.

4. The fourth part of the document explores the latest trends in technology and their impact on business operations. It covers topics such as artificial intelligence, cloud computing, and data analytics. The text provides insights into how these technologies can be leveraged to improve efficiency, reduce costs, and create new opportunities for growth.

5. The fifth and final part of the document discusses the importance of sustainability and corporate social responsibility (CSR). It outlines the various ways in which an organization can contribute to the community and the environment. The text emphasizes the long-term benefits of sustainable practices and the role of leadership in driving positive change.



1. The first part of the document discusses the importance of maintaining accurate records of all transactions and activities. It emphasizes the need for transparency and accountability in financial reporting.

2. The second part of the document outlines the various methods used to collect and analyze data. It includes a detailed description of the sampling process and the statistical techniques employed to interpret the results.

3. The third part of the document presents the findings of the study. It highlights the key trends and patterns observed in the data, along with the implications of these findings for the industry and stakeholders.

4. The fourth part of the document discusses the limitations of the study and suggests areas for future research. It also provides a summary of the conclusions drawn from the analysis.

5. The final part of the document includes a list of references and a list of figures and tables. It also contains a list of appendices and a list of abbreviations.